The Arctic

J. K Andersen, Liss M Andreassen, Emily H Baker, Thomas J Ballinger, Logan T Berner, Germar H Bernhard, Uma S Bhatt, Jarle W Bjerke, Jason E Box, L. Britt, et al.

STATE OF THE CLIMATE IN 2019

THE ARCTIC

J. Richter-Menge and M. L. Druckenmiller, Eds.

Special Online Supplement to the *Bulletin of the American Meteorological Society,* Vol.101, No. 8, August, 2020

https://doi.org/10.1175/BAMS-D-20-0086.1

Corresponding author: Matthew L. Druckenmiller / druckenmiller@nsidc.org

STATE OF THE CLIMATE IN 2019

The Arctic

Editors

Jessica Blunden
Derek S. Arndt

Chapter Editors

Peter Bissolli
Howard J. Diamond
Matthew L. Druckenmiller
Robert J. H. Dunn
Catherine Ganter
Nadine Gobron
Rick Lumpkin
Jacqueline A. Richter-Menge
Tim Li
Ademe Mekonnen
Ahira Sánchez-Lugo
Ted A. Scambos
Carl J. Schreck III
Sharon Stammerjohn
Diane M. Stanitski
Kate M. Willett

Technical Editor

Andrea Andersen

BAMS Special Editor for Climate

Richard Rosen

American Meteorological Society

Cover credit:
A patch of eightpetal mountain-avens (*Dryas octopetala*) bloom on a tundra hillslope in the Brooks Range near Atigun Pass, northern Alaska, 2 June 2019. Photo by Gerald V. Frost.

The Arctic is one chapter from the *State of the Climate in 2019* annual report and is available from https://doi.org/10.1175/BAMS-D-20-0086.1. Compiled by NOAA's National Centers for Environmental Information, *State of the Climate in 2019* is based on contributions from scientists from around the world. It provides a detailed update on global climate indicators, notable weather events, and other data collected by environmental monitoring stations and instruments located on land, water, ice, and in space. The full report is available from https://doi.org/10.1175/2020BAMSStateoftheClimate.1.

How to cite this document:

Citing the complete report:
Blunden, J. and D. S. Arndt, Eds., 2020: State of the Climate in 2019. *Bull. Amer. Meteor. Soc.,* **101** (8), Si–S429, https://doi.org/10.1175/2020BAMSStateoftheClimate.1.

Citing this chapter:
Richter-Menge, J. and M. L. Druckenmiller, Eds., 2020: The Arctic [in "State of the Climate in 2019"]. *Bull. Amer. Meteor. Soc.,* **101** (8), S239–S285, https://doi.org/10.1175/BAMS-D-20-0086.1.

Citing a section (example):
Mudryk, L., R. Brown, C. Derksen, K. Luojus, and B. Decharme, 2020: Terrestrial snow cover [in "State of the Climate in 2019"]. *Bull. Amer. Meteor. Soc.,* **101** (8), S263–S265, https://doi.org/10.1175/BAMS-D-20-0086.1.

Editor and Author Affiliations (alphabetical by name)

Andersen, J. K., Geological Survey of Denmark and Greenland, Copenhagen, Denmark
Andreassen, Liss M., Section for Glaciers, Ice and Snow, Norwegian Water Resources and Energy Directorate, Oslo, Norway
Baker, Emily H., U.S. Geological Survey, Alaska Science Center, Anchorage, Alaska
Ballinger, Thomas J., International Arctic Research Center, University of Alaska Fairbanks, Fairbanks, Alaska
Berner, Logan T., School of Informatics, Computing, and Cyber Systems, Northern Arizona University, Flagstaff, Arizona
Bernhard, Germar H., Biospherical Instruments Inc., San Diego, California
Bhatt, Uma S., Geophysical Institute, University of Alaska Fairbanks, Fairbanks, Alaska
Bjerke, Jarle W., Norwegian Institute for Nature Research, FRAM – High North Research Centre for Climate and the Environment, Tromsø, Norway
Box, Jason E., Geological Survey of Denmark and Greenland, Copenhagen, Denmark
Britt, L., NOAA/NMFS Alaska Fisheries Science Center, Seattle, Washington
Brown, R., Climate Research Division, Environment and Climate Change Canada, Montréal, Quebec, Canada
Burgess, David, Geological Survey of Canada, Ottawa, Ontario, Canada
Cappelen, John, Danish Meteorological Institute, Copenhagen, Denmark
Christiansen, Hanne H., Geology Department, University Centre in Svalbard, The University Center in Svalbard, Longyearbyen, Norway
Decharme, B., Centre National de Recherches Météorologiques, France
Derksen, C., Climate Research Division, Environment and Climate Change Canada,Downsview, Ontario, Canada
Drozdov, D. S., Earth Cryosphere Institute, and Tyumen State University, Tyumen, Russia
Druckenmiller, Matthew L., National Snow and Ice Data Center, Boulder, Colorado
Epstein, Howard E., Department of Environmental Sciences, University of Virginia, Charlottesville, Virginia
Farquharson, L. M., Geophysical Institute, University of Alaska Fairbanks, Fairbanks, Alaska
Farrell, Sinead L., NOAA Earth System Science Interdisciplinary Center, University of Maryland, College Park, Maryland
Fausto, Robert S., Geological Survey of Denmark and Greenland, Copenhagen, Denmark
Fettweis, Xavier, SPHERES research unit, University of Liège, Liège, Belgium
Fioletov, Vitali E., Environment and Climate Change Canada, Toronoto, Ontario, Canada
Forbes, Bruce C., Arctic Centre, University of Lapland, Rovaniemi, Finland
Frost, Gerald V., ABR, Inc. Environmental Research & Services, Fairbanks, Alaska
Gerland, Sebastian, Norwegian Polar Institute, Fram Centre, Tromsø, Norway
Goetz, Scott J., School of Informatics, Computing, and Cyber Systems, Northern Arizona University, Flagstaff, Arizona
Grooß, Jens-Uwe, Forschungszentrum Jülich, Jülich, Germany
Hanna, Edward, School of Geography and Lincoln Centre for Water and Planetary Health, University of Lincoln, Lincoln, United Kingdom
Hanssen-Bauer, Inger, Norwegian Meteorological Institute, Blindern, Oslo, Norway
Hendricks, Stefan, Alfred Wegener Institute, Helmholtz Centre for Polar and Marine Research, Bremerhaven, Germany
Ialongo, Iolanda, Finnish Meteorological Institute, Helsinki, Finland
Isaksen, K., Norwegian Meteorlogical Institute, Blindern, Oslo, Norway
Johnsen, Bjørn, Norwegian Radiation and Nuclear Safety, Østerås, Norway
Kaleschke, L., Alfred Wegener Institute, Helmholtz Centre for Polar and Marine Research, Bremerhaven, Germany
Kholodov, A. L., Geophysical Institute, University of Alaska Fairbanks, Fairbanks, Alaska
Kim, Seong-Joong, Korea Polar Research Institute, Incheon, Republic of Korea
Kohler, Jack, Norwegian Polar Institute, Tromsø, Norway
Labe, Zachary, University of California at Irvine, Irvine, California
Ladd, Carol, NOAA/OAR Pacific Marine Environmental Laboratory, Seattle, Washington
Lakkala, Kaisa, Finnish Meteorological Institute, Sodankylä, Finland
Lara, Mark J., Department of Plant Biology and Department of Geography, University of Illinois at Urbana-Champaign, Urbana, Illinois
Loomis, Bryant, NASA Goddard Space Flight Center, Greenbelt, Maryland
Luks, Bartłomiej, Institute of Geophysics, Polish Academy of Sciences, Warsaw, Poland
Luojus, K., Arctic Research Centre, Finnish Meteorological Institute, Helsinki, Finland
Macander, Matthew J., ABR, Inc. Environmental Research & Services, Fairbanks, Alaska
Malkova, G. V., Earth Cryosphere Institute, Tyumen Science Center, Tyumen, Russia
Mankoff, Kenneth D., Geological Survey of Denmark and Greenland, Copenhagen, Denmark
Manney, Gloria L., NorthWest Research Associates, and New Mexico Institute of Mining and Technology, Socorro, New Mexico
Marsh, J. M., College of Fisheries and Ocean Sciences, University of Alaska Fairbanks, Fairbanks, Alaska
Meier, Walt, National Snow and Ice Data Center, Cooperative Institute for Research in Environment Sciences at the University of Colorado, Boulder, Colorado
Moon, Twila A., National Snow and Ice Data Center, Cooperative Institute for Research in Environmental Sciences at the University of Colorado, Boulder, Colorado
Mote, Thomas, Department of Geography, University of Georgia, Athens, Georgia
Mudryk, L., Climate Research Division, Environment and Climate Change Canada, Downsview, Ontario, Canada
Mueter F. J., College of Fisheries and Ocean Sciences, University of Alaska Fairbanks, Alaska
Müller, Rolf, Forschungszentrum Jülich, Jülich, Germany
Nyland, K. E., Department of Geography, George Washington University, Washington, D.C.
O'Neel, Shad, U.S. Geological Survey, Alaska Science Center, Anchorage, Alaska
Overland, James E., NOAA/OAR Pacific Marine Environmental Laboratory, Seattle, Washington
Perovich, Don, Thayer School of Engineering, Dartmouth College, Hanover, New Hampshire
Phoenix, Gareth K., Department of Animal and Plant Sciences, University of Sheffield, Sheffield, United Kingdom
Raynolds, Martha K., Institute of Arctic Biology, University of Alaska Fairbanks, Alaska
Reijmer, C. H., Institute for Marine and Atmospheric Research Utrecht, Utrecht University, Utrecht, The Netherlands
Richter-Menge, Jacqueline, University of Alaska Fairbanks, Institute of Northern Engineering, Fairbanks, Alaska
Ricker, Robert, Alfred Wegener Institute, Helmholtz Centre for Polar and Marine Research, Bremerhaven, Germany
Romanovsky, Vladimir E., Geophysical Institute, University of Alaska Fairbanks, Fairbanks, Alaska; Earth Cryosphere Institute, Tyumen Science Center, Tyumen, Russia
Schuur, E. A. G., Center for Ecosystem Science and Society, Northern Arizona University, Flagstaff, Arizona

Sharp, Martin, Department of Earth and Atmospheric Sciences, University of Alberta, Edmonton, Alberta, Canada
Shiklomanov, Nikolai I., Department of Geography, George Washington University, Washington, D.C.
Smeets, C. J. P. P., Institute for Marine and Atmospheric Research Utrecht, Utrecht University, Utrecht, The Netherlands
Smith, Sharon L., Geological Survey of Canada, Natural Resources Canada, Ottawa, Ontario, Canada
Streletskiy, Dimitri A., Department of Geography, George Washington University, Washington, D.C.
Tedesco, Marco, Lamont Doherty Earth Observatory, Columbia University, Palisades, New York, and NASA Goddard Institute of Space Studies, New York, New York
Thoman, Richard L., International Arctic Research Center, University of Alaska Fairbanks, Fairbanks, Alaska
Thorson, J. T., NOAA/NMFS Alaska Fisheries Science Center, Seattle, Washington
Tian-Kunze, X., Alfred Wegener Institute, Helmholtz Centre for Polar and Marine Research, Bremerhaven, Germany
Timmermans, Mary-Louise, Yale University, New Haven, Connecticut
Tømmervik, Hans, Norwegian Institute for Nature Research, Tromsø, Norway
Tschudi, Mark, Aerospace Engineering Sciences, University of Colorado, Boulder, Colorado
van As, Dirk, Geological Survey of Denmark and Greenland, Copenhagen, Denmark
van de Wal, R. S. W., Institute for Marine and Atmospheric Research Utrecht, Utrecht University, Utrecht, The Netherlands
Walker, Donald A., Institute of Arctic Biology, University of Alaska Fairbanks, Alaska
Walsh, John E., International Arctic Research Center, University of Alaska Fairbanks, Fairbanks, Alaska
Wang, Muyin, NOAA/OAR Pacific Marine Environmental Laboratory, and Joint Institute for the Study of the Atmosphere and Ocean, University of Washington, Seattle, Washington
Webster, Melinda, Geophysical Institute, University of Alaska Fairbanks, Fairbanks, Alaska
Winton, Øyvind, Geological Survey of Denmark and Greenland, Copenhagen, Denmark
Wolken, Gabriel J., Alaska Division of Geological & Geophysical Surveys; University of Alaska Fairbanks, Fairbanks, Alaska
Wood, K., Joint Institute for the Study of the Atmosphere and Ocean, University of Washington, and NOAA/OAR Pacific Marine Environmental Laboratory, Seattle, Washington
Wouters, Bert, Institute for Marine and Atmospheric Research, Utrecht University, Utrecht, Netherlands; Department of Geoscience & Remote Sensing, Delft University of Technology, Delft, The Netherlands
Zador, S., NOAA/NMFS Alaska Fisheries Science Center, Seattle, Washington

Editorial and Production Team

Andersen, Andrea, Technical Editor, Innovative Consulting Management Services, LLC, NOAA/NESDIS National Centers for Environmental Information, Asheville, North Carolina
Griffin, Jessicca, Graphics Support, Cooperative Institute for Satellite Earth System Studies, North Carolina State University, Asheville, North Carolina
Hammer, Gregory, Content Team Lead, Communications and Outreach, NOAA/NESDIS National Centers for Environmental Information, Asheville, North Carolina
Love-Brotak, S. Elizabeth, Lead Graphics Production, NOAA/NESDIS National Centers for Environmental Information, Asheville, North Carolina
Misch, Deborah J., Graphics Support, Innovative Consulting Management Services, LLC, NOAA/NESDIS National Centers for Environmental Information, Asheville, North Carolina
Riddle, Deborah B., Graphics Support, NOAA/NESDIS National Centers for Environmental Information, Asheville, North Carolina
Veasey, Sara W., Visual Communications Team Lead, Communications and Outreach, NOAA/NESDIS National Centers for Environmental Information, Asheville, North Carolina

5. Table of Contents

***Please refer to Chapter 8 (Relevant datasets and sources) for a list of all climate variables and datasets used in this chapter for analyses, along with their websites for more information and access to the data.**

5. THE ARCTIC

J. Richter-Menge and M. L. Druckenmiller, Eds.

a. Overview—M. L. Druckenmiller and J. Richter-Menge

Mean annual Arctic surface air temperatures (SAT) over land have increased more than twice as fast as the global mean since the mid-1980s. Observations from 2019 continue to highlight prolonged changes across key and connected features of the Arctic's land, ice, ocean, and atmosphere. Through these connections, the changing Arctic environment has a magnified impact on ecosystems and societies on regional and global scales.

Central to observed changes throughout the Arctic system is the persistent and pronounced increase in Arctic SAT, which in 2019 was the second highest in the 120-year observational record. In particular, the southward displacement of the polar vortex over North America—a repeat of conditions from 2018—brought record-high SATs to Alaska and northwest Canada. These conditions contributed to the second winter in a row when sea ice coverage in the Bering Sea was by far the lowest in observed or reconstructed records dating back to 1850 (Richter-Menge et al. 2019; Walsh et al. 2019). More generally, warming air temperatures are linked to the continued Arctic-wide decline in the extent and thickness of the sea ice cover. In March 2019, when the ice reached its maximum extent for the year, thin, first-year ice predominated at ~77%, compared to about 55% in the 1980s. This transformation toward thinner and more mobile ice makes the sea ice cover more vulnerable to melting out in summer and, therefore, diminishes the ice cover's role in cooling the Arctic region by reflecting incoming solar radiation back to space. In September 2019, the minimum sea ice extent at the end of summer was tied with 2007 and 2016 for the second smallest in the 41-year satellite record.

The declining trend in the extent of the sea ice cover is driving changes in sea surface temperatures (SSTs) in the Arctic Ocean and adjacent seas, largely caused by direct solar heating of exposed, ice-free—and thus darker (i.e., lower albedo)—Arctic waters. A warmer ocean, in turn, melts more sea ice. This feedback, known as the ice–albedo feedback, contributes to the continued and accelerated warming of the Arctic region. August mean SSTs show significant warming for 1982–2019 in most regions of the Arctic Ocean that are ice-free in August. On a regional scale, the Chukchi and Bering Seas continue to exhibit larger warming trends in August than the Arctic-wide August mean, with the Chukchi Sea mean SSTs in August 2019 being the second highest on record.

Increased ocean temperatures and reduced sea ice in the Bering Sea are leading to shifts in fish distributions within some of the most valuable fisheries in the world. On the Bering Sea shelf, the summer distribution of fishes living on the seafloor is closely tied to the extent of the cold pool (bottom water temperatures < 2°C), which forms during autumn freeze-up when cold dense water sinks to the seafloor where it persists throughout the following summer. As this cold pool was considerably reduced during summers 2018 and 2019 in association with the record low winter sea ice coverage, southern fish species expanded northward. As a result, larger and more abundant boreal (southern Bering Sea) species, as opposed to smaller and less abundant Arctic species, dominated a large portion of the shelf in 2018 and 2019. These shifts in populations present challenges for the management of commercial and subsistence fisheries alike, while illuminating the potential for further cascading changes to the ecosystem.

On land, the increasing SATs are causing a decrease in the extent of the Arctic spring snow cover, an increase in the overall amount of Arctic vegetation, and the warming and thawing of perennially-frozen ground, known as permafrost. These components of the Arctic environment interconnect to influence hydrology, surface stability, wildlife, infrastructure, and the livelihoods

of Indigenous Peoples. Permafrost thaw also promotes the release of carbon dioxide and methane from soils to the atmosphere through the microbial conversion of permafrost carbon that has accumulated over hundreds to thousands of years. New evidence suggests that the increasing release of these sequestered greenhouse gases may be shifting permafrost soils from being a net carbon sink to being a net carbon source, thereby further accelerating global climate warming.

Land-based ice across the Arctic is similarly responding to the persistent rise of SATs. Melt across the Greenland ice sheet (GrIS) is contributing to global average sea level rise at a current rate of about 0.7 mm yr^{-1}. During the 2019 melt season, the extent and magnitude of ice loss over the GrIS rivaled 2012, the previous year of record ice loss. Observations from 2018 and 2019 reveal a continuing trend of significant ice loss from glaciers and ice caps across the Arctic, especially in Alaska and Arctic Canada. The Arctic-wide mass loss from glaciers and ice caps outside of Greenland is estimated to contribute approximately 0.4 mm yr^{-1} to global sea level rise, which, if normalized by area, represents more melt water per area than the GrIS.

Long-term observing in the Arctic has revealed a region undergoing sustained and often rapid change. Yet, throughout this chapter, observations are also often marked by regional differences (e.g., continental-scale differences in snow cover and terrestrial greening), indicating a complex and variable system, tied in part to its global connections via the ocean and atmosphere. The Arctic plays a critical role in regulating global climate, primarily through the reflective properties of sea ice, land ice, and snow. As these features diminish in extent, the Arctic will increasingly exert its influence on the rest of Earth in other ways, too. Through global sea level rise, the release of permafrost carbon, and its role in steering global weather patterns, the Arctic is vitally connected to people worldwide.

(This chapter includes a focus on glaciers and ice caps outside Greenland, section f, which alternates yearly with a section on Arctic river discharge, as the scales of regular observation for both of these climate components are best suited for reporting every two years.)

b. Surface air temperature—J. E. Overland, T. J. Ballinger, E. Hanna, I. Hanssen-Bauer, S.-J. Kim, J. E. Walsh, M. Wang, U. S. Bhatt, and R. L. Thoman

Arctic surface air temperature (SAT) is a leading indicator of global climate change. Although there are year-to-year and regional differences in SATs that are driven by natural variability, the magnitude, persistence, and Arctic-wide patterns of recent temperature increases are indicators of global climate warming due to increasing concentrations of atmospheric greenhouse gases (Overland 2009; Notz and Stroeve 2016). Increasing atmospheric temperatures also act as a driver of Arctic changes in the ocean and on land. For instance, a linear relationship between global temperature change and Arctic sea ice cover decline (section 5d) suggests a direct climate forcing (Mahlstein and Knutti 2012). Similarly, tundra greening (section 5i), especially along coastlines, and glacier mass loss (sections 5e,f) are also results of air temperature increases (Box et al. 2019).

Highlights from 2019 include a mean annual SAT over Arctic land that was the second highest in the observational record (1900–present). On the regional scale, Alaska experienced higher-than-normal air temperatures throughout the year, especially in winter, that were associated with unusual southerly winds and a lack of sea ice in the Bering Sea (section 5d). West Greenland experienced especially warm localized air temperatures during spring and summer, which supported extensive ice sheet melt events (section 5e) and early regional snow melt. In autumn, a major northward jet stream displacement resulted in extreme high temperatures in northern Greenland.

1) Mean annual land surface air temperature

At +1.7°C, the mean annual SAT anomaly for January–December 2019 for land weather stations north of 60°N, relative to the 1981–2010 mean, is the second-highest value after 2016 in the observational record starting in 1900. Since the mid-1980s, Arctic warming has consistently outpaced global mean temperature increases, leading to an Arctic that has now warmed more than twice as much as the

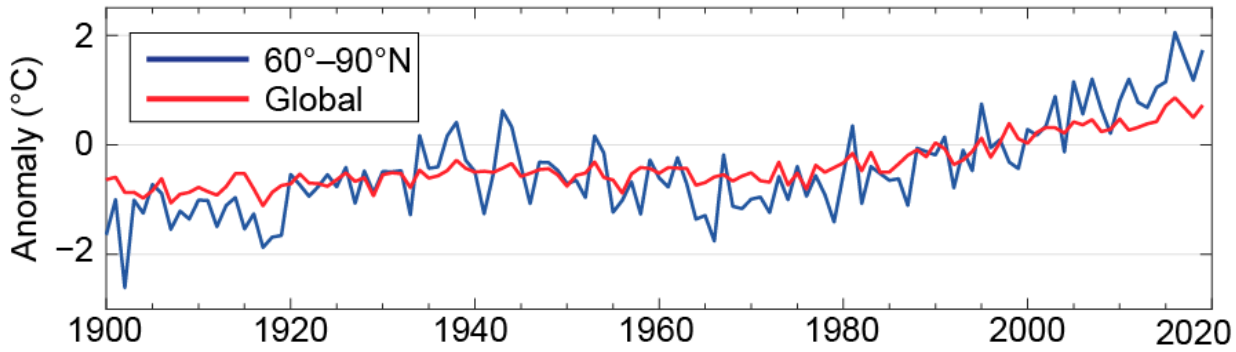

Fig. 5.1. Arctic (land stations north of 60°N; blue line) and global (red line) mean annual land SAT anomalies (in °C) for the period 1900–2019 relative to the 1981–2010 mean value. Note that there were few stations in the Arctic, particularly in northern Canada, before 1940. (Source: CRUTEM4 dataset.)

globe—a phenomenon known as Arctic amplification (Fig. 5.1). While there is currently no consensus on the relative importance of several factors contributing to Arctic amplification, mechanisms include: reduced summer albedo due to sea ice and snow cover loss (Pithan and Mauritsen 2014); the increase of water vapor and clouds in the Arctic atmosphere (Dufour et al. 2016; Kim et al. 2017); lapse-rate feedback (decreases in tropospheric temperature with height [Stuecker et al. 2018]); ocean heat transport (Langenbrunner 2020); and decreased air pollution (Acosta Navarro et al. 2016).

2) Air temperature variation

Seasonal air temperature variations during 2019 are divided into winter (January, February, March [JFM]); spring (April, May, June [AMJ]); summer (July, August, September [JAS]); and autumn (October, November, December [OND]) (Fig. 5.2). These SAT divisions are chosen to coincide with the seasonal cycles of key Arctic variables. For instance, the summer sea ice minimum extent occurs in September and autumn cooling continues through December.

Winter 2019 (JFM). A major Arctic warming event in winter (Fig. 5.2a) was observed in Alaska and its adjacent seas, where monthly temperature anomalies reached more than 6°C above normal. Over the Bering Sea, this event was similar, yet even warmer than the event observed in winter 2018, and contributed to low sea ice extent and ecological impacts to fisheries (Sidebar 5.1) and marine mammals (Richter-Menge et al. 2019). In both cases, this pattern of SAT was supported by the displacement of the stratospheric polar vortex to over North America (Fig. 5.3b). March was exceptionally warm over much of Alaska, the Yukon, and western Northwest Territories, where most places set all-time record high monthly means, in some cases 3°C higher than any previous March.

In February and March 2019 (Fig 5.3a), as in winter 2018, strong, warm winds from the south over the Bering Sea greatly delayed sea ice advances (section 5d) and moved warm air

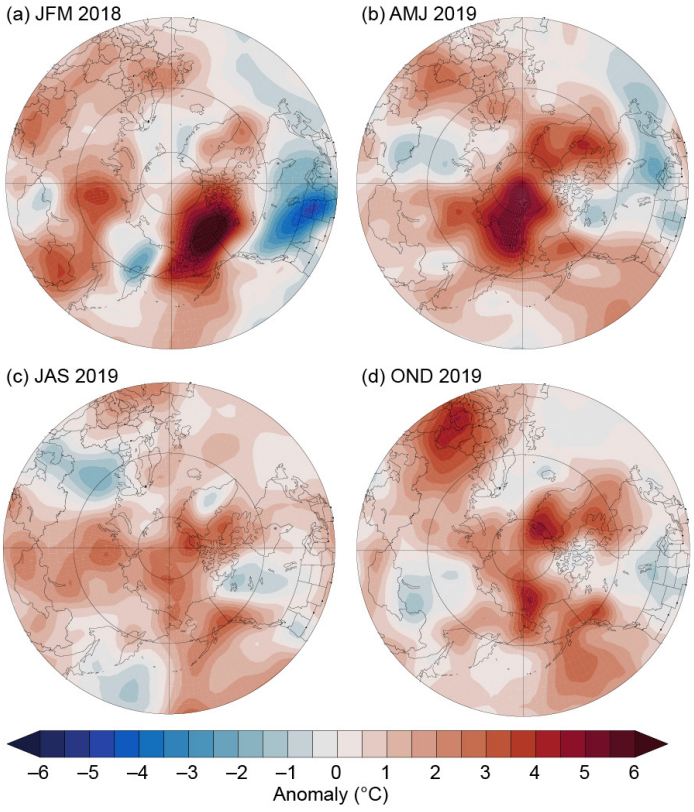

Fig. 5.2. Seasonal anomaly patterns during 2019 for near-SAT (in °C) relative to the baseline period 1981–2010 in (a) winter, (b) spring, (c) summer, and (d) autumn. Temperature anomalies are from slightly above the surface layer (at 925 hPa level) to emphasize large spatial patterns rather than local features. (Source: NCAR/NCEP reanalysis via NOAA/ESRL.)

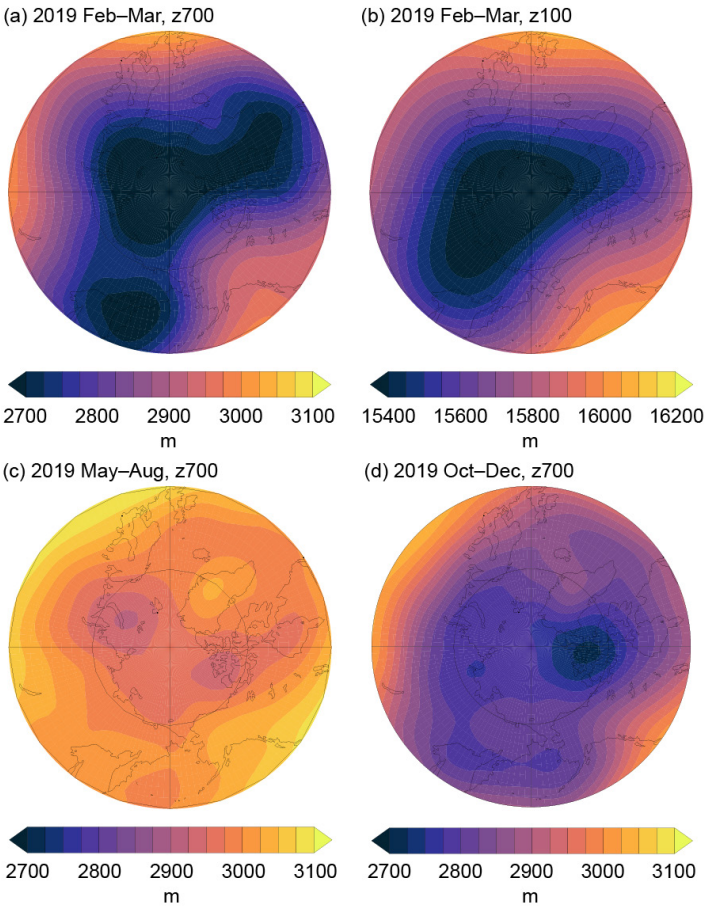

Fig. 5.3. The geopotential height pattern (m) (a), (c), (d) at 700 hPa and (b) 100 hPa for selected 2019 time periods that also reflect Arctic-wide wind patterns. The 700-hPa geopotential height field is used to characterize atmospheric wind circulation about a third of the way up in the troposphere; winds tend to follow the contours of geopotential heights anticlockwise around low values. (a) Feb–Mar 2019 and (b) the polar vortex at 100 hPa in Feb–Mar 2019, which supported the winter wind pattern shown in Fig. 5.3a. (c) May–Aug geopotential height at 700 hPa. There is a low geopotential height center and cyclonic flow near the Kara Sea and Canadian Arctic Archipelago and high geopotential heights and anticyclonic winds over Greenland, which acted in tandem to transport warm air from lower latitudes into the central Arctic. The persistent ridges over the Pacific Arctic and Greenland caused southerly winds and warm air temperatures over Alaska and the southern Yukon Territory and over areas to the north and west of Greenland, respectively. (d) Rare displacement of the jet stream over the Canadian Arctic Archipelago and Baffin Bay in Oct–Dec 2019 led to extremely high northern Greenland temperatures. (Source: NCAR/NCEP reanalysis via NOAA/ESRL.)

northward along the date line into the central Arctic. The lower-level atmospheric wind pattern (Fig. 5.3a) was connected to patterns higher in the atmosphere (i.e., the polar vortex; Fig. 5.3b) that contributed to the persistence of the wind pattern over Alaska and the rest of North America.

Spring 2019 (AMJ). Spring (Fig. 5.2b) showed warm temperature anomalies, especially in the East Siberian Sea extending into the central Arctic where temperatures were 5°C above average and were associated with offshore winds, as also seen during 2017 and 2018. In April, record high temperatures occurred at several sites in Scandinavia and in many parts of Iceland. Localized extreme temperatures off the west coast of Greenland triggered an early and extensive snow melt season (sections 5e,g). Stations along the Greenland coast, especially the west and northwest coasts, had near-record high temperature maxima of ~22°C in June due to localized southerly winds (Fig. 5.3c). Similar high temperatures continued into the summer.

Summer 2019 (JAS). Unlike summers 2016, 2017, and 2018, summer 2019 returned to the relatively warm conditions observed in much of the previous decade (Fig. 5.2c). Low surface pressures, particularly over the Canadian Archipelago and Kara Sea, combined with high pressure over Greenland to advect warm, southerly air into the central Arctic, causing early summer melting (section 5d). June and especially July were very warm over much of Alaska and the southern Yukon (+4°C anomalies). At Anchorage, all three months were the warmest on record over the last 69 years, caused by a persistent ridge of high pressure and southerly winds over the Pacific Arctic (Fig. 5.3c). Similarly, July was the warmest month on record in Reykjavik, Iceland, since records began there in 1871 (Trausti Jónsson, Icelandic Met. Office, personal communication).

Autumn 2019 (OND). Positive temperature anomalies stretched across the central Arctic with the largest temperature anomalies (+3°C) in the Chukchi Sea and north Greenland (Fig. 5.2d). Like autumn 2017 and 2018, the sustained warming pattern in the Chukchi Sea during 2019 was associated with a delayed autumn sea ice freeze-up (section 5d). During autumn 2019, the Northern Hemisphere jet stream pattern was relatively zonal and well to the south of Arctic regions, with strong westerly winds over North America and Europe and little penetration of Arctic air toward

the south. The exception was the location of low 700-hPa geopotential heights displaced from the North Pole to northern Canada, centered in the Canadian Arctic Archipelago, which created the strongest high-pressure Greenland blocking episode (above-average mid-tropospheric geopotential heights and anticyclonic winds over Greenland) in October since 2006 (Fig. 5.3d). This blocking pattern led to southerly winds advecting relatively warm air to northern Greenland, resulting in the observed large temperature anomalies.

c. Sea surface temperature—M.-L. Timmermans, Z. Labe, and C. Ladd

Summer sea surface temperatures (SSTs) in the Arctic Ocean are driven mainly by the amount of incoming solar radiation absorbed by the sea surface. Solar warming of the Arctic surface ocean is influenced by the distribution of sea ice (with greater warming occurring in ice-free regions), cloud cover, ocean optical properties, and upper-ocean stratification. In the Barents and Chukchi Seas, there is an additional source of ocean heat contributed by the advection of warm water from the North Atlantic and North Pacific Oceans, respectively. Arctic SSTs are an essential indicator of the role of the ice–albedo feedback mechanism in any given summer melt season. As the area of sea ice cover decreases (section 5d), more incoming solar radiation is absorbed by the ocean and, in turn, the warmer ocean melts more sea ice. In addition, higher SSTs are associated with delayed autumn freeze-up and increased ocean heat storage throughout the year. Marine ecosystems are influenced by SST, which affects the timing and development of primary and secondary production cycles, as well as available habitat for upper-trophic and temperature-sensitive species.

Sea surface temperature data presented in this section are a blend of in situ and satellite measurements from December 1981 to present, taken from the OISSTv2 (Reynolds et al. 2002, 2007). Compared to purely in situ temperature measurements, the OISSTv2 product explains about 80% of the variance, with an overall cold bias via its tendency to underestimate SST by −0.02°C (Stroh et al. 2015). The OISSTv2 product uses a linear relationship with sea ice concentration to infer SST, with SST constrained to −1.8°C (the freezing point of seawater with a salinity of 33 g kg^{-1} at the sea surface) where ice concentration is 100% (Reynolds et al. 2007). Variations in freezing temperature as a result of variations in sea surface salinity (not accounted for in the algorithm) imply that OISSTv2 SSTs under sea ice can be too cool by up to 0.2°C, with the highest errors in the fresher surface waters of the Canada Basin (see Timmermans and Proshutinsky 2015). August mean SSTs provide the most appropriate representation of Arctic Ocean summer SSTs, because they are not affected by the cooling and subsequent sea ice growth that typically takes place in the latter half of September. The period 1982–2010 is used as a climatological reference mean.

August 2019 mean SSTs ranged from 8° to 9°C in the southern Chukchi and Barents Seas to approximately 1°C in the interior Arctic Ocean near the mean sea ice edge for that month (Fig. 5.4a). Sea surface temperatures in August 2019 were consistent with sustained mean August SST

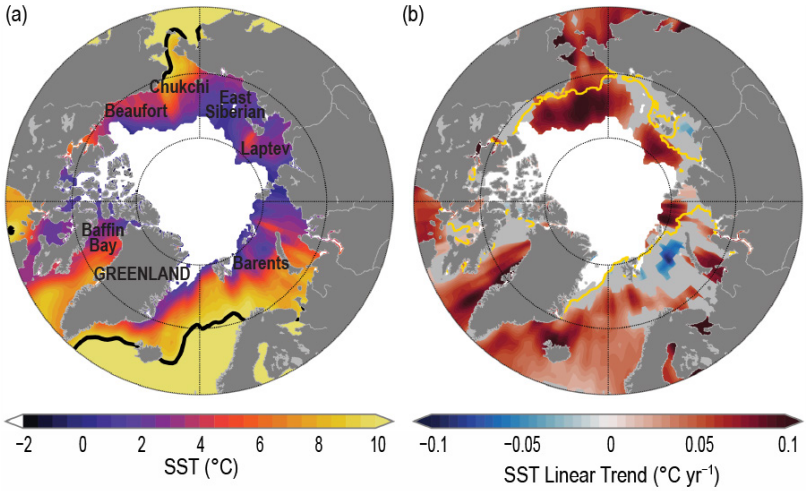

Fig. 5.4. (a) Mean SST (°C) in Aug 2019. White shading is the Aug 2019 mean sea ice extent, and black contours indicate the 10°C SST isotherm. (b) Linear SST trend (°C yr^{-1}) for Aug of each year from 1982–2019. The trend is shown only for values that are statistically significant at the 95% confidence interval; the region is gray otherwise. The yellow line indicates the median ice edge for Aug 1982–2010. White shading is the Aug 2019 mean sea ice extent. (Sources: SST data are from the NOAA OISSTv2; sea ice extent and ice-edge data are from NOAA/NSIDC Climate Data Record of Passive Microwave Sea Ice Concentration, Version 3; Peng et al. 2013; Meier et al. 2017.)

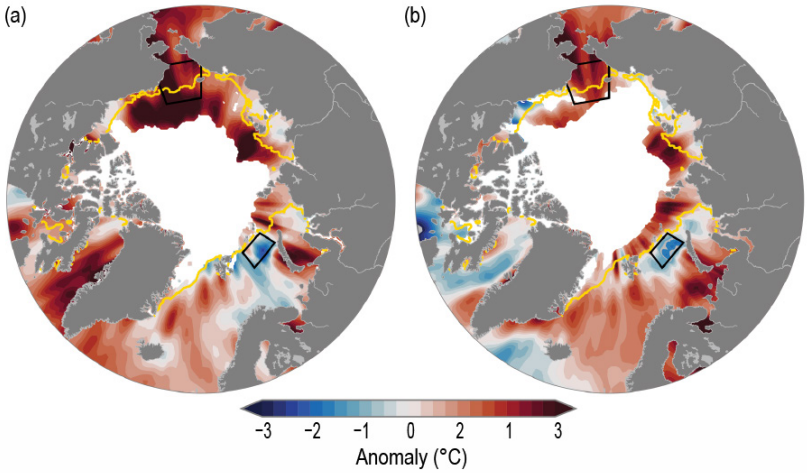

Fig. 5.5. SST anomalies (°C) in (a) Aug 2019 and (b) Aug 2018 relative to the Aug 1982–2010 mean. The yellow line indicates the median ice edge for Aug 1982–2010 and white shading indicates the mean sea ice extent in (a) Aug 2019 and (b) Aug 2018. The two regions marked by black boxes relate to data presented in Figs. 5.6 and 5.7. (Sources: SST data are from the NOAA OISSTv2; sea ice extent and ice-edge data are from NOAA/NSIDC Climate Data Record of Passive Microwave Sea Ice Concentration, Version 3; Peng et al. 2013; Meier et al. 2017.)

warming trends from 1982 to 2019 over much of the Arctic Ocean, with statistically significant (at the 95% confidence interval) linear warming trends of up to +1°C decade^{-1} (Fig. 5.4b). A notable exception was the cooling trend in the northern Barents Sea region, discussed later.

August 2019 mean SSTs were around 1°–7°C higher than the 1982–2010 August mean in the Beaufort, Chukchi, and Laptev Seas and Baffin Bay (Fig. 5.5a). The anomalously high SSTs in the vicinity of the August 2019 mean sea ice edge are linked to anomalously low sea ice extent throughout summer, which allowed for direct solar heating of the exposed surface waters (Fig. 5.5a). Conversely, the entire Barents Sea region was marked by anomalously low August 2019 SSTs that were around 0.5°–2°C lower than the 1982–2010 mean. Relative to August 2018, August 2019 SSTs were up to 4°C higher in the Beaufort Sea and Baffin Bay, while SSTs were a few degrees lower in the Barents Sea in August 2019 compared to August 2018 (Fig. 5.5b).

The Chukchi Sea region continues to exhibit larger warming trends than the Arctic mean (Figs. 5.6a,b), with August 2019 mean SSTs in the region being the second highest on record (Fig. 5.6b). The Bering Sea exhibits a similar warming trend to the Chukchi Sea in August (Fig. 5.6c; see Thoman et al. 2019). A marked exception to the prevalent August SST warming trends across the Arctic is the cooling trend (−0.06 ± 0.03°C yr^{-1}) in the northern Barents Sea (Fig. 5.7a). The statistically significant northern Barents Sea cooling trend is not observed in all months; annually-averaged northern Barents

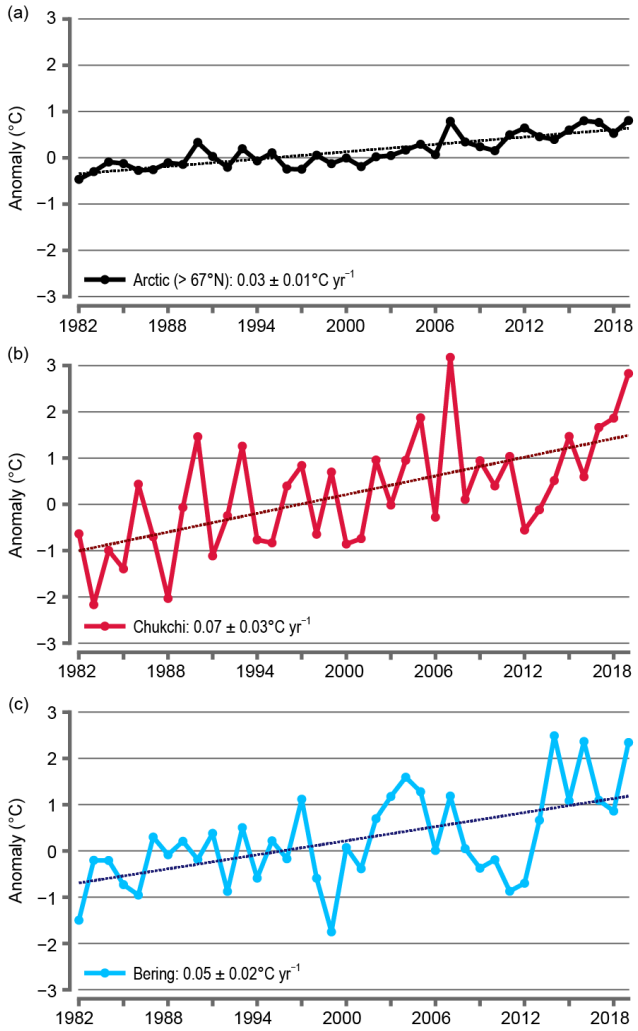

Fig. 5.6. Area-averaged SST anomalies (°C) for Aug of each year (1982–2019) relative to the 1982–2010 Aug mean for (a) the Arctic Ocean north of 67°N; (b) the Chukchi Sea region shown by black box in Fig. 5.5; and (c) the Bering Sea domain bounded by 54°–64°N and 180°–200°E (see Thoman et al. 2019). The dotted lines show the linear SST anomaly trends over the period shown. Numbers in the legends correspond to linear trends in °C yr^{-1} (with 95% confidence intervals).

Sea SSTs exhibit a warming trend, which has been attributed to changes in Atlantic water influence in the region (e.g., see Barton et al. 2018). August mean sea ice extent over the entire Barents Sea domain has been generally declining over 1982–2019 (Fig. 5.7b). If only the northern Barents Sea is considered, there has been little-to-no August sea ice for most years in the past two decades. The interplay between sea ice cover, solar absorption, and lateral ocean heat transport that results in lower August SSTs in the Barents Sea region requires further study.

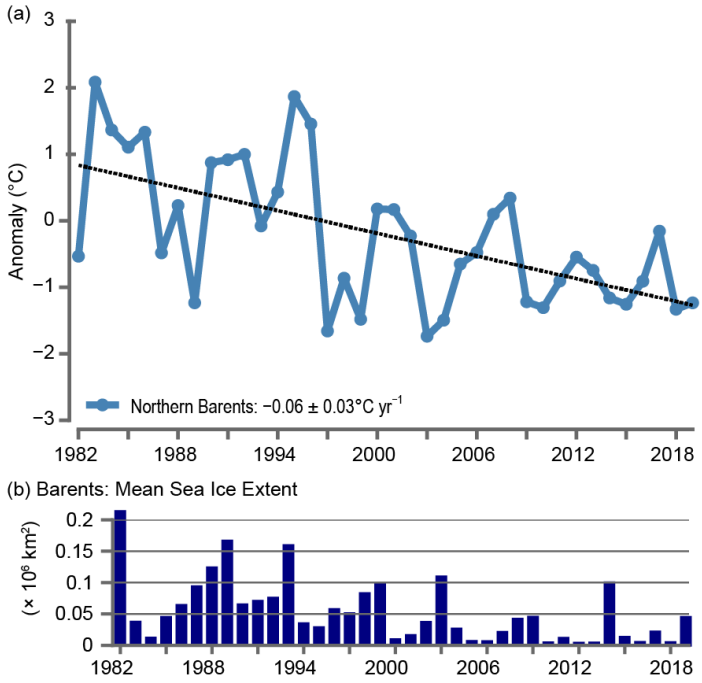

Fig. 5.7. (a) Area-averaged SST anomalies (°C) for Aug of each year (1982–2019) relative to the 1982–2010 Aug mean for the northern Barents Sea region shown by black box in Fig. 5.5. The dotted line shows the linear SST anomaly trend over the period shown. Numbers in the legend indicate the statistically significant linear cooling trend in °C year^{-1} (with 95% confidence interval). (b) Aug sea ice extent calculated over the entire Barents Sea domain. Sea ice extent data are from NSIDC Sea Ice Index, Version 3 (Fetterer et al. 2017) using a regional mask introduced by Meier et al. (2007), available at nsidc.org.

d. Sea ice—D. Perovich, W., Meier, M. Tschudi, K. Wood, S. Farrell, S. Hendricks, S. Gerland, L. Kaleschke, R. Ricker, X. Tian-Kunze, and M. Webster

1) Sea ice extent

Sea ice is an important component of the Arctic system, because it limits the amount of absorbed solar energy due to its high albedo, acts as a barrier between the underlying ocean and the atmosphere, provides a habitat for biological activity, and serves as a platform for Indigenous community hunting and travel. The extent of the Arctic sea ice cover varies substantially during the year, with the end-of-winter ice cover generally being two to three times as large as that at the end of summer. Sea ice extent has been continuously monitored by passive microwave instruments on satellite platforms since 1979, providing a consistent long-term perspective on changing coverage over the last four decades. The sea ice extent estimates used in this report are based on products from the National Snow and Ice Data Center (NSIDC) Sea Ice Index (Fetterer et al. 2017), derived from NASA's gridded sea ice concentration fields (Cavalieri et al. 1996; Maslanik and Stroeve 1999). Other similar products exist and, while absolute numbers vary, they all show general consistency in trends and variability (e.g., Meier and Stewart 2019).

March and September are of particular interest in sea ice time series because Arctic sea ice maximum and minimum extents, respectively, typically occur during these months. Figure 5.8 shows monthly average ice extents in March and September 2019. The sea ice cover reached a winter maximum extent of 14.78 million km^2 on 13 March 2019. This tied with 2007 as the seventh-lowest maximum extent in the 41-year satellite record and was 5.9% below the 1981–2010 average. The previous four years (2015–18) are the four lowest years in the record. From year to year, the regions with a reduced winter sea ice

cover extent are not consistent. For example, in March 2019, the winter maximum sea ice extent in some marginal seas was near normal, such as in the Sea of Okhotsk, while the Bering Sea was 70%–80% lower than normal.

The sea ice cover reached a summer minimum extent of 4.15 million km^2 on 18 September 2019. This tied with 2007 and 2016 as the second-lowest extent of the satellite record and was 2.04 million km^2 (33%) less than the 1981–2010 average minimum ice extent. The September minimum ice extent has not returned to pre-2007 levels; the 13 lowest extents in the satellite record have all occurred in the last 13 years (2007–19).

Observations of Arctic sea ice extent have shown decreasing trends in all months and virtually all regions (Meier et al. 2014). The September monthly average trend for the entire Arctic Ocean is now –12.9 ± 2.2% decade^{-1} relative to the 1981–2010 average (Fig. 5.9), statistically significant at the 99% confidence level. Trends are smaller during March (–2.7% decade^{-1}), but the decrease is also statistically significant. In 2019, the seasonal reduction between the March maximum and September minimum extent was 10.63 million km^2, a change of roughly 72%. The difference between maximum and minimum extents in the satellite record has increased in recent years.

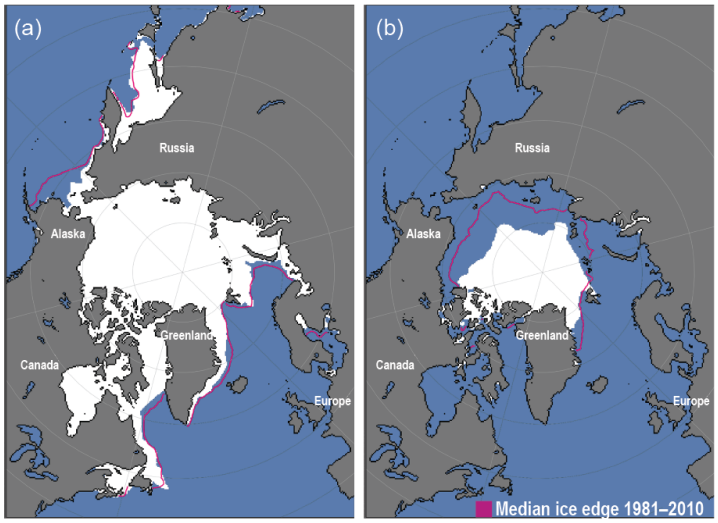

Fig. 5.8. Average monthly sea ice extent in Mar 2019 (left) and Sep 2019 (right) illustrate the respective monthly winter maximum and summer minimum extents. The magenta line indicates the median ice extents in Mar and Sep, respectively, during the period 1981–2010. Maps are from NSIDC at http://nsidc.org/data/seaice_index/ (Fetterer et al. 2017).

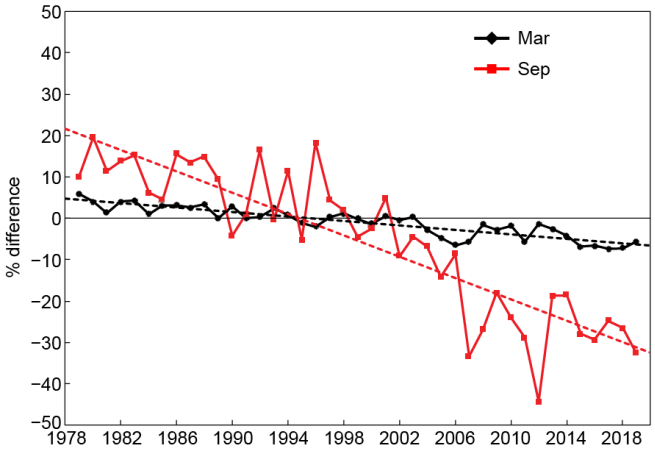

Fig. 5.9. Time series of sea ice extent anomalies in Mar (the month of maximum ice extent, in black) and Sep (the month of minimum ice extent, in red). The anomaly value for each year is the difference (in %) in ice extent relative to the mean values for the period 1981–2010. The black and red dashed lines are least-squares linear regression lines. The slopes of these lines indicate ice losses of –2.7 ± 0.4% and –12.9 ± 2.2% decade^{-1} in Mar and Sep, respectively. Both trends are statistically significant at the 99% confidence level. (Source: NSIDC Sea Ice Index [Fetterer et al. 2017].)

2) Sea ice age

The age of sea ice is also a key descriptor of the state of the sea ice cover. It serves as an indicator for ice physical properties including snow cover, surface roughness, optical properties, melt pond coverage, salinity, and thickness (Tschudi et al. 2016). Older ice tends to be thicker and thus more resilient to changes in atmospheric and oceanic forcing compared to younger ice. The age of the ice has been determined using satellite observations and drifting buoy records that track ice parcels over several years (Maslanik et al. 2011). This method has been used to provide a record of the age of the ice since the mid-1980s (Tschudi et al. 2019 a,b).

The area of the oldest ice (>4 years old) was a substantial fraction of the winter sea ice cover within the Arctic Ocean in the mid-1980s (2.52 million km^2, 33% of the ice pack in March 1985). In

contrast, in 2019 the >4 year-old ice category made up just a small fraction (90 000 km^2, 1.2% in March 2019) of the Arctic Ocean ice pack (Fig. 5.10). First-year ice now dominates the sea ice cover, comprising ~70% of the March 2019 ice pack, compared to approximately 35%–50% in the 1980s. Given that older ice tends to be thicker and stronger, the sea ice cover has transformed from a strong, thick ice mass in the 1980s to a younger, more fragile, and thinner ice mass in recent years. The distribution of ice age in March 2019 was generally similar to that in March of the previous year.

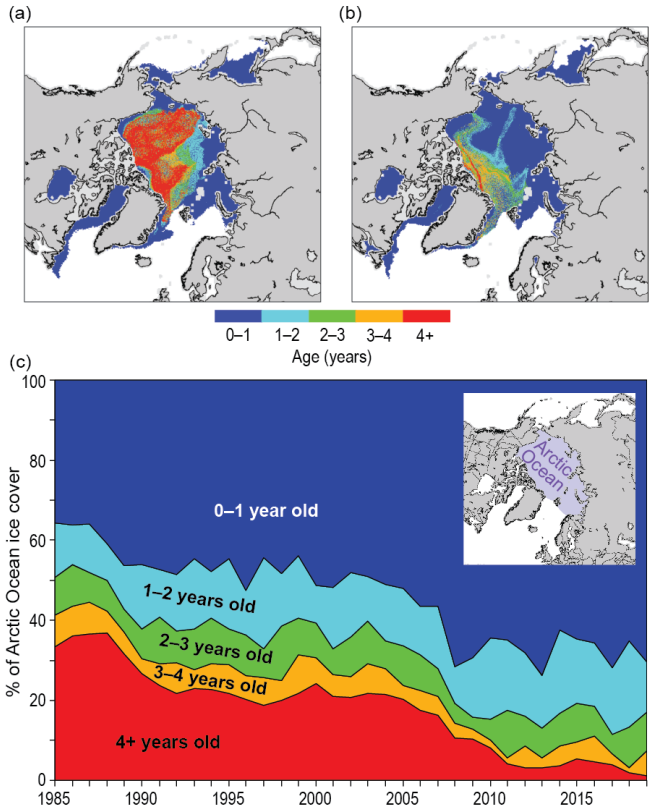

Fig. 5.10. Late winter sea ice age coverage map for the week of (a) 12–18 Mar 1985 (b) and 12–18 Mar 2019 (c) Sea ice age percentage within the Arctic Ocean region (purple shaded region in inset image) for the week of 12–18 Mar 1985 and 2019. (Source: NSIDC [Tschudi et al. 2019a,b].)

3) Chukchi Sea

The Chukchi Sea has experienced particularly large changes in sea ice coverage and is a representative example of extreme sea ice conditions in the Arctic. The September 2019 Arctic sea ice minimum extent was characterized by profound sea ice loss in the Chukchi Sea (Fig. 5.11), due to multiple factors. First, the Bering Sea had extremely low ice cover for much of the winter 2019 (see Sidebar 5.1), which may have acted as a precursor to the summer Chukchi Sea conditions. In spring 2019, melt onset across the Chukchi Sea occurred 20–35 days earlier than the 1981–2010 average. Sea ice began a rapid and accelerating retreat from the south in early May, leading to a record low sea ice extent in the Chukchi Sea that lasted until early August, with negative sea ice concentration anomalies of 50%. A combination of anomalously warm air temperatures (1°–5°C above the 1981–2010 average) and southerly winds promoted this precipitous loss of ice (section 5b). As the sea ice retreated northward, exposed open water areas warmed, leading to anomalous SSTs in summer 2019 greater than 5°C above average (section 5c).

The dearth of sea ice continued into the autumn season, accompanied by anomalously warm air temperatures of 4° to 5°C above the 1981–2010 average during October and November 2019 (section 5b). The warm air temperatures were partly due to very warm ocean waters, with SSTs remaining at 5°C or more above average in the Chukchi Sea well into November. The Chukchi Sea did not fully freeze over until 24 December, about a month later than average, with only 2007 and 2016 showing similarly late freeze-up dates since modern satellite observations began in 1979.

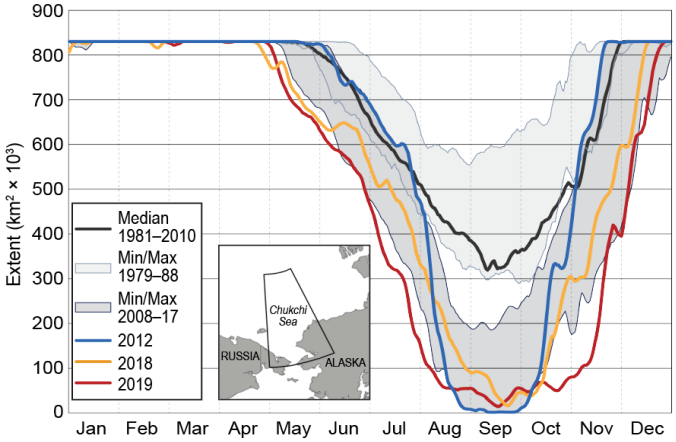

Fig. 5.11. Time series of 2019 sea ice extent in the Chukchi Sea (see inset) through 12 Nov (red line) compared to the previous year (2018; yellow line); the record minimum year (2012, blue line), and the climatological median (1981–2010; black line), derived from satellite passive-microwave data. The gray shaded areas show the maximum range of variability of sea ice extent for the first decade of the satellite era (1979–88) and the most recent decade (2008–17), illustrating the long-term change in sea ice extent over the entire period since 1979. (Source: NSIDC Sea Ice Index, version 3 [Fetterer et al. 2017].)

SIDEBAR 5.1: **Shifting fish distributions in the Bering Sea**—J. M. MARSH, F. J. MUETER, J. T. THORSON, L. BRITT, AND S. ZADOR

The eastern Bering Sea is a highly productive ecosystem that supports many subsistence and commercial fisheries. These commercial fisheries are some of the most valuable in the world, with annual wholesale revenue exceeding $1 billion (U.S. dollars; Fissel et al. 2019). To support sustainable management and assess overall ecosystem health, yearly summer bottom-trawl surveys in the southeastern Bering Sea have monitored the abundance and biomass of demersal (living on the seafloor) fishes and invertebrates since 1982 (NPFMC 2018). To study impacts of the loss of seasonal sea ice on the Bering Sea ecosystem, the surveys were expanded in 2010 and 2017–19 to include the northern Bering Sea, a transitional zone between the North Pacific Ocean and the Arctic Chukchi Sea.

On the Bering Sea shelf, the summer distribution of demersal fishes and invertebrates is tied to the extent of the cold pool (bottom water temperatures < 2°C). The cold pool forms during autumn freeze-up when cold dense water sinks to the seafloor where it persists throughout the following summer, even as the surface waters undergo seasonal warming. The size of the cold pool is dependent on the extent of sea ice in the Bering Sea during the preceding winter (Wyllie-Echeverria and Wooster 1998), and it can serve as a thermal barrier to boreal (southern Bering Sea) fish expansion into the Arctic. Until recently, it was expected that sea ice would continue to persist throughout the winter over the shallow northern Bering Sea and southern Chukchi Sea shelf, enabling the formation of the cold pool (Stabeno et al. 2012). However, latent heat in the water column from the warm conditions of summer 2016, combined with less sea ice formation in the 2016/17 winter (Thoman et al. 2020), resulted in an unusually narrow cold pool on the eastern Bering Sea shelf during summer 2017. Sea ice extent was further reduced in the 2017/18 and 2018/19 winters with the lowest coverage on record for February and March, respectively (<40% of average conditions; Stabeno and Bell 2019; Stabeno et al. 2019). This led to a considerable reduction (>75%) in the size of the cold pool during the summers of 2018 and 2019 (Fig. SB5.1).

These changes in the physical environment are expected to affect the distribution of fish and invertebrate communities. In general, fish populations are expected to remain within their preferred thermal conditions by shifting their spatial distributions to track changes in ocean temperatures (Pinsky et al. 2013). Therefore, within a warming marine environment, boreal fish populations in the Bering Sea are expected to expand northward into new areas (Hollowed et al. 2013), while cold-adapted species may contract.

We compare the spatial distribution of five assemblages (groups of co-occurring species) in the Bering Sea during the 2017–19 warm period, relative to the cooler conditions of 2010 (Fig. SB5.1). These assemblages represent three boreal fish communities from the outer, middle, and inner shelf, a mixed community in Norton Sound, and an Arctic community on the northern shelf. Following a drastic reduction in the size of the

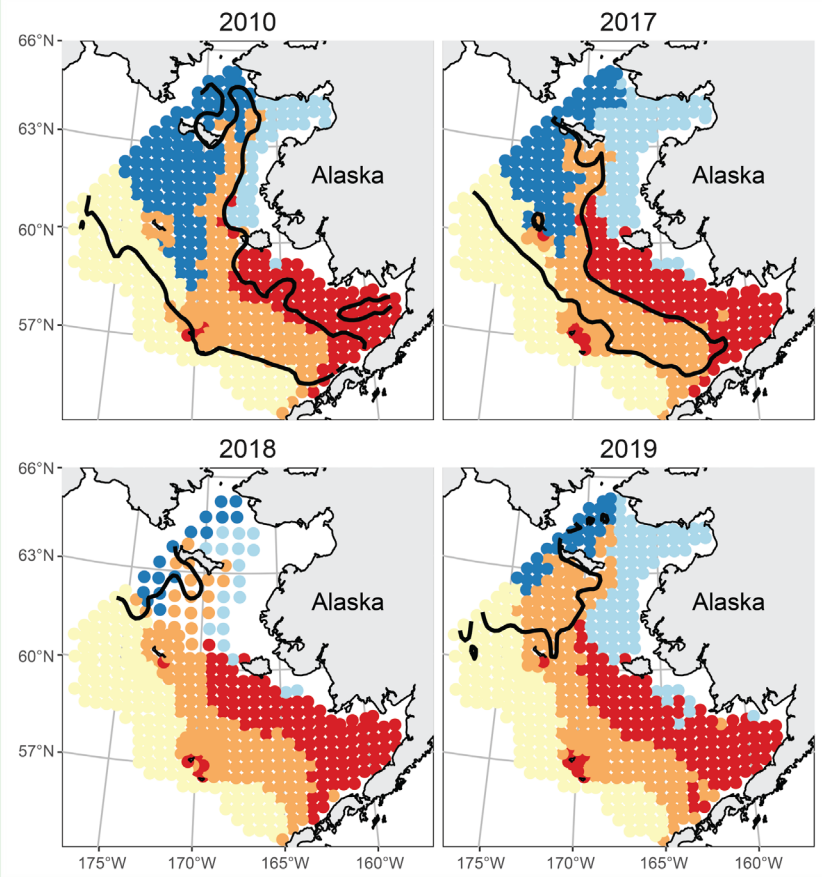

Fig. SB5.1. Distribution of major species assemblages identified in the eastern Bering Sea during the summers of 2010, 2017, 2018, and 2019, including three boreal assemblages on the southern inner shelf (red), middle shelf (orange), and outer shelf/slope region (yellow), as well as a mixed Norton Sound (light blue) and an Arctic/northern shelf assemblage (dark blue). See Thorson et al. (2019) for a description of clustering methods used on catch-per-unit-effort (kg ha^{-1}) of 44 common species caught in 1983 hauls. The contour (black) denotes the 2°C isotherm of bottom water temperature, which marks the boundary of the cold pool.

cold pool in 2018 and 2019, the middle-shelf (boreal) assemblage expanded northward while the northern shelf (Arctic) assemblage retracted. At the same time, the inner shelf and Norton Sound assemblages expanded offshore in 2018 and 2019, coinciding with warmer coastal water temperatures, particularly in 2019. These community-level shifts, which reflect changes in the distribution of individual species, result in a large portion of the shelf transitioning from an Arctic community, dominated by relatively smaller and less abundant species (e.g., Arctic cod; *Boregadus saida*), to a community dominated by larger and more abundant boreal species (e.g., Pacific cod; *Gadus macrocephalus*).

Changing distributions are also illustrated by mapping the density (biomass per unit area) of four individual gadid (cod family) species in the Bering Sea (Fig. SB5.2). We selected two boreal species that support high-value commercial fisheries, walleye pollock (*Gadus chalcogrammus*) and Pacific cod, and two smaller gadids, Arctic cod and saffron cod (*Eleginus gracilis*), which are key indicator species for the northern shelf (Arctic) and Norton Sound assemblages, respectively. Both walleye pollock and Pacific cod shifted northward between bottom-trawl surveys conducted in 2010 and repeated in 2017, 2018, and 2019. Hotspots of increased density in the later years are apparent for Pacific cod south of St. Lawrence Island (63°N, 170°W) and for pollock south of the Bering Strait (64°N, 172°W). The locations of these hotspots on the northern Bering Sea shelf have contributed to a rapid northward shift in the center of population for these commercially important species (Stevenson and Lauth 2019). These results also show that the areas with the greatest changes vary from species to species, and that northward shifts in boreal species can occur even while their densities remain high within the southern portion of their range. A similar "borealization" of the fish community has occurred in the Barents Sea, as increasing water temperatures and retreating ice cover have opened new feeding habitats for Atlantic cod (*Gadus morhua*) and haddock (*Melanogrammus aeglefinus*), two commercially important cod species (Fossheim et al. 2015; Thorson et al. 2019).

Compared to these boreal species, Arctic taxa tend to be more sensitive to habitat changes. Arctic cod in particular can serve as a sentinel species that responds quickly to changes in water temperature and sea ice extent (Alabia et al. 2018; Marsh and Mueter 2019). Correspondingly, we saw roughly 92% and 78% reductions in the area occupied by Arctic cod when comparing 2010 to 2018 and 2019, respectively (Figs. SB5.2i–l), while saffron cod, an indicator for the Norton Sound assemblage, has expanded westward and southward along the coast (Figs. SB5.2m–p).

The expansion of nearshore "Norton Sound" and southern shelf species into the northern Bering Sea is likely to have profound effects from predation on the benthic ecology of the northern Bering Sea—effects that are yet undocumented. The observed high densities of fish in the Bering Strait suggest that boreal species may shift their summer feeding migrations into the Chukchi Sea, which has also seen large decreases in summer and autumn sea ice extent (section 5d). Such potential movement northward into the Chukchi Sea highlights the need for additional fisheries surveys north of the Bering Strait, as well as continued surveys in the Bering Strait region and a synthesis of data from both the United States and Russian waters. In this report, we have presented only a limited four years of survey data from the U.S. Bering Sea.

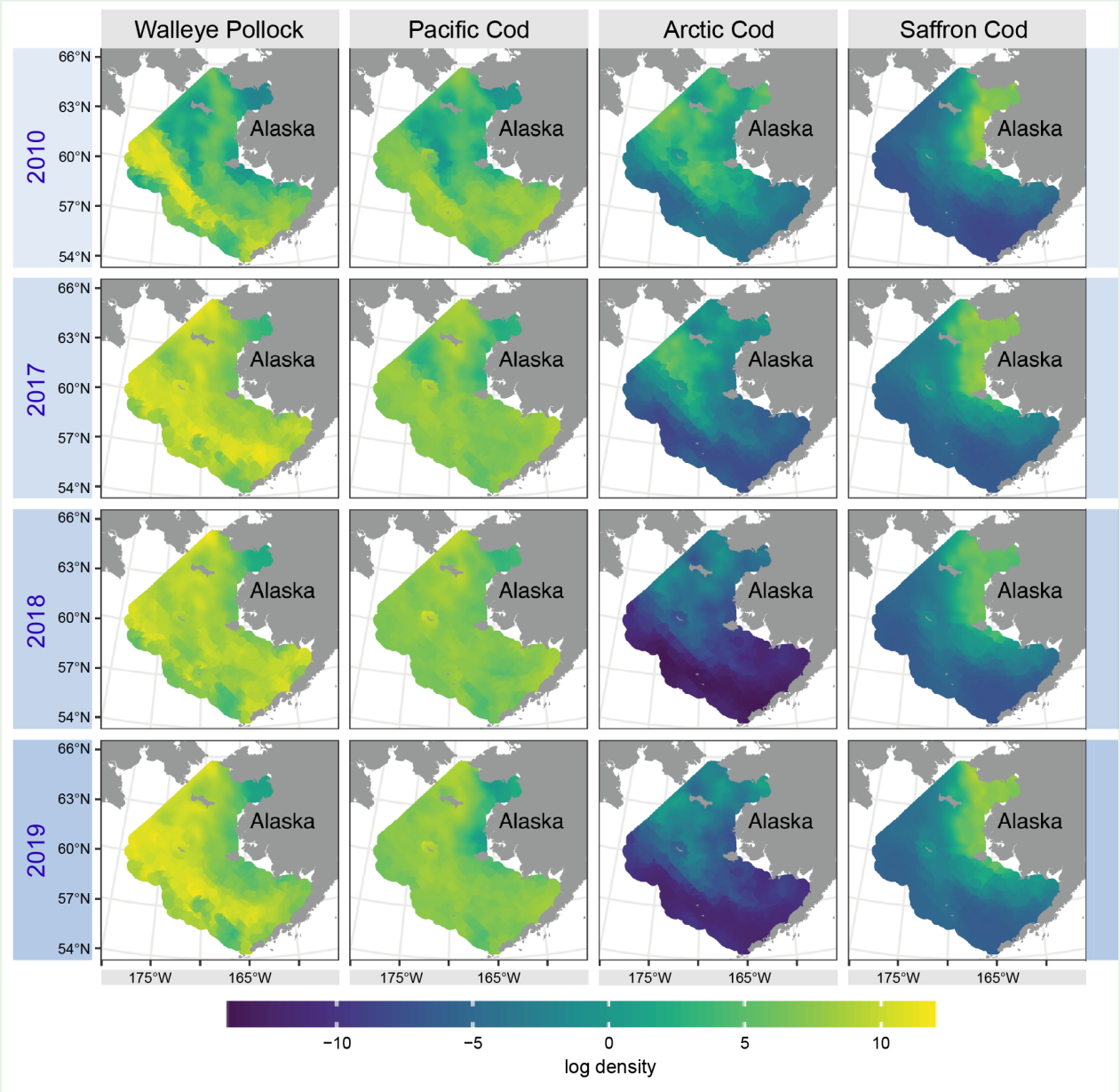

Fig. SB5.2. Density estimates (kg km^{-2}, log-scale) for four gadids (cod family) on the eastern and northern Bering Sea shelf in 2010 and 2017–19, the only years with standardized bottom-trawl survey data for the northern Bering Sea. The highest densities for each species are depicted in yellow, intermediate in green, and the lowest are blue. Estimates are generated using a spatio-temporal delta-model (Thorson 2019 using methods in Thorson et al. 2019).

e. Greenland ice sheet—T. A. Moon, M. Tedesco, J. K. Andersen, J. E. Box, J. Cappelen, R. S. Fausto, X. Fettweis, B. Loomis, K. D. Mankoff, T. Mote, C. H. Reijmer, C. J. P. P. Smeets, D. van As, R. S. W. van de Wal, and Ø. Winton

The Greenland ice sheet (GrIS) sits atop the largest island in the world and contains the equivalent of 7.4 m of global mean sea level rise (Morlighem et al. 2017). While the GrIS was likely in balance (i.e., ice mass gain was balancing ice mass loss) during the 1970s, 1980s, and early 1990s, it began to lose mass in earnest in the mid- to late-1990s (Mouginot et al. 2019). As Greenland loses ice, cold, fresh meltwater is added to the ocean, which increases sea levels and also impacts ocean properties and circulation (e.g., Luo et al. 2016); alters nutrient and sediment fluxes (e.g., Cape et al. 2018; Overeem et al. 2017); and influences local ecosystems (e.g., Hopwood et al. 2018). Observations of the GrIS over the "balance year" of accumulation and loss, from September 2018 through August 2019, reveal another year of dramatic ice melt. The extent and magnitude of ice loss in 2019 rivaled 2012, the previous record year of ice loss.

1) Surface air temperatures, surface mass balance, and albedo

During September 2018–August 2019, overall high air temperatures, low snow accumulation, extensive ice melt, and low surface albedo led to strong deficits in ice sheet surface mass balance. Measurements at 20 Danish Meteorological Institute (DMI) Program for Monitoring of the Greenland Ice Sheet (PROMICE) weather stations near the ice sheet periphery indicated widespread above- or near-average air temperatures during winter 2018/19 (December–February, DJF), spring 2019 (March–May, MAM), and summer 2019 (June–August, JJA) (Cappelen 2020). At Summit Station, located in the high-elevation ice cap interior (elevation 3162 m), autumn 2018 and winter 2018/19 were colder than average, while spring and summer 2019 were warmer than average.

Roughly 95% of the GrIS surface experienced melting at some point during the 2019 melt season, which is significantly greater than the 1981–2010 average melt extent of ~64%. While the maximum daily extent of ice sheet surface melt in 2019 only reached 60.3% on 31 July (Fig. 5.12a), compared to 90% in 2012 on 11 July, the cumulative 2019 summer melt extent matched the 2012 values (the previous record melt year). Satellite-derived observations indicate that surface melt in 2019 started in mid-April, six to eight weeks before the long-term average (1981–2010 average). Similar conditions occurred in 2012, when melting started as early as the beginning of April. Except for a small area in the southeast, melt duration in 2019 also exceeded the 1981–2010 mean across the ice sheet ablation zone, the area of net surface ice loss around the ice sheet periphery (Fig. 5.12b).

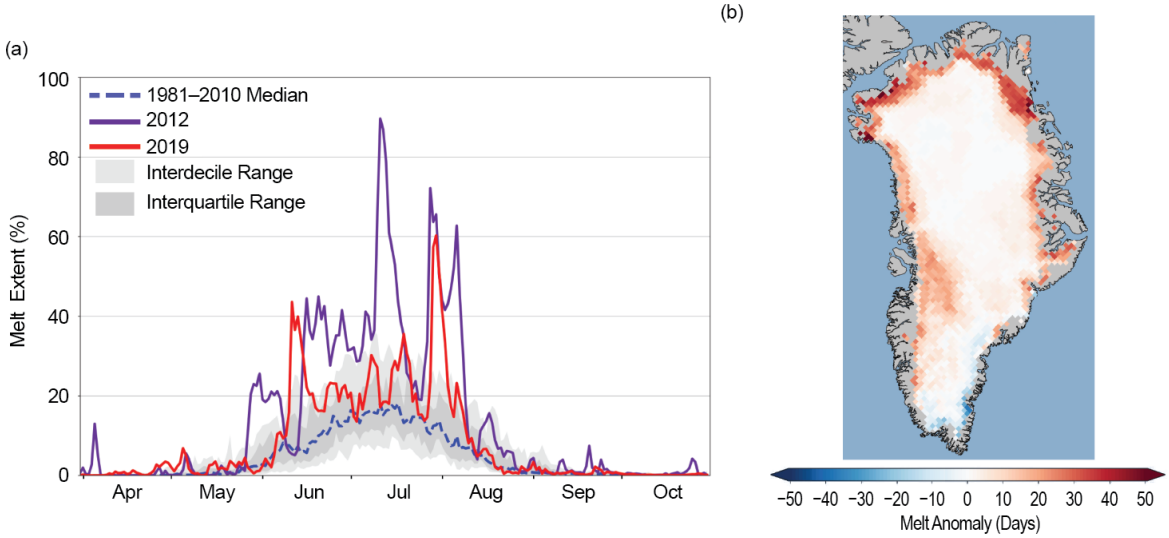

Fig. 5.12. (a) Surface melt area as a percentage of the ice sheet area during 2019 (solid red) and 2012 (solid purple). Also shown are the 1981–2010 median (dashed blue) and interdecile and interquartile ranges (shaded). (b) Summer 2019 melt anomaly (in number of melting days) with respect to the 1981–2010 period. (Source: Observations derived from brightness temperatures measured by the SSMIS passive microwave radiometer [e.g., Mote 2007; Tedesco et al. 2013].)

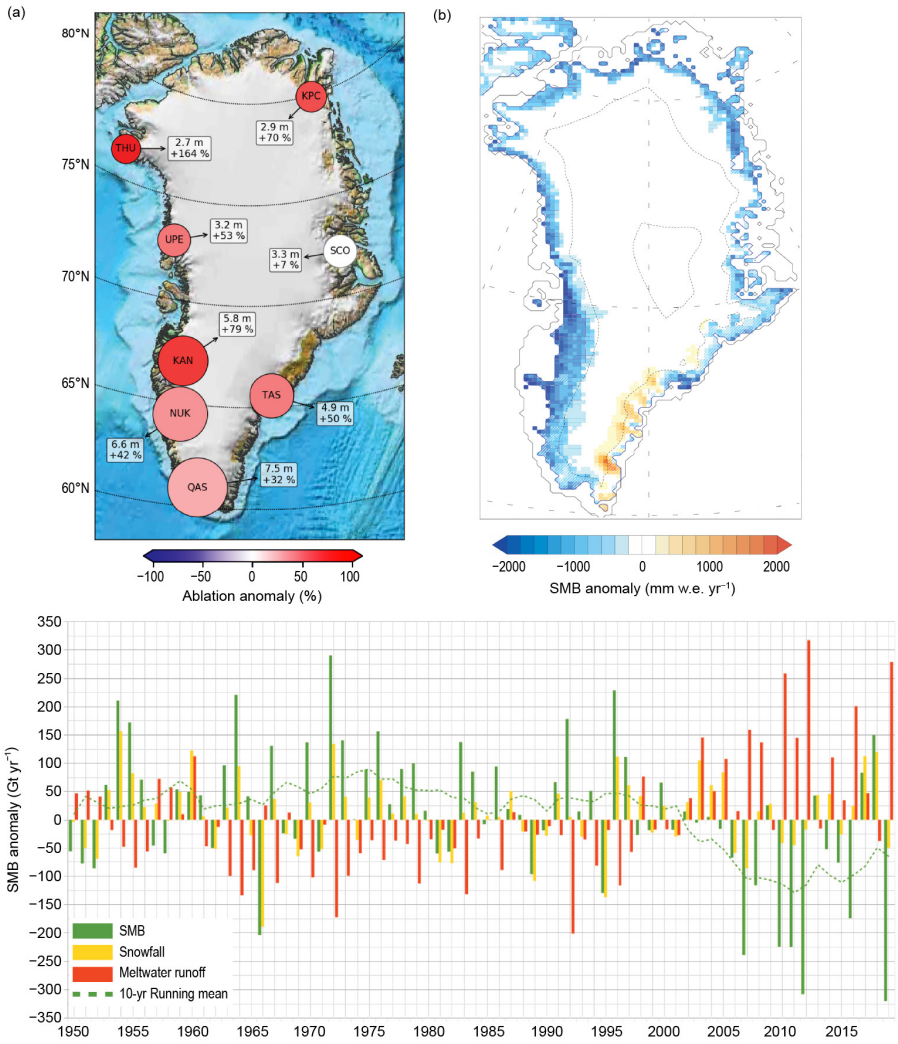

Fig. 5.13. (a) Net ablation in 2019 measured by PROMICE weather stations along the GrIS margin, following van As et al. (2016; https://www.promice.dk/). Circle size represents the ablation in meters of ice equivalent (m), and color represents anomaly value (%). White circles indicate anomaly values not exceeding methodological and measurement uncertainty. (b) 2019 Greenland surface mass balance anomaly (mm w.e. yr^{-1}) simulated by MARv3.10. (c) Surface mass balance anomaly (Gt yr–1) for Sep–Aug balance year using MARv3.10 forced by the reanalysis NCEP–NCARv1 climate data during 1948–2019. All plots are relative to 1981–2010 reference period.

Observations from the DMI-PROMICE ablation area weather stations provide additional evidence of the high degree of surface melt during 2019 (Fausto and van As 2019). The 2019 net ice ablation exceeded the 2008–19 PROMICE average at all 18 sites, as well as the 1981–2010 average; melting was particularly notable in the southwest (+79 ± 20%), northwest (+164 ± 49%), and northeast (+70 ± 30%) (Fig. 5.13a).

Surface mass balance simulations from the Modèle Atmosphérique Régionale (MAR; Fettweis 2007) show that the September 2018–August 2019 total surface mass balance was the lowest since 1948, with a normalized anomaly of –3.2 with respect to the 1981–2010 mean. The normalized anomaly is the anomaly divided by the 1981–2010 interannual variability (Figs. 5.13b,c), gauged here by the standard deviation, and is considered statistically significant for values > +2 or < –2 (i.e., more than two times the interannual variability). Low surface mass balance is mainly due to lower accumulation than average (normalized anomaly of –0.8) and significantly higher surface melt than normal (normalized anomaly of +3.0; the second record high after 2012; Tedesco and Fettweis 2019).

Surface albedo, which is the fraction of incident sunlight reflected by a surface, is estimated from spaceborne Moderate Resolution Imaging Spectroradiometer (MODIS) measurements (after

Box et al. 2017). The surface albedo in JJA 2019 averaged 77.7% over Greenland land ice, the second lowest in the 20-year record (2000–19) after 2012 (76%). Especially low albedo along the western and northern ice sheet margins is consistent with the thin snow cover and significant early melt in 2019. The 2000–19 trend for summer broadband albedo from MODIS is –1.0% ± 1.0 per year, although this is insignificant at the 5% level.

During JJA 2019, a mean normalized North Atlantic Oscillation (NAO) index value of –1.8 suggests a dominance of anticyclonic atmospheric circulation, which favored (1) dry, sunny conditions over the south and central part of the ice sheet, enhancing the surface melt-albedo feedback (Tedesco and Fettweis 2019); and (2) advection of warm and moist air masses through the Baffin Sea toward the northern ice sheet. The MAR regional climate simulations suggest a record loss in the surface mass balance in 2019, although meltwater runoff was lower in 2019 than 2012 (Figs. 5.13b,c; section 5b). Exceptional northern melt was driven by anomalously high longwave downward radiation due to clouds, while exceptional southern and central melt was a consequence of lower albedo and higher solar incoming radiation due to reduced cloudiness (normalized anomaly for JJA solar radiation was +3.0, which is statistically significant).

2) Glacier retreat and ice discharge

Along with losing ice mass via surface melt, Greenland also loses mass through the direct discharge or loss (calving) of solid ice (icebergs) into the ocean from marine-terminating glaciers. PROMICE estimates for the GrIS indicate that 2019 solid ice discharge averaged 498 ± 50 Gt yr^{-1}, ~4% above the 1986–2010 average of 480 ± 48 Gt yr^{-1}. The discharge from most regions has been approximately steady or declining for the past decade, pointing to mass balance associated with surface melting as the major source for increasing ice loss (Figs. 5.14a,c). The largest discharge

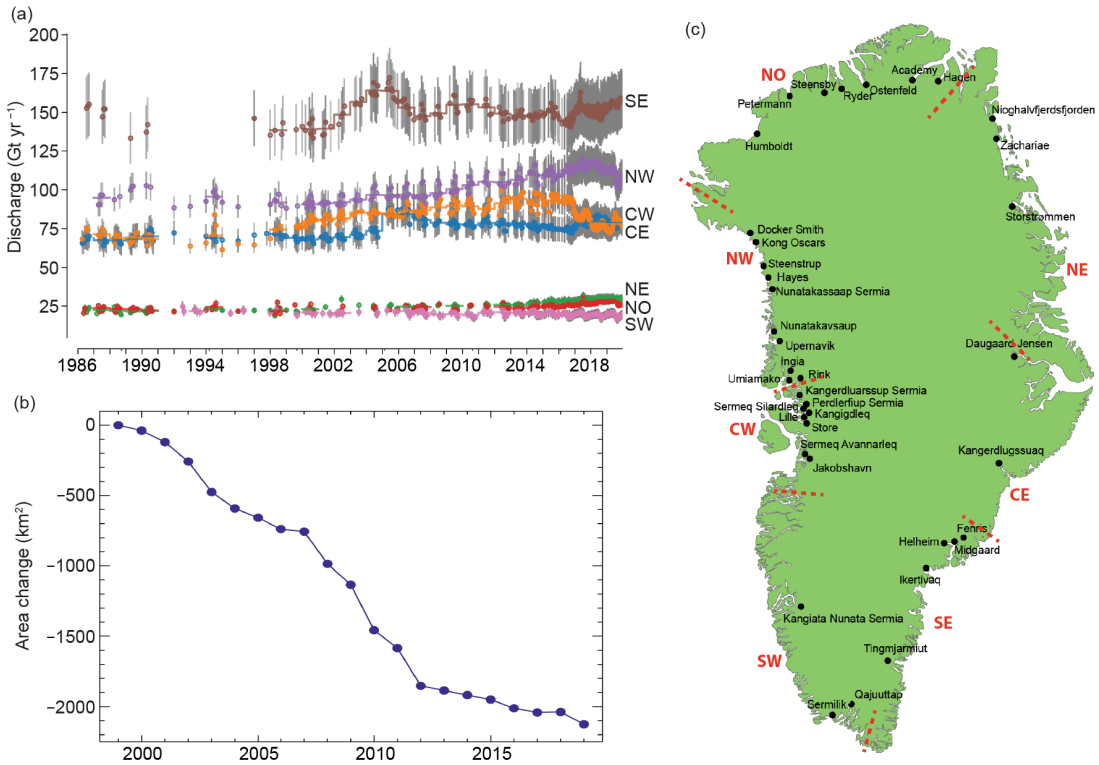

Fig. 5.14. (a) Time series of ice discharge (Gt yr^{-1}) from the GrIS to the ocean via calving. Dots represent when observations occurred. Gray bars show ±10% uncertainty range. (b) Cumulative annual net glacier area change (km^2) at 47 major marine-terminating glaciers of the GrIS ice sheet from 1999/2000 to 2018/19, measured using Sentinel-2, LANDSAT, and ASTER satellite optical imagery (after Andersen et al. 2019). (c) GrIS map indicating the regions used for (a) with red dashed border zones and red labels for the southeast (SE), southwest (SW), central west (CW), northwest (NW), north (NO), northeast (NE), and central east (CE), and the 47 glaciers used for (b) with black dots and labels.

is from the southeast, which discharged a high of 164 ± 19 Gt in 2004, dropped to 145 ± 18 Gt in 2016, and then increased to 158 ± 18 Gt in 2019. The northwest exhibited a relatively persistent increase in discharge from the 1990s through 2016, with a slight decrease during 2017–19. The 1998 discharge was ~89 Gt yr^{-1} compared to a 2019 discharge of 115 Gt yr^{-1} (23% increase). The discharge in the central west, which is dominated by Sermeq Kujalleq (Jakobshavn Isbræ), has seen an almost 20% decrease over the past two years.

Satellite-derived measurements of annual advance or retreat at 47 marine-terminating glaciers since 1999 (Figs. 5.14b,c) indicate that the 2018/19 average net area change was a loss of 87.2 ± 1.7 km^2 (i.e., glacier retreat) with a cumulative net area loss of 2125.6 ± 42.5 km^2. The 2018/19 area loss is a slight uptick over year-to-year changes during 2013–18.

3) Total mass balance

NASA's Gravity Recovery and Climate Experiment (GRACE; 2002–17) and GRACE-Follow-On (FO; 2018–present) satellite missions have revolutionized our ability to monitor ice loss by providing monthly estimates of total ice sheet mass (surface mass balance plus solid ice discharge). The GRACE-FO mission was launched on 22 May 2018, creating a measurement gap from July 2017 through May 2018. The total ice mass loss trend for the GRACE period (April 2002–June 2017) is –282 ± 14 Gt yr^{-1} (Fig. 5.15). The updated mass loss trend for the combined GRACE and GRACE-FO period (April 2002–December 2019) is –269 ± 19 Gt yr^{-1}, indicating continuing substantial ice loss equal to roughly 0.7 mm yr^{-1} of global average sea level rise. While there are no GRACE measurements prior to 2002, a recent study of Greenland mass loss during 1972–2000 (Mouginot et al. 2019) suggests that decadal mass change rates during this time ranged from +47 ± 21 Gt yr^{-1} (mass gain) during 1972–80 to –51 ± 17 Gt yr^{-1} (mass loss) during 1980–90. Across all metrics, 2019 has proved to be another year of substantial Greenland ice loss.

Fig. 5.15. Gravity-derived estimates (blue dots with yellow circles) of total mass change (Gt) of the GrIS between Apr 2002 and Dec 2019 determined from GRACE (2002–17) and GRACE–FO (2018–19) JPL RL06 Level 2 solutions (using techniques from Wahr et al. (1998); 2-std. dev. model fit uncertainties reported), with linear interpolation (blue dots). The following corrections have been applied: Geocenter (Technical Note 13); C20 and C30 (Technical Note 14); glacial isostatic adjustment (ICE-6G_D).

f. Glaciers and ice caps outside Greenland—G. J. Wolken, B. Wouters, M. Sharp, L. M. Andreassen, E. H. Baker, D. Burgess, J. Kohler, B. Luks, and S. O'Neel

Land areas in the Arctic, outside Greenland, host numerous glaciers and ice caps. Although their potential, longer-term contribution to sea level rise is small compared to the ice sheets of Antarctica and Greenland, these smaller land ice masses are sensitive to changes in climate and have been a large contributor to recent sea level rise in response to continued atmospheric warming (Gardner et al. 2011, 2013; Jacob et al. 2012; Millan et al. 2017; Wouters et al. 2019). Observations of glaciers and ice caps from 2018 and 2019 show regional variations in mass change and a continuing trend of significant ice loss throughout the Arctic and especially in Alaska and Arctic Canada.

Glaciers gain mass by snow accumulation and lose mass through surface melt and runoff as well as iceberg calving, where they terminate in the ocean or a lake. The annual climatic mass balance (B_{clim}) is a widely used index that describes the state, or health, of a glacier. B_{clim} is defined as the difference between the annual mass gain by snow accumulation and the annual mass loss by surface melting and runoff. The annual mass balance is traditionally measured over

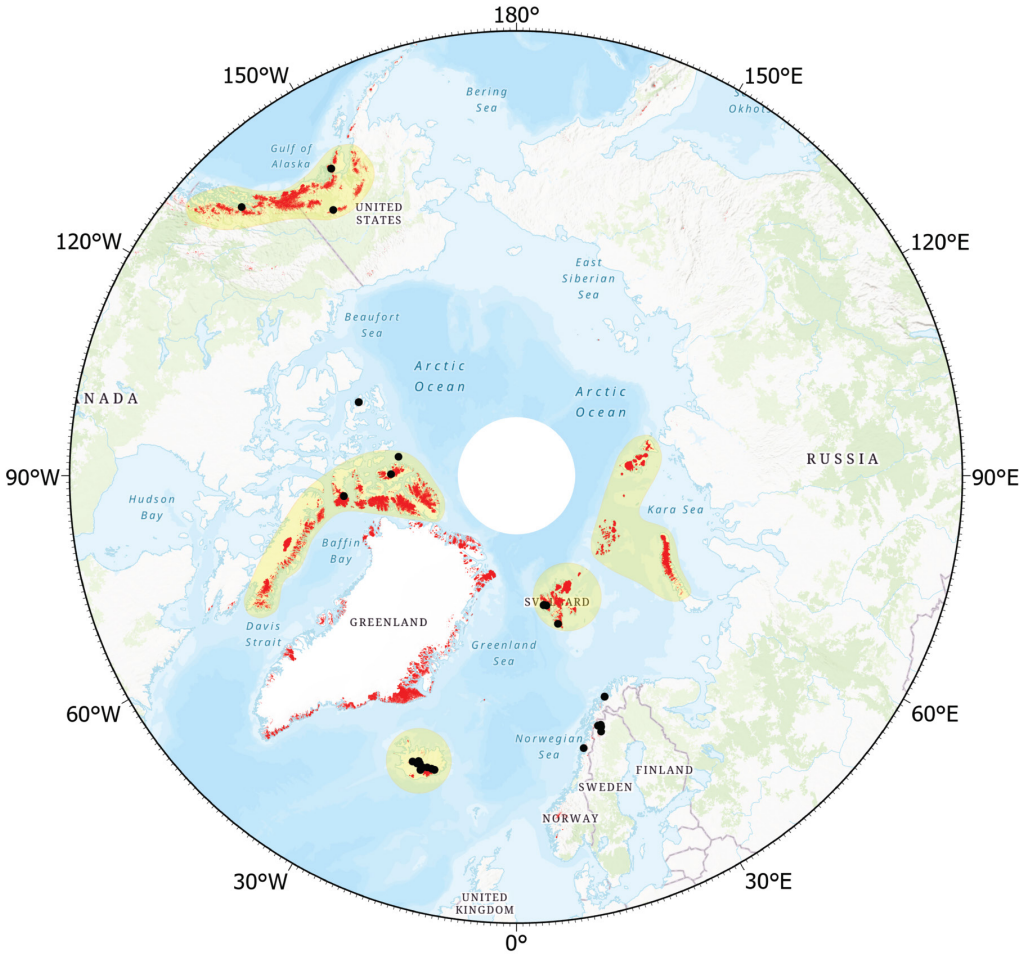

Fig. 5.16. Arctic glaciers and ice caps (red), including ice caps in Greenland separate from the ice sheet. Yellow shading shows the GRACE- and GRACE-FO-derived mass anomaly domains used to estimate changes in regional annual glacier mass balance for the heavily glacierized regions of the Arctic.

a "balance year" that, in the Arctic, is often operationally defined to extend from September to August of the following year. Positive annual mass balance values indicate a gain in mass over the balance year, whereas negative mass balance values indicate a loss in mass. The total mass balance is given by the mass gain by snow accumulation plus the mass losses by runoff and iceberg calving. Of the 27 glaciers currently monitored for mass balance across the Arctic (Fig. 5.16), only three (Kongsvegen, Hansbreen, and Devon Ice Cap) are tidewater glaciers, which lose mass by iceberg calving into the ocean.

In this section, we report on B_{clim} measurements for the mass balance year 2018/19 from 10 of the 27 monitored Arctic glaciers (three in Alaska, four in Svalbard, two in Norway, and one in Arctic Canada). The limited data availability of measurements for 2018/19 is due to latency in seasonal measurements at some glaciers and because some of these data are still provisional. To provide a more complete picture, we also report on 25 glaciers for the mass balance year 2017/18 (World Glacier Monitoring Service [WGMS] 2017; Kjøllmoen et al. 2019), building on observations for the mass balance years 2015/16 and 2016/17, which were reported the last time this section appeared, in *State of the Climate in 2017* (Sharp et al. 2018). For the Arctic as a whole, the mean B_{clim} values for 2017/18 and 2018/19 were negative, indicating overall mass loss.

In 2017/18, 16 of the 25 glaciers (64%) registered negative balances (in Alaska, Svalbard, and northern Scandinavia) and nine (36%) registered positive balances (in Arctic Canada and Iceland). Relative to the long-term (1985–2015) mean values of B_{clim}, 12 of the 25 were more negative and 13 were more positive than the mean. The B_{clim} values reported for glaciers in 2018/19 (Alaska, Svalbard, Norway, and Arctic Canada) were all more negative than the long-term mean, with mass

balance data from Alaska showing extremely negative values. This was the seventh consecutive year of strongly negative anomalies in the Alaska region. The positive anomalies observed for the nine individual glaciers during 2017/18 contrast with the mainly negative annual mass balance anomalies that have driven the current trend of continued mass loss observed throughout the Arctic since the mid-1950s (Fig. 5.17). With the exception of the Svalbard region (where there has been no obvious recent acceleration of mass loss rates), rapid mass loss across the five regions generally began during the 1990s (van Pelt et al. 2019; Zemp et al. 2019).

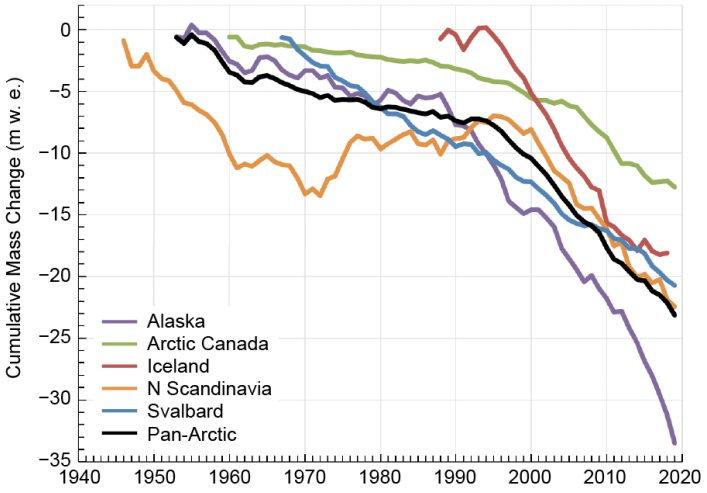

Fig. 5.17. Cumulative B_{clim} in meters of water equivalent (m w.e.) for monitored glaciers in five regions of the Arctic and for the Arctic as a whole (Pan-Arctic). Mean balances are calculated for glaciers monitored in each region in each year and these means are summed over the period of record. Note that monitoring periods vary between regions and that the number and identity of glaciers monitored in a given region may vary between years. (Source: WGMS 2017.)

Air temperature exerts a strong control on surface mass balance in the Arctic. Positive balance anomalies in Arctic Canada and Iceland during 2017/18 were likely influenced by frequent low-pressure systems in the central Arctic generating persistent cloud cover that reduced solar heating during summer (Overland et al. 2019). The negative balances of glaciers in Alaska, northern Scandinavia, and Svalbard in 2017/18 were most likely linked to melt increases caused by positive air temperature anomalies during autumn from the surface to 850 hPa, relative to the 1981–2010 climatology (data from NCEP–NCAR Reanalysis; Overland et al. 2019). Negative balance values reported for glaciers in Alaska, Arctic Canada, and Svalbard in 2018/19 were also associated with anomalously high air temperatures at 850 hPa and persistent ridges of high pressure over Arctic Russia, Arctic Canada, and Alaska. Strongly positive air temperature anomalies (2.5°–3.5°C at 1000–850 hPa) in 2018/19, associated with southerly winds and warm air (section 5b), produced the most negative mass balance year on record for the combined Alaska glaciers. For example, the 2019 average summer air temperature at Wolverine Glacier in south-central Alaska was 11.1°C, marking the hottest summer in the 52-year record and 3.2°C higher than the 1981–2010 climatological mean (Fig. 5.18). Over the period of record at Wolverine Glacier (1967–2019), mean

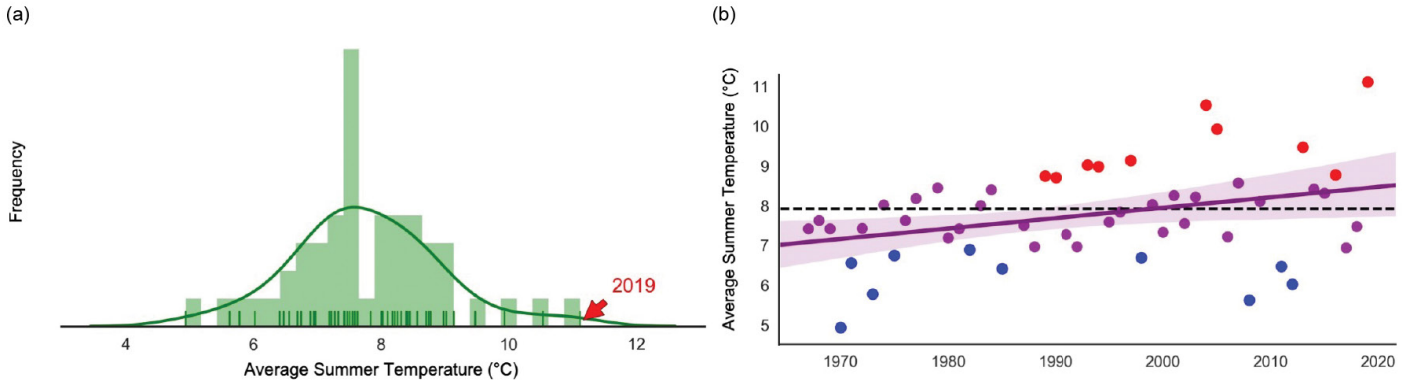

Fig. 5.18. Summer air temperatures at Wolverine Glacier, Alaska, from 1967 to 2019, at 990-m a.s.l. The summer season is defined as Jun, Jul, and Aug following Bieniek (2017). (a) Distribution of mean summer temperatures, shown with a histogram (bar plot) and kernel density estimate (smoothed curve). Small vertical lines show each individual year's summer temperature. Summer 2019 is labeled for emphasis. (b) Time series of mean summer temperature, with the 10 warmest years shown as red dots and the 10 coldest years shown as blue dots. An ordinary least squares trend line is fit through all data and is shown in purple ($p < 0.02$ for Kendall-tau trend test). Light purple shading indicates uncertainty.

summer temperatures have increased 1°C, at a rate of 0.02°C yr^{-1} ($p < 0.02$ for Kendall-tau trend test; O'Neel et al. 2019).

Time series of cumulative regional mass anomalies, derived using GRACE (2002–17) and GRACE-FO (2018–present) satellite gravimetry (see also section 5e), can be used to estimate changes in regional annual glacier mass balance for the heavily glacierized regions of the Arctic (Fig. 5.16; Wouters et al. 2019). For the Arctic glaciers and ice caps as a whole, the overall mass balance was strongly negative during the combined GRACE and GRACE-FO period (2002–19), with the signal dominated largely by ice mass loss from Alaska and Arctic Canada (Fig. 5.19). The estimated mass loss trends during this period for five regions in the Arctic are: −66 ± 10 Gt yr^{-1} (Alaska); −63 ± 8.2 Gt yr^{-1} (Arctic Canada); −9 ± 1.8 Gt yr^{-1} (Iceland); −14 ± 3.2 Gt yr^{-1} (Arctic Russia); and −12 ± 0.6 Gt yr^{-1} (Svalbard), with estimated uncertainties (at 2 std. dev.) including corrections for glacial isostatic adjustment and terrestrial hydrology. The Arctic-wide estimate for mass loss from glaciers and ice caps outside of Greenland is equal to a global sea level rise contribution of approximately 0.4 mm yr^{-1}. By comparison, Greenland currently contributes about 0.7 mm yr^{-1} (section 5e). If normalized by area, glaciers and ice caps outside Greenland are currently producing more melt per area than Greenland itself. For the Arctic as a whole (glaciers and ice caps plus the Greenland ice sheet), the current rate of contribution to global sea level rise is 1.1 mm yr^{-1}.

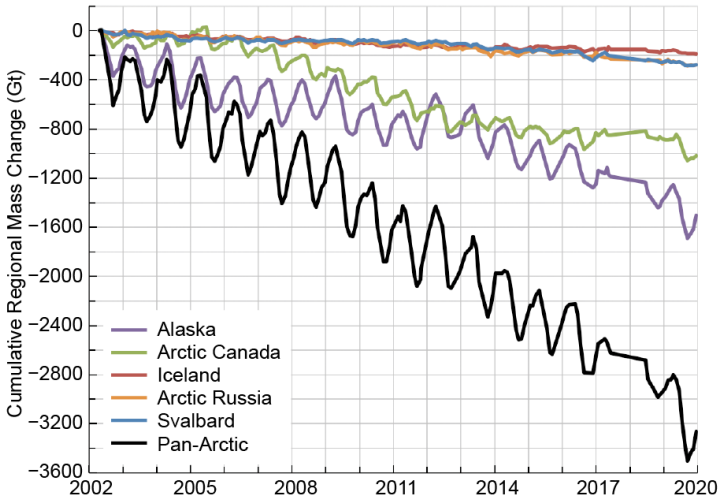

Fig. 5.19. Cumulative changes in regional total stored water for 2002–19 (Gt), derived using GRACE and GRACE-FO satellite gravimetry. A measurement gap exists between the GRACE and GRACE-FO missions from Jul 2017 to May 2018 through which linear interpolation is applied.

g. Terrestrial snow cover—L. Mudryk, R. Brown, C. Derksen, K. Luojus, and B. Decharme

Snow covers the Arctic land surface (areas north of 60°N) for up to nine months each year, influencing the surface energy budget, ground thermal regime, and freshwater budget of the Arctic (Brown et al. 2017). Snow also impacts terrestrial and aquatic ecosystems through interactions with vegetation, influences on biogeochemical cycles, and effects on migration and access to forage for wildlife (Callaghan et al. 2011). Pan-Arctic monitoring of snow cover extent, duration, depth, and water equivalent provides a suite of indicators broadly relevant across physical and ecological systems. All of these indicators exhibit negative trends over long time periods (e.g., three decades or more), albeit with varying levels of interannual variability consistent with a strong response to increasing temperatures (Mudryk et al. 2020).

Figure 5.20 shows May and June snow cover extent (SCE) anomalies (difference from 1981–2010 average) for the North American and Eurasian sectors of the Arctic. After two years of above- or near-average anomalies, spring 2019 saw a return in both sectors to the below-average SCE anomalies that were predominant over the 2005–16 time period. In particular, North American Arctic SCE anomalies were the fifth lowest in May and third lowest in June, in the 53-year record.

Snow cover onset (Fig. 5.21a) was earlier than normal over the eastern Canadian Arctic and later than normal over the Eurasian Arctic and Alaska, relative to the 1998–2017 average. These deviations from the average correspond to a pattern of warm surface temperature anomalies over Eurasia and cold anomalies over eastern Canada during September and October. Snow-off dates (Fig. 5.21b) were near normal over most of the Eurasian Arctic. Over North America, earlier-than-usual melt occurred in March across northwestern Canada and Alaska and in May and June over northeastern Canada

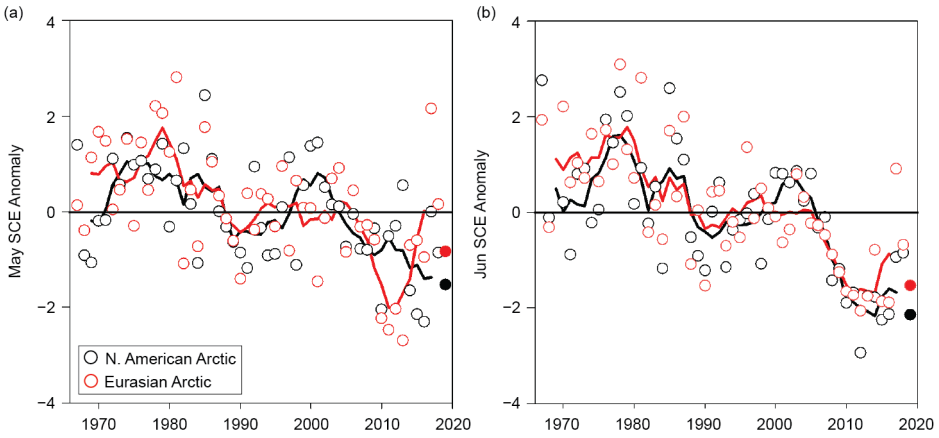

Fig. 5.20. Monthly snow cover extent (SCE) for Arctic land areas (>60°N) for (a) May and (b) Jun from 1967 to 2019, a 53-year record. Anomalies are relative to the 1981–2010 average and standardized (each observation differenced from the mean and divided by the std. dev. and thus unitless). Solid black and red lines depict 5-year running means for North America and Eurasia, respectively. Filled circles are used to highlight 2019 anomalies. (Source: NOAA snow chart Climate Data Record [Estilow et al. 2015].)

(Baffin Island and northern Quebec). These patterns are linked to warm air advection from over the North Pacific and North Atlantic, respectively (section 5b).

Snow depths over the 2019 spring season were near normal over Eurasia, relative to the 1999–2017 average. Over North America, unusually early and rapid snowmelt, driven by above-average temperatures in March over northwestern Canada and Alaska, resulted in below-average snow depth starting in March (Fig. 5.21c) and continuing through June (Fig. 5.21d), consistent with the shorter-than-average spring snow cover duration (SCD) observed in the region (Fig. 5.21b). Lower-than-normal June snow depth was also observed across Baffin Island, northern Quebec, and eastern Siberia (Fig. 5.21d).

Figure 5.22 shows a time series of April snow water equivalent (SWE) anomalies. The SWE provides a measure of how much water is stored in solid form by the snowpack. April 2019 SWE estimates indicate near-normal snow accumulation over the Eurasian Arctic relative to the 1981–2010 average. Lower-than-normal SWE is observed across the North American Arctic, consistent with negative snow depth anomalies that emerged in March (Fig. 5.21c). Note that snow conditions over the North American Arctic (north of 60°N) were in contrast to the North American midlatitude regions, which experienced an unusually deep March snowpack (Fig. 5.21c) and associated longer SCD (Fig. 5.21b).

In summary, snow accumulation during the 2018/19 winter was close to normal over the Eurasian Arctic. Over the North American Arctic, earlier-than-normal snow melt in northwestern Canada and Alaska resulted in below-average April SWE and below-average snow depth from March through June. Earlier-than-normal snow melt also occurred over Baffin Island during May

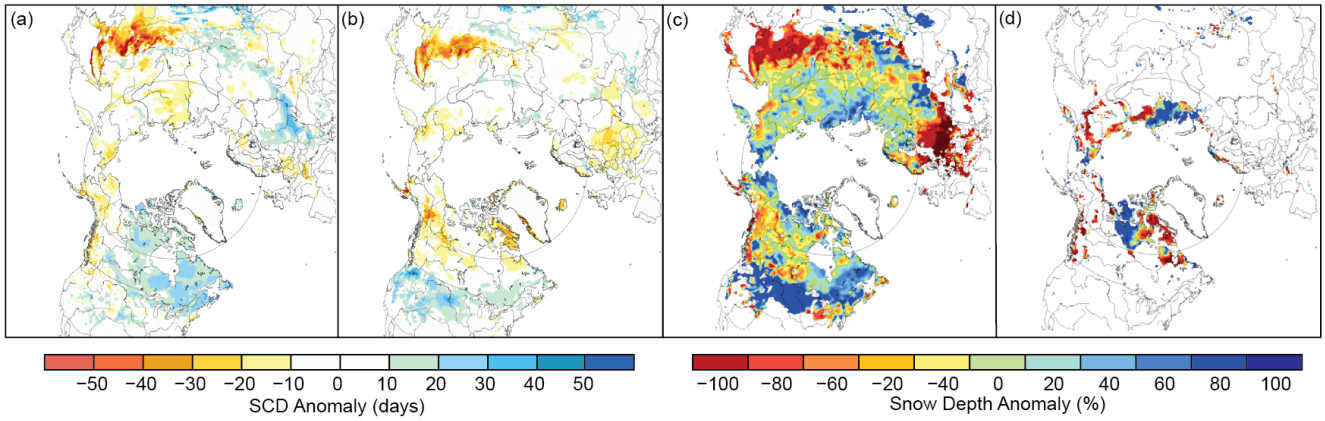

Fig. 5.21. Snow cover duration (SCD) anomaly (days, difference from 1998–2017 mean; red = shorter SCD than average; blue = longer SCD than average) for the 2018/19 snow year's (a) snow onset period (Aug–Jan) and (b) snow melt period (Feb–Jul); and snow depth anomaly (%, difference from the 1999–2017 average) for (c) Mar and (d) Jun 2019. Gray circles mark the latitude 60°N. (Source: [a,b] NOAA IMS data record [Helfrich et al. 2007; U.S. National Ice Center 2008] and [c,d] CMC snow depth analysis [Brasnett 1999].)

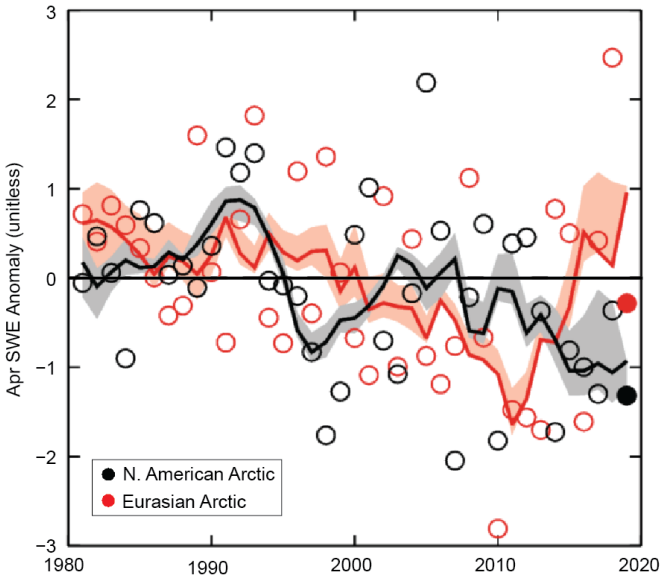

Fig. 5.22. Mean Apr snow water equivalent (SWE) anomalies for Arctic land areas calculated for North American (black) and Eurasian (red) sectors. Anomalies are relative to the average for 1981–2010 and standardized (each observation differenced from the mean and divided by the std. dev. and thus unitless). Filled circles are used to highlight 2019 anomalies. Solid black and red lines depict 5-year running means for North America and Eurasia, respectively. The spread among the running means for individual datasets is shown in shading. (Source: Suite of four independent analyses: [1] modern atmospheric reanalysis [MERRA-2; Reichle et al. 2017]; [2] reconstructed snow accumulation driven by ERA-interim meteorology with the temperature index model described by Brown et al. [2003]; [3] the physical snowpack model Crocus [Brun et al. 2013]; and [4] the European Space Agency GlobSnow product derived through a combination of satellite passive microwave data and climate station observations [Takala et al. 2011]. Note that Crocus data was unavailable for 2019 so SWE estimates for this year are calculated from only three sources.)

and June. These anomalies over the western and eastern sectors of the North American Arctic combined to cause the fifth- and third-lowest SCE in May and June, respectively, since 1967.

h. Terrestrial permafrost—V. E. Romanovsky, S. L. Smith, K. Isaksen, K. E. Nyland, A. L. Kholodov, N. I. Shiklomanov, D. A. Streletskiy, L. M. Farquharson, D. S. Drozdov, G. V. Malkova, and H. H. Christiansen

Permafrost refers to Earth materials (e.g., bedrock, mineral soil, organic matter) that remain at or below 0°C for two years or longer. Overlying the permafrost is the active layer, which thaws and refreezes annually. Permafrost underlies extensive regions of the high-latitude landscape and can be found within 24% of the landmass in the Northern Hemisphere (NH; Brown et al. 1997). The presence of permafrost, especially where it contains large volumes of ground ice, can play a critical role in the stability of Arctic landscapes. Permafrost warming, active layer thickening, and ground ice melt cause changes in surface topography, hydrology, and landscape stability, posing a major threat to Arctic infrastructure, such as buildings, roads, pipelines, and airports, as well as ecosystem integrity (Romanovsky et al. 2017; Bjella 2019). Changes in permafrost-laden regions also affect the rate of release of CO_2 and CH_4 to the atmosphere, with the potential to accelerate global climate warming (see Sidebar 5.2).

Permafrost conditions respond to shifts in the surface energy balance through a combination of interrelated changes in ground temperature and active layer thickness (ALT). Close to the surface, ground temperatures fluctuate seasonally, while below the depth of seasonal temperature variation, ground temperature reflects longer-term changes in climate. Monitoring sites across the Arctic have been recording ground temperature in the upper 30 m for up to half a century (Fig. 5.23), providing critical data on changes in permafrost stability. Observed changes in the thickness of the active layer relate to shorter-term fluctuations in climate and are especially sensitive to changes in summer air temperature and precipitation.

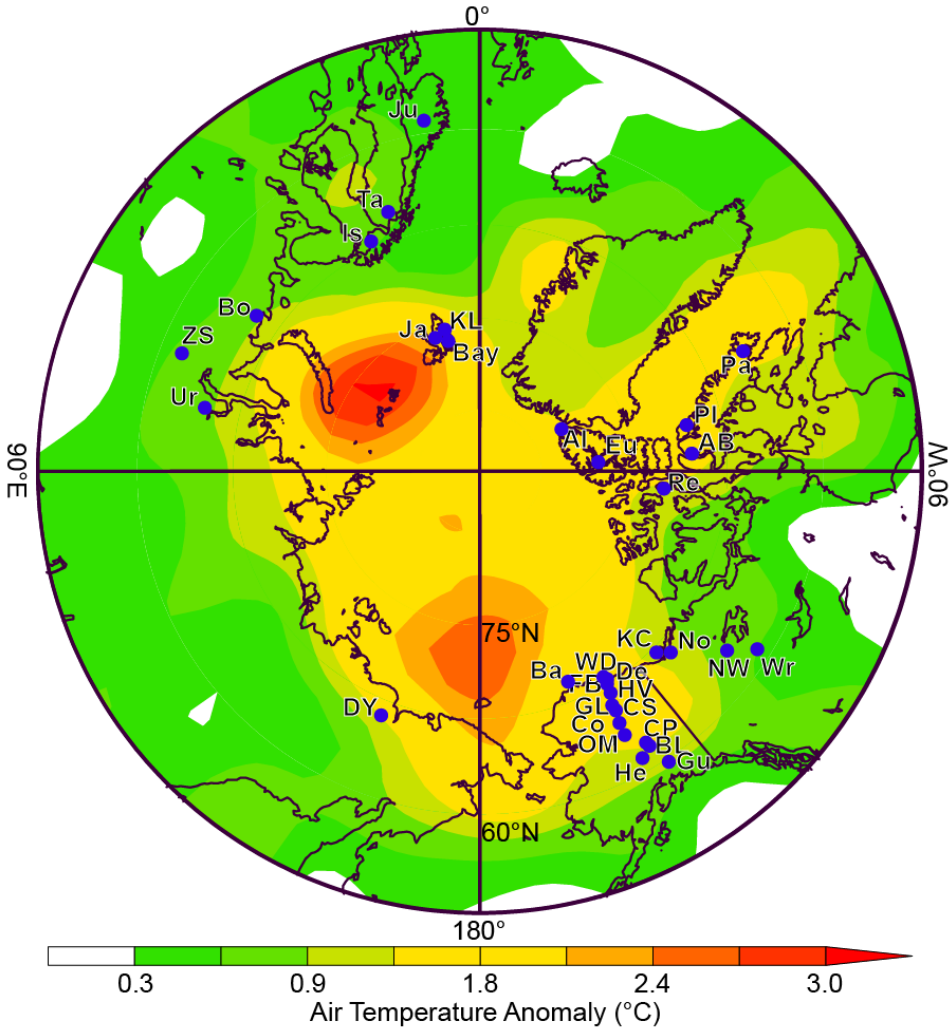

Fig. 5.23. Location of the permafrost temperature-monitoring sites, for which data are shown in Fig. 5.24, superimposed on average SAT anomalies during 2000–19 (with respect to the 1981–2010 mean) from the NCEP-reanalysis (Kalnay et al. 1996). Reanalysis data provided by the NOAA/ESRL Physical Sciences Division, Boulder, CO (www.esrl.noaa.gov/psd/). Sites shown in Fig. 5.24 are: a) Barrow (Ba), West Dock (WD), KC-07 (KC), Duvany Yar (DY), Deadhorse (De), Franklin Bluffs (FB), Galbraith Lake (GL), Happy Valley (HV), Norris Ck (No); b) College Peat (CP), Old Man (OM), Chandalar Shelf (CS), Birch Lake (BL), Coldfoot (Co), Norman Wells (NW), Wrigley 2 (Wr), Healy (He), Gulakana (Gu), Wrigley 1 (Wr); c) Eureka EUK4 (Eu), Alert BH2 (Al), Alert BH5 (Al), Resolute (Re), Alert BH1 (Al), Arctic Bay (AB), Pond Inlet (Pl), Pangnirtung (Pa); d) Janssonhaugen (Ja), Bayelva (Bay), Kapp Linne 1 (KL), Urengoy #15-10 (Ur), Juvvasshøe (Ju), Tarfalaryggen (Ta), Polar Ural (ZS), Bolvansky #59 (Bo), Bolvansky #65 (Bo), Urengoy #15-06 (Ur), Bolvansky #56 (Bo), Iskoras Is-B-2 (Is). Information about these sites is available at: http://gtnpdatabase.org/, http://permafrost.gi.alaska.edu/sites_map, https://www2.gwu.edu/~calm/data/data-links.html.

1) Permafrost temperatures

Recent long-term trends in permafrost temperatures are driven mostly by long-term air temperature changes (Romanovsky et al. 2017). In general, the increase in permafrost temperatures observed since the 1980s is more significant in the relatively colder permafrost at higher latitudes, where the largest increase in air temperature is observed (Fig. 5.23). Permafrost temperature trends also show local variability, due to other important influences such as snow depth, density, and timing (snow-on/snow-off date and duration; section 5g); vegetation characteristics; and soil moisture. Observed changes in mean annual permafrost temperatures through 2019 are presented for sites throughout the Arctic in Fig. 5.24. Table 5.1 summarizes the rate of change for each region.

In 2019, record high permafrost temperatures were observed at a majority of the observation sites (Table 5.1). For example, in northern Alaska, temperatures in 2019 were 0.1°–0.2°C higher than in 2018 and in the Alaskan interior, the 2019 temperature at one site (Old Man) was 0.26°C higher

than in 2018 (Fig. 5.24b). At sites on Svalbard, a significant temperature increase in recent years was detected down to 80-m depth (not shown), reflecting a multi-decadal permafrost warming, with 2019 clearly the warmest year in the observational record.

Also widely observed are recent increases in the rate of permafrost warming (Fig. 5.24, Table 5.1). For example, in the Canadian High Arctic, warming rates in the twenty-first century are almost twice those for the entire 40-year record. It is worth noting that throughout the Arctic, the response of permafrost with temperatures close to 0°C (i.e., warm permafrost sites) is slower than in permafrost with lower temperatures due to latent heat effects related to melting ground ice. For instance, at cold continuous permafrost sites in the Beaufort-Chukchi region, records of more than four decades in northern Alaska indicate that permafrost temperatures have increased by 0.3°–0.8°C decade^{-1} (Fig. 5.24a). Shorter records of about a decade for northwest Canada and northeastern Siberia show cold permafrost temperatures have increased by 0.4°–0.8°C decade^{-1}, similar to the twenty-first-century rate for northern Alaska. On Svalbard, at the Janssonhaugen site (Fig. 5.24d), cold permafrost has warmed by 0.8°C decade^{-1} since 1998. In contrast, at sites farther south in the warm discontinuous permafrost of interior Alaska and the central Mackenzie Valley, permafrost over the last three to four decades has warmed at a lower rate, generally less than 0.3°C decade^{-1} (Fig. 5.24b). Lower rates of warming are also observed at sites in the warm discontinuous permafrost regions of Scandinavia (e.g., Iskoras) and Russia (e.g., Bovansky #56; Fig. 5.24d).

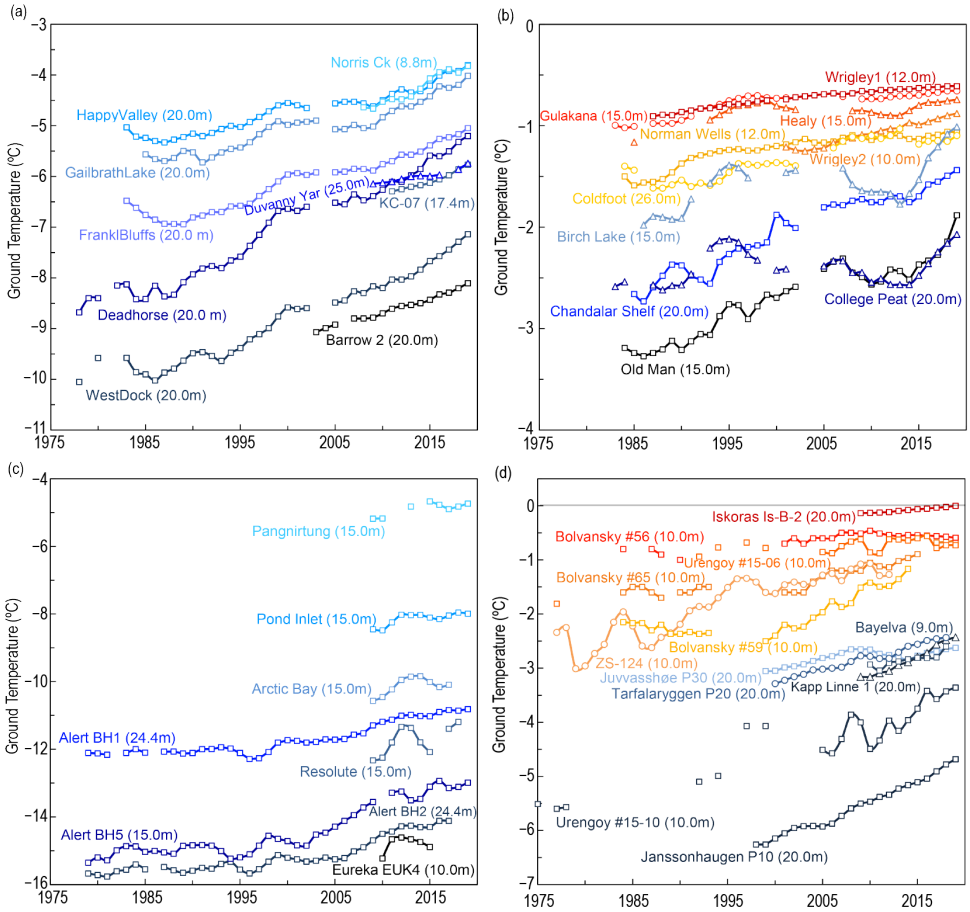

Fig. 5.24. Time series of mean annual ground temperature (°C) at depths of 9–26 m below the surface at selected measurement sites that fall roughly into priority regions of the Adaptation Actions for a Changing Arctic Project (AMAP 2015): (a) cold continuous permafrost of NW North America and NE East Siberia (Beaufort–Chukchi region); (b) discontinuous permafrost in Alaska and northwestern Canada; (c) cold continuous permafrost of eastern and High Arctic Canada (Baffin Davis Strait); (d) continuous to discontinuous permafrost in Scandinavia, Svalbard, and Russia/Siberia (Barents region). Temperatures are measured at or near the depth of zero annual amplitude where the seasonal variations of ground temperature are less than 0.1°C. The locations of each borehole are shown in Fig. 5.23. Data are updated from Christiansen et al. 2010; Romanovksy et al. 2017; Smith et al. 2019, 2018; Ednie and Smith 2015; Boike et al. 2017.

Table 5.1. Change in mean annual ground temperature (°C decade^{-1}) for permafrost monitoring sites shown in Fig. 5.24. For sites where measurements began prior to 2000, the rate of change for the entire available record is provided as well as the rate for the period after 2000. The periods of records are shown in parenthesis below the rates of change. The names of the stations with record high temperatures in 2018/19 are shown in red.

Subregion	Sites	Entire Record	Since 2000
Beaufort-Chukchi Region			
North of East Siberia	Duvany Yar (DY)	NA	+0.37 (2009–19)
Alaskan Arctic plain	West Dock (WD), Deadhorse (De), Franklin Bluffs (FB), Barrow (Ba)	+0.39 to +0.83 (1978–2019)	+0.46 to +0.72 (2000–19)
Northern foothills of the Brooks Range, Alaska	Happy Valley (HV), Galbraith Lake (GL)	+0.33 to +0.44 (1983–2019)	+0.37 to +0.48 (2000–19)
Northern Mackenzie Valley	Norris Ck (No), KC-07(KC)	NA	+0.6 to +0.8 (2008–19)
Discontinuous Permafrost Alaska and NW Canada			
Southern foothills of the Brooks Range, Alaska	Coldfoot (Co), Chandalar Shelf (CS), Old Man (OM)	+0.08 to +0.36 (1983–2019)	+0.14 to +0.41 (2000–19)
Interior Alaska	College Peat (CP), Birch Lake (BL), Gulkana (Gu), Healy (He)	+0.09 to +0.28 (1983–2019)	+0.04 to +0.27 (2000–19)
Central Mackenzie Valley	Norman Wells (NW), Wrigley (Wr)	Up to +0.1 (1984–2019)	<+0.1 to +0.2 (2000–19)
Baffin Davis Strait Region			
Baffin Island	Pangnirtung (Pa), Pond Inlet (PI)	NA	+0.4 (2009–19)
High Canadian Arctic	Resolute (Re)	NA	+0.7 (2009–18)
High Canadian Arctic	Alert (Al) @ 15m @24m	+0.6 +0.4 (1979–2019)	+1.1 +0.6 (2000–19)
Barents Region			
North of West Siberia	Urengoy 15-06 and 15-08 (Ur)	+0.31 to +0.47 (1974–2019)	+0.1 to +0.19 (2000–19)
Russian European North	Bolvansky 56, and 65 (Bo)	+0.18 to +0.46 (1984–2019)	+0.1 to +0.83 (2000–19)
Svalbard	Janssonhaugen (Ja), Bayelva (Bay), Kapp Linne 1 (KL)	+0.8 (1998–2019)	+0.6 to +0.8 (2000–19)
Northern Scandinavia	Tarfalarggen (Ta), Iskoras Is-B-2 (Is)	NA	+0.1 to +0.5 (2000–19)
Southern Norway	Juvvasshøe (Ju)	+0.2 (1999–2019)	+0.2 (2000–19)

2) Active layer thickness

In 2019, standardized, mechanical probing of ALT was conducted at 64 Circumpolar Active Layer Monitoring (CALM) program sites in Alaska, Greenland, Svalbard, and Russia (Fig. 5.25). Sites consist of a spatial grid varying from 0.01 km^2 (1 ha) to 1 km^2 in size in landscapes representative of the region (Shiklomanov et al. 2012). Additional active-layer observations are available for 25 sites in the Mackenzie Valley, northwestern Canada, where ALT is obtained from thaw tubes (Duchesne et al. 2015). The thaw tube ALT record is complete through 2018 and some of the thaw tube data are in the CALM data archive.

In all regions, as described in Fig. 5.25, the average ALT in 2019 was above the mean value for the 10-year reference period 2003–12. All regions have also experienced an overall increase in ALT over the period of record. However, there is significant variability in the magnitude of the deviation above the mean and the rate of increase. For instance, for the North Slope of Alaska, the average ALT in 2019 was 0.04 m above the 2003–12 mean. At sites in interior Alaska, which have experienced a more pronounced ALT increase, the average ALT was 0.30 m above the mean and set a new record of 0.84 m for the 23-year record. A new mean ALT maximum was also reached in southern Greenland, which was at least 0.07 m higher than the 2003–12 mean. At sites in Svalbard, where the summer of 2019 was particularly warm, ALT values were similar to the maximum recorded in 2016.

As a result of long-term permafrost warming and relatively mild and snowy winters in 2017/18 and 2018/19, the active layer did not freeze completely down to the underlying permafrost table by the end of these winters at 26 sites in interior Alaska and the Seward Peninsula. This marks the first time in the observational record that the active layer did not freeze completely in this region. Similarly, the summer thawed layer has not been refreezing completely during the last several winters at more than 10 study sites in the Russian European North and western Siberian Arctic.

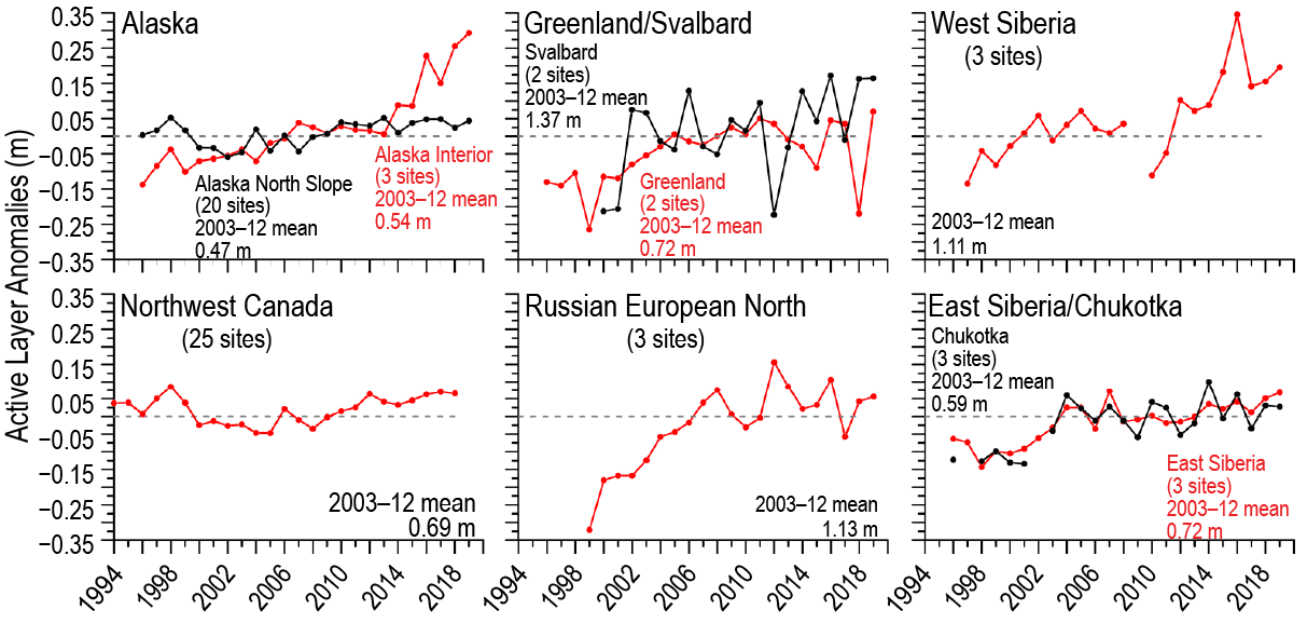

Fig. 5.25. Long-term change in the ALT in six different Arctic regions as observed by the CALM program at the end of the thawing season. The data are presented as annual anomalies (m) relative to the mean value for the 10-year reference period (2003–12). Positive and negative anomaly values indicate the active layer is thicker or thinner than these 10-year means, respectively. Only sites with at least 20 years of continuous thaw depth observations are included in this analysis. The number of sites used for each region varies and is shown in the figure. Site-specific data are available at www.gwu.edu/~calm.

SIDEBAR 5.2: **Permafrost carbon**—E.A.G. SCHUUR

Permafrost carbon is the remnants of plants, animals, and microbes that have lived and died in tundra and boreal ecosystems, accumulating over hundreds to thousands of years in frozen soils (Schuur et al. 2008). The northern permafrost region holds almost twice as much carbon as is currently in the atmosphere, representing a climate-sensitive organic carbon reservoir that is susceptible to release with warming air and ground temperatures (Schuur et al. 2015). As permafrost warms and thaws, additional net releases of CO_2 and CH_4 to the atmosphere as a result of faster microbial decomposition of this permafrost carbon have the potential to accelerate climate warming. This summary focuses specifically on recent changes in the exchange of CO_2 between tundra and boreal ecosystems and the atmosphere. While the change in net releases of CH_4 is also critical to understand, it is beyond the scope here.

The best mean estimate of the amount of organic carbon stored in the northern circumpolar permafrost region is 1460–1600 petagrams (Pg; 1 Pg = 1 billion metric tons; Schuur et al. 2015; Hugelius et al. 2014). Of this inventory, 65%–70% (1035 ± 150 Pg) of the carbon is within the surface layer (0–3 m depth; Fig. SB5.3). Soils in the top 3 m of the rest of Earth's biomes (excluding Arctic and boreal biomes) contain 2050 Pg of organic carbon (Jobbagy and Jackson 2000). Thus, the soil carbon from the northern permafrost region adds another 50% to this 3-m inventory, even though it occupies only 15% of the total global soil area (Schuur et al. 2015).

A significant amount of permafrost carbon (25%–30%) is also stored deeper (>3 m depth) due to unique processes that bury carbon in permafrost region soils. In particular, the Yedoma region of Siberia and Alaska remained ice-free during the last ice age and accumulated silt (loess) soils, which buried large quantities of organic matter deep into the permafrost (Strauss et al. 2013). Recent work has reconciled several estimates for the Yedoma region, placing 327–466 Pg C in these deep loess deposits, which can be tens of meters thick (Anthony et al. 2014; Strauss et al. 2017; Schuur et al. 2018).

Northern tundra and boreal ecosystems have historically gained carbon (carbon sink). Carbon is stored in plant biomass and new soil organic matter during the short summer growing season, when plant photosynthesis and growth is greater than carbon respired by plants and soil back to the atmosphere. In any given year, individual ecosystems can have gains or losses in net carbon due to changes in the physical and biological environment, and also depending on the successional stage of the ecosystem. However, what matters to future climate is the aggregate response across the permafrost region over years to decades.

Recent measurements of atmospheric greenhouse gas concentrations over Alaska by NASA aircraft have estimated the net regional impact on the atmosphere by Arctic tundra and boreal forest ecosystems (Commane et al. 2017). This NASA campaign, conducted during different parts of the year from 2012 to 2014, provided important insight into the aggregate influence of the carbon exchange for the Alaska permafrost region, across tundra, boreal forests, and wetland/lake/freshwater ecosystems as a whole. During this three-year period, the tundra region of Alaska was found to be a consistent net CO_2 source to the atmosphere, whereas the boreal forest region was either neutral or a net CO_2 sink. The boreal forest region exhibited larger interannual variability due both to changes in the balance of photosynthesis and respiration and to the amount of combustion emissions by wildfire.

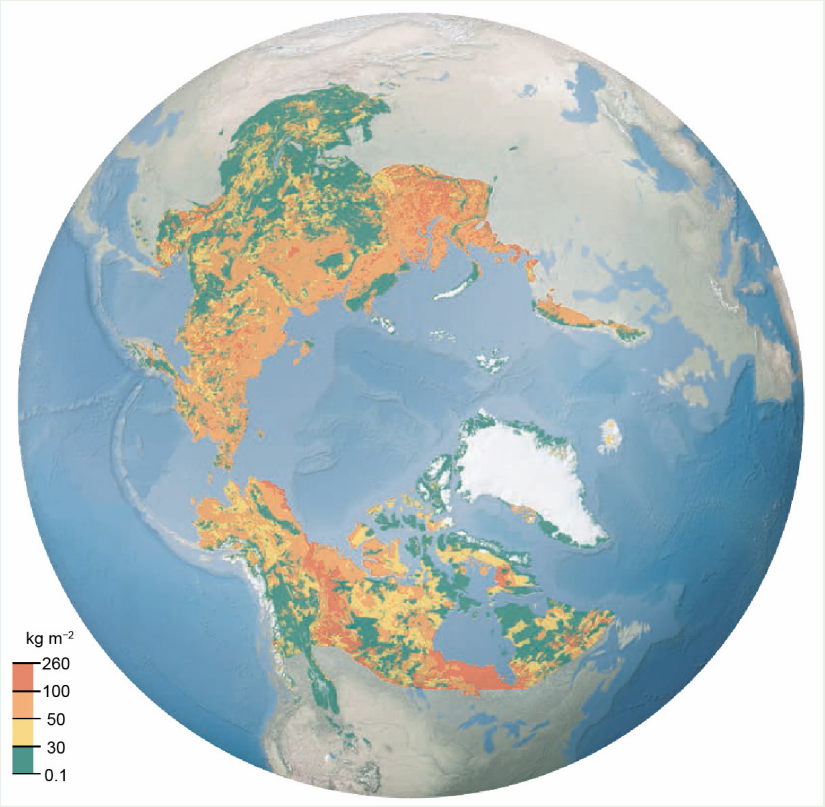

Fig. SB5.3. Soil organic carbon pools (kg m^{-2}; 0–3 m depth) for the northern circumpolar permafrost region. (Modified from *Scientific American*, Nov 2016.)

The Alaska study region as a whole was estimated to be a net carbon source of 0.025 ± 0.014 Pg C per year, averaged over the land area of both tundra and boreal forest regions for the three-year study period. If this Alaskan region (1.6×10^6 km^2) was representative of the entire northern circumpolar permafrost region soil area (17.8×10^6 km^2), this amount would be equivalent to a circumpolar net source of 0.3 Pg C per year. For comparison, recent estimates of annual CO_2 emissions from land use change (largely tropical deforestation) are 1.5 ± 0.7 Gt C (Le Quere et al. 2018). Historically (over hundreds to thousands of years), the Arctic region was accumulating carbon in soils and vegetation and thus was acting as a net sink of atmospheric CO_2. Assuming this three-year snapshot provided by NASA aircraft monitoring is indicative of the Arctic's current physical and biological environment, a significant and major threshold has been crossed in the high latitude region whereas the aggregate effect of terrestrial ecosystems is now contributing to, rather than slowing, climate change.

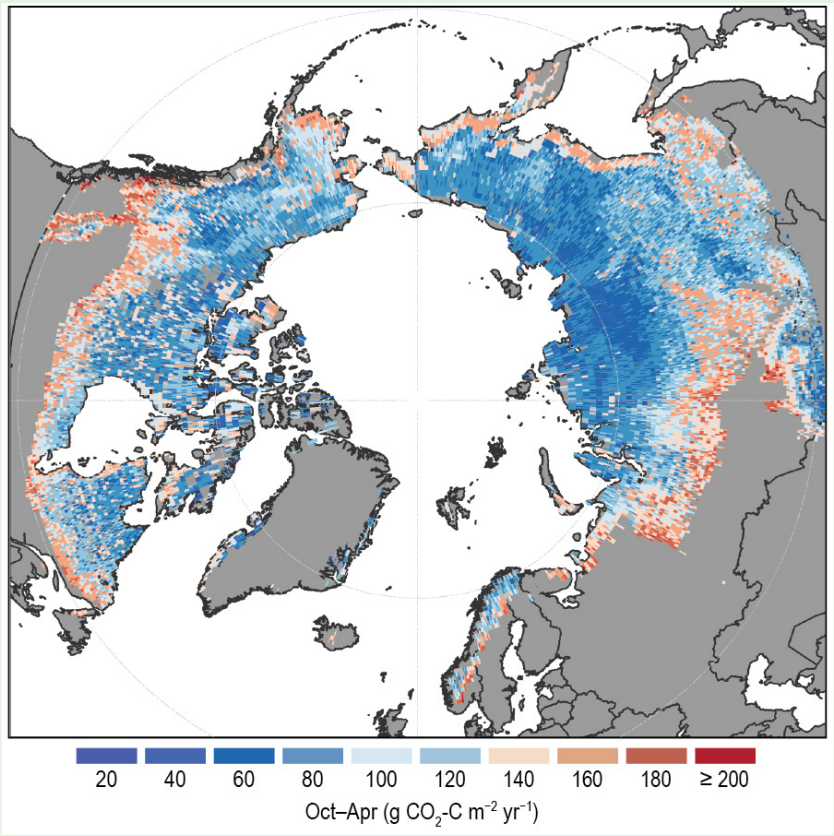

Fig. SB5.4. Non-summer season CO_2 flux rates for the permafrost region, synthesized from individual study sites measured between 2003 and 2017 and extrapolated using environmental variables. (Figure from Natali et al. 2019.)

Aircraft measurements of atmospheric greenhouse gas concentrations help to describe the combined regional impact of changing permafrost region ecosystems. However, the long cold Arctic winter (or non-summer) season limits observations from the air, just as it has limited ground-based observations in the past due to the difficult operating conditions. The summer growing season is typically a time when net carbon is stored within growing ecosystems acting as a seasonal carbon sink. However, summer carbon sequestration is partially offset by carbon losses in autumn, winter, and spring when microbes remain metabolically active and release CO_2 during a period where plants are largely dormant. While absolute levels of CO_2 flux are low during the non-summer season, the long period of more than 250 days can be enough to offset the net carbon that accumulated during summer.

A new comprehensive synthesis study of non-summer ecosystem CO_2 fluxes across the circumpolar region shows that carbon release during the Arctic winter was two to three times higher than previously estimated from ground-based measurements (Fig.SB5.4; Natali et al. 2019). This circumpolar estimate suggests that carbon release in the cold season offsets net carbon uptake during the growing season (derived from models) such that the region as a whole could already be a source of 0.6 Pg C per year to the atmosphere. It was not possible to determine whether these higher flux estimates were a result of changing environmental conditions or the aggregation of more observations during this scarcely observed non-summer period. Regardless, similar to the regional extrapolation made by aircraft, this winter flux synthesis supports the idea that the accelerating feedback from changing permafrost ecosystems to climate change may already be underway.

(Text in this essay was drawn from a longer 2019 *Arctic Report Card* essay [Schuur 2019].)

i. Tundra greenness—G. V. Frost, U. S. Bhatt, H. E. Epstein, L. T. Berner, J. W. Bjerke, B. C. Forbes, S. J. Goetz, M. J. Lara, M. J. Macander, G. K. Phoenix, M. K. Raynolds, H. Tømmervik, and D. A. Walker

One of the most widespread and conspicuous manifestations of Arctic climatic and environmental change has been an increase in the productivity and biomass of tundra vegetation, a phenomenon commonly termed "the greening of the Arctic." Trends in the productivity of tundra ecosystems, however, have not been uniform in direction or magnitude across the circumpolar Arctic, and there has been substantial inter-annual variability (Bhatt et al. 2013, 2017; National Academies of Sciences, Engineering and Medicine 2019). This variability arises from a web of interactions that link the vegetation, atmosphere, sea ice, seasonal snow cover, ground (soils, permafrost, and topography), disturbance processes, and herbivores of the Arctic system (Duncan et al. 2019; Piao et al. 2019; Myers-Smith et al. 2020).

Many of the changes observed in tundra ecosystems are producing a cascade of effects on Earth's subsurface, surface, and atmosphere within and beyond the far north (Post et al. 2019). For example, changes in the composition and height of tundra vegetation impact the cycling of carbon and nutrients (Blume-Werry et al. 2019; Hewitt et al. 2019; Mörsdorf et al. 2019; Salmon et al. 2019; Treharne et al. 2019), as well as energy exchanges between the atmosphere and permafrost (Wilcox et al. 2019). The latter has implications for permafrost stability, geomorphology, and surface wetness, which, coupled with changing vegetation structure, strongly alters landscape properties important to wildlife (Cray and Pollard 2018; Tape et al. 2018; Taylor et al. 2018; Ims et al. 2019; Farquharson et al. 2019; Andruko et al. 2020) and the subsistence activities of Arctic peoples (Brinkman et al. 2016; Veldhuis et al. 2018; Herman-Mercer et al. 2019). Continued monitoring of the Arctic tundra biome both from space and in situ field studies improves our understanding of these complex interactions.

Since 1982, Earth-observing satellites have provided a continuous record of global vegetation productivity using the Normalized Difference Vegetation Index (NDVI), a metric that exploits the unique spectral properties of live vegetation. NDVI is strongly correlated with the quantity of above-ground vegetation, or "greenness," of Arctic tundra (Raynolds et al. 2012). The data reported here come from the Global Inventory Modeling and Mapping Studies (GIMMS)-3g dataset (Pinzon and Tucker 2014). Two metrics based on NDVI are used: (1) MaxNDVI, the peak annual NDVI value that corresponds to the maximum above-ground biomass of vegetation reached in

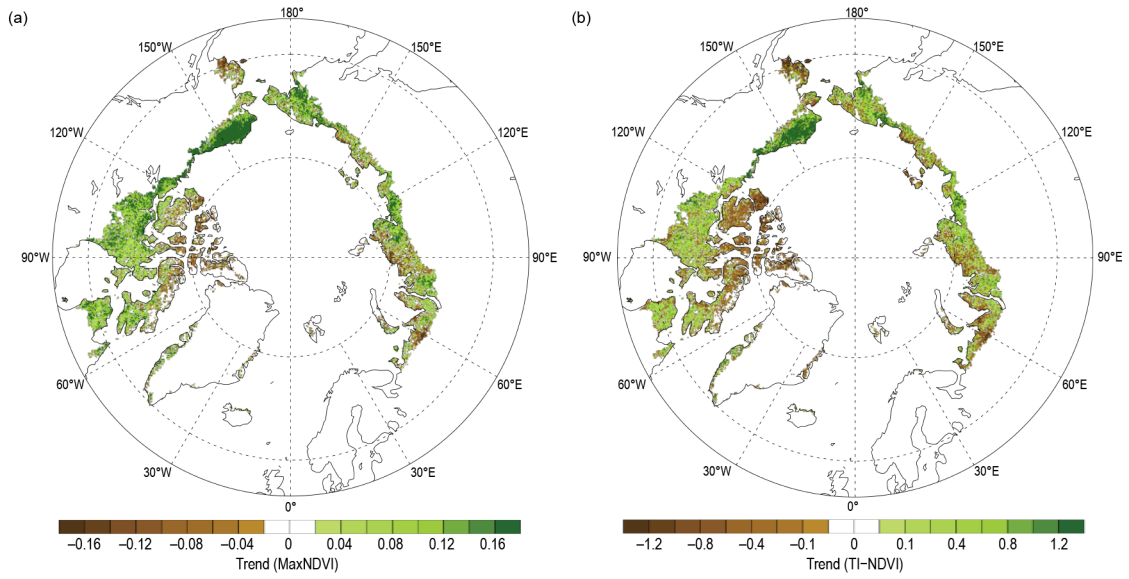

Fig. 5.26. Magnitude of the trend (calculated as the total change over a least squares, linear fit trend line) in (a) MaxNDVI and (b) TI-NDVI for 1982–2019. (Source: GIMMS-3g, a biweekly, maximum-value composited dataset of the NDVI derived from the AVHRR sensor with a spatial resolution of 1/12° [approximately 40 km; Pinzon and Tucker 2014].)

midsummer; and (2) TI-NDVI, the time-integrated NDVI that is the sum of the biweekly NDVI values for the growing season and is correlated with the total above-ground productivity of vegetation.

The GIMMS-3g dataset now provides a 38-year record (1982–2019) that indicates increasing MaxNDVI and TI-NDVI across most of the Arctic tundra biome (Figs. 5.26a,b). The strongest greening has occurred in northern Alaska, mainland Canada, and the Russian Far East. Tundra greenness appears to have declined, however, in parts of western Alaska, the Canadian Arctic Archipelago, northeastern Europe, and northwestern Siberia. In recent years, similar NDVI datasets have been compiled from other satellite sensors, such as those on the Landsat satellites, which can be used to corroborate the GIMMS-3g record. These datasets suggest that Arctic greening may be even more widespread than the GIMMS-3g record indicates, albeit with a shorter period of record. For example, a recent analysis of the Landsat record indicates widespread increases in MaxNDVI from 1985 to 2018; significant greening was evident at 37% of sampling sites distributed across the Pan-Arctic, and significant browning occurred at only 5% of sampling sites (L. Berner, personal communication, 2020).

In 2019, the mean MaxNDVI value for the circumpolar Arctic declined slightly from the previous year (Fig. 5.27a). This marks the third straight year of declining MaxNDVI across the region, following the record high value in 2016. However, trends in MaxNDVI have differed strongly by continent, especially over the last three years. In the Eurasian Arctic, the 2019 value was similar to the preceding four years, and was above the 1982–2019 mean. In the North American Arctic, however, the 2019 value was the lowest in the record since 1996 and fell below the long-term mean. In contrast to MaxNDVI, TI-NDVI increased substantially from the previous year (Fig. 5.27b) for the circumpolar Arctic, and particularly in the North American Arctic where late snowmelt and relatively cool summer temperatures contributed to record low TI-NDVI values in 2018 (Schmidt et al. 2019). The increase in TI-NDVI from the previous year in the North American Arctic was the third-largest single-year increase in the entire record. Nonetheless, the 2019 TI-NDVI value for the circumpolar region was well below the 1982–2019 mean and was the second-lowest value since 2009. It should be noted that mean NDVI values for North American tundra average lower than those for Eurasian tundra because a much larger proportion of the North American Arctic experiences a cold, dry High Arctic climate (Walker et al. 2005).

Spaceborne observations of land surface temperature—a key control of tundra productivity—provide

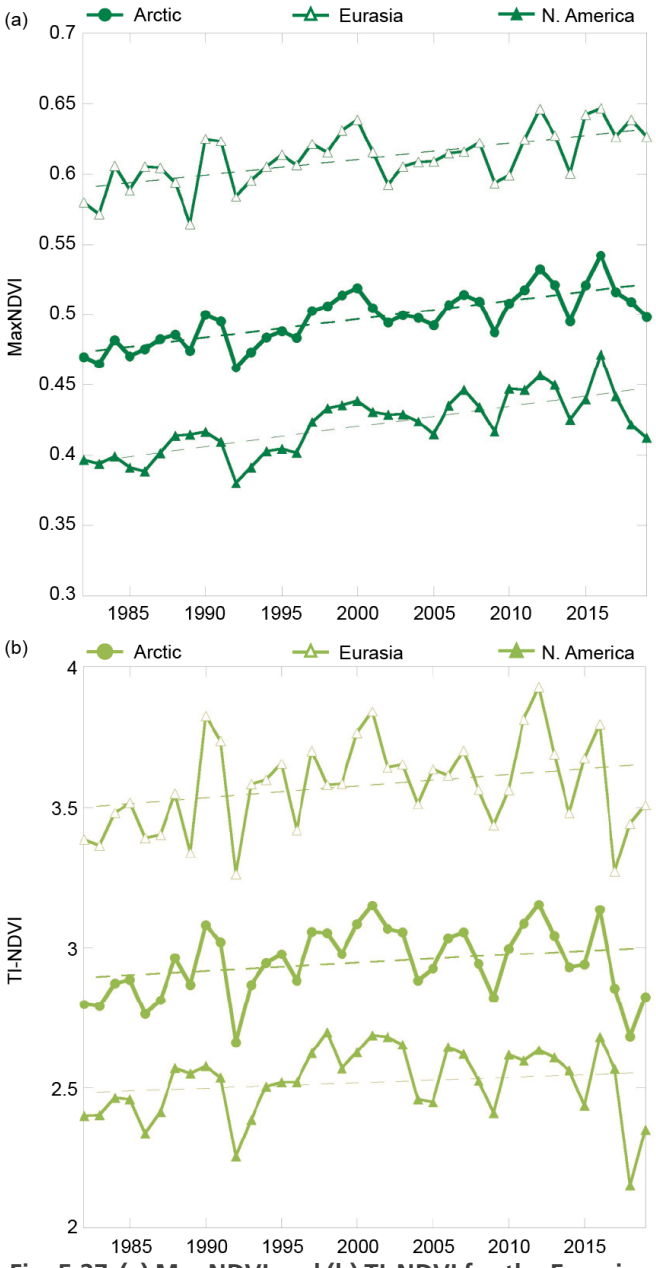

Fig. 5.27. (a) MaxNDVI and (b) TI-NDVI for the Eurasian Arctic (top), the full circumpolar Arctic (middle), and the North American Arctic (bottom) for 1982–2019. Dashed lines indicate linear trends; MaxNDVI trends are highly significant ($p < 0.001$) but TI-NDVI trends are not ($p > 0.05$). (Source: GIMMS-3g, a biweekly, maximum-value composited dataset of the NDVI derived from the AVHRR sensor with a spatial resolution of 1/12° [approximately 40 km; Pinzon and Tucker 2014].)

context for understanding spatio-temporal patterns of tundra productivity and are available from the same satellite sensors that record NDVI for the GIMMS-3g dataset. We summarize the land surface temperature observations as the Summer Warmth Index (SWI), the sum of mean monthly temperatures for all months with mean temperatures above freezing (>0°C). The 2019 growing season was the warmest in the entire record; the mean SWI for the full circumpolar region (39.0°C-months) broke the previous record set in 2016 (34.9°C-months). The tundra regions of both continents experienced record warmth (section 5b). The 2019 SWI exceeded previous highs set in North America and Eurasia in 1994 and 2016, respectively. This warmth was not, however, accompanied by strong increases in NDVI, possibly due to lag effects arising from the below-normal summer temperatures experienced in 2018. Within the 38-year record, MaxNDVI values for 2019 ranked 19th, 9th, and 26th for the circumpolar Arctic, Eurasian Arctic, and North American Arctic, respectively. TI-NDVI values ranked 31st, 26th, and 35th for the circumpolar Arctic, Eurasian Arctic, and North American Arctic respectively.

j. Ozone and UV radiation—G. Bernhard., V. Fioletov, J.-U. Grooß, I. Ialongo, B. Johnsen, K. Lakkala, G. Manney, and R. Müller

Past emissions of chlorine-containing substances, such as chlorofluorocarbons (CFCs), have substantially contributed to the chemical destruction of ozone in the atmosphere (WMO 2018). The resulting ozone loss has led to increased ultraviolet (UV) radiation with adverse effects on human health and Earth's environment (EEAP 2019). The chemical destruction of polar ozone occurs within a cold low-pressure system (i.e., cyclone) known as the polar vortex, which forms over the North Pole every year during winter and spring (WMO 2018). Hence, the period of December 2018–April 2019 is emphasized in this report. As explained in more detail below, unusual conditions during this period enabled ozone concentrations in February and early March 2019 to reach the highest values in at least the past 15 years of satellite observations. In March 2019, the minimum Arctic daily total ozone column (TOC; i.e., ozone amounts integrated from the surface to the top of the atmosphere) was the highest value since 1988, for years when a well-defined polar vortex existed in March. With some exceptions, UV index (UVI) anomalies during this period were generally within the typical range of variability.

1) Ozone

Chemical processes that drive ozone depletion in the polar stratosphere are initiated at temperatures below about 195 K (–78°C) at altitudes of approximately 15 to 25 km. These low temperatures lead to the formation of polar stratospheric clouds (PSCs), which act as a catalyst to transform inactive forms of chlorine-containing substances to active, ozone-destroying chlorine species. At the beginning of December 2018, temperatures in the lower Arctic stratosphere dropped below the threshold for PSC formation and remained below this threshold and near the mean of the observational record (1979–2017) during the first three weeks of December. On 2 January 2019, a major sudden stratospheric warming (SSW) occurred, which led to a rapid rise of polar stratospheric temperatures over the course of a few days. During this event, the polar vortex split into three "offspring" vortices. As a result, stratospheric temperatures rose above the threshold for PSCs and remained well above this threshold for the remainder of the winter. The offspring vortices recombined in early March such that the polar vortex observed on 12 March was the strongest of the winter/spring 2018/19 period (Lee and Butler 2020). However, stratospheric temperatures at this time were too high for PSC formation.

Because of the early SSW event, chemical destruction of ozone was unusually low over the winter/spring period of 2018/19, as is confirmed by satellite-based observations. Measurements by the Microwave Limb Sounder (MLS) show that chlorine activation started in mid-December, resulting in a small decline in ozone concentrations, as expressed by the ozone mixing ratio (Fig. 5.28). Chlorine deactivation began in early January 2019 and was complete by late that month—consequently no chemical

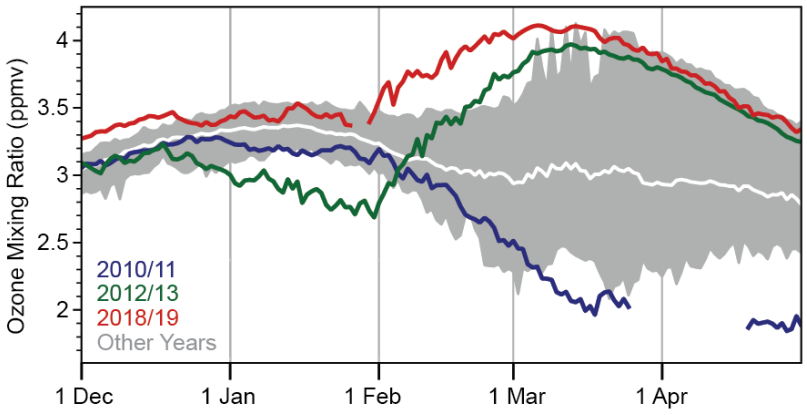

Fig. 5.28. Average ozone mixing ratios (ppmv) at an altitude of ~18 km for the area bounded by the polar vortex, as measured by *Aura* MLS. Data from 2018/19 (red), 2012/13 (green), and 2010/11 (blue) are compared with the average (solid white) and minimum/maximum range (gray shading) from 2004/05 to 2017/18, excluding 2010/11, 2012/13, and 2018/19. Gaps in the record for 2010/11 and 2018/19 are due to missing data.

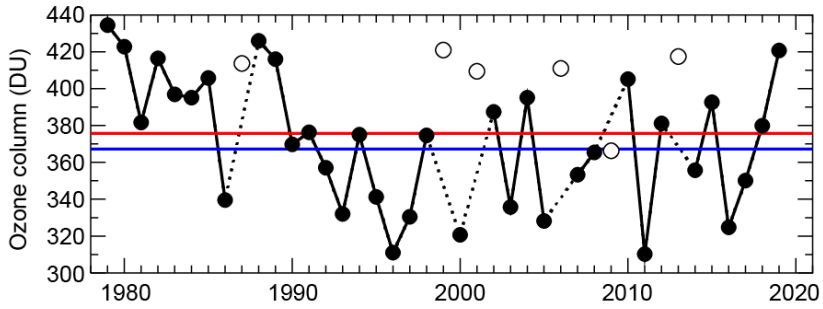

Fig. 5.29. Minimum of the daily average column ozone for Mar poleward of 63°N equivalent latitude (Butchart and Remsberg 1986). Open circles represent years in which the polar vortex was not well-defined in Mar, resulting in relatively high values due to mixing with lower latitude air masses and a lack of significant chemical ozone depletion. Red and blue lines indicate the average TOC for 1979–2018 and 2005–18, respectively. Ozone data for 1979–2016 are based on the combined total column ozone database version 3.4 produced by Bodeker Scientific (www.bodeker-scientific.com/data/total-column-ozone). Ozone data for 2017–19 are from the OMI. The graph is adapted from Müller et al. (2008) and WMO (2018), updated using ERA-Interim reanalysis data (Dee et al. 2011) for determining equivalent latitude.

ozone loss occurred after about mid-January. This sequence of conditions enabled ozone concentrations in February and early March 2019 to reach the highest values in at least the past 15 years, the period of the MLS observational record. The conditions in 2018/19 were similar to those in 2012/13 (Manney et al. 2015), although the strong SSW started a few days earlier in 2019 (Fig. 5.28). Unlike December 2018, December 2012 temperatures in the lower Arctic stratosphere were unusually cold, resulting in greater chlorine activation and much larger ozone loss in 2012/13 compared to 2018/19. The largest chemical ozone loss observed to date occurred in the winter of 2010/11 and was associated with an unusually prolonged cold period lasting through early April 2011, with temperatures in the lower stratosphere remaining low enough for PSC formation (Manney et al. 2011).

The evolution of Arctic TOC in March 2019 is compared to the satellite-derived observational record (1979–2018) in Fig. 5.29 using the minimum of the daily averages for March. March TOC is evaluated because chemically-induced Arctic ozone loss has the largest variability in this month (Fig. 5.28; WMO 2018). In March 2019, the minimum Arctic daily TOC was 421 Dobson units (DU), which was the highest value since 1988 for years when a well-defined polar vortex existed in March. The value was 12.0% (45 DU) above the average of the observational record (376 DU) and 14.6% (54 DU) above the average when MLS data are available (2005–18).

Spatial deviations of monthly average TOCs from historical (2005–18) averages (Figs. 5.30a,b) were estimated from the Ozone Monitoring Instrument (OMI; co-located with MLS on the *Aura* satellite) measurements. With the exception of an area centered over northwestern Canada, TOCs in March 2019 were above the mean over sunlit regions of the Arctic (Fig. 5.30a), consistent with the high ozone concentrations inside the lower stratospheric polar vortex during March 2019 (Fig. 5.28). These anomalies ranged between 0% over Scandinavia to 12% over Siberia. In mid-April, TOC departures exhibited a distinct geographical pattern with positive anomalies of up to 17% over Canada, the North Pole, and Siberia, and negative anomalies as large as –17% over Scandinavia and the North Sea (Fig. 5.30b).

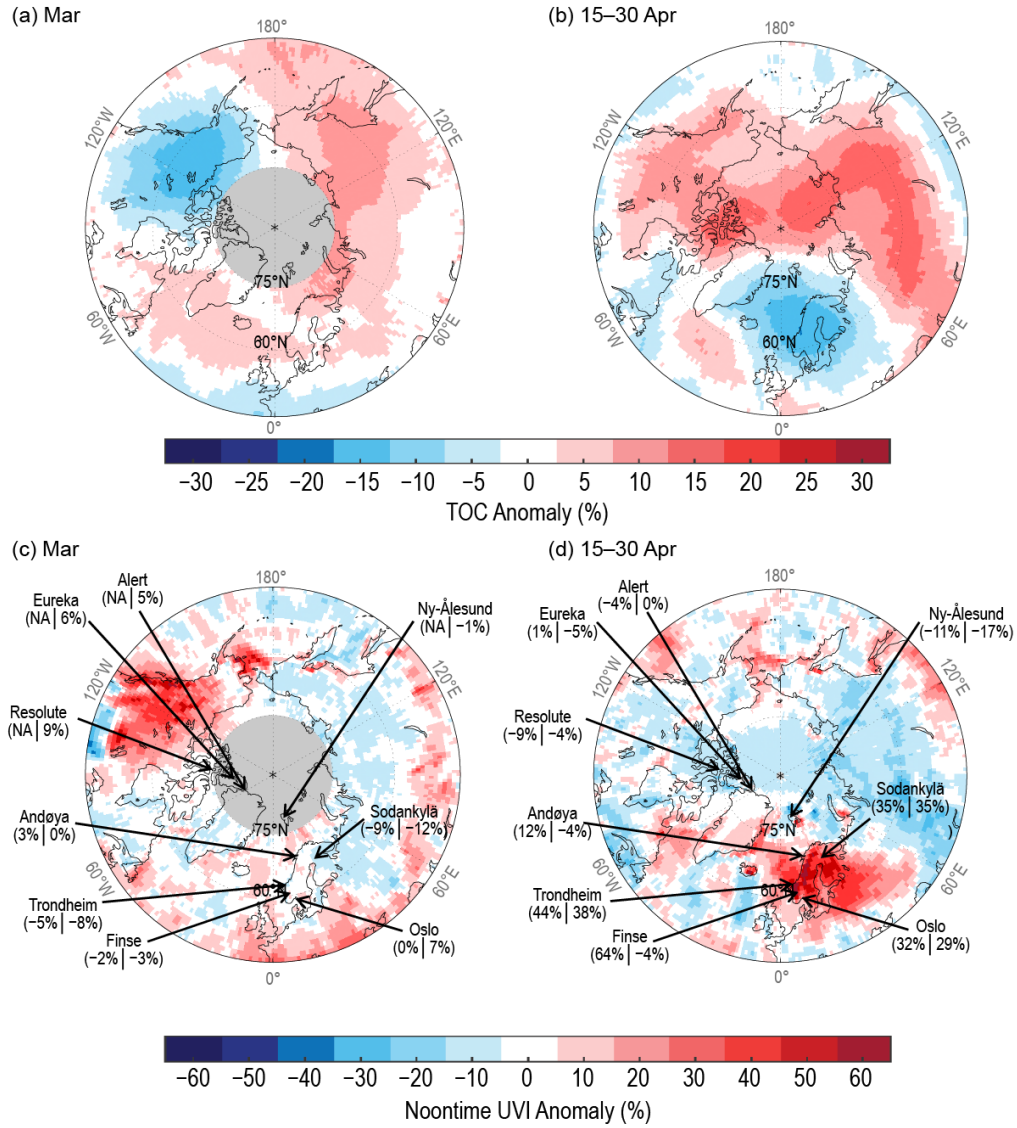

Fig. 5.30. Anomalies of TOC (%) for (a) Mar and (b) 15–30 Apr 2019. Anomalies of noontime UVI (%) for (c) Mar and (d) 15–30 Apr 2019. Anomalies are relative to 2005–18 averages. Maps are based on the OMTO3 Level 3 total ozone product (Bhartia and Wellemeyer 2002). (c) and (d) also compare UVI anomalies from OMI (first value in parenthesis) with ground-based measurements at nine locations (second value). Gray, solid circles centered at the North Pole indicate the areas where no OMI data are available due to the lack of sunlight at this time of year.

2) Ultraviolet radiation

UV radiation is quantified with the UVI, which is a measure of the capacity of UV radiation to cause erythema (sunburn) in human skin (WHO 2002). In addition to its dependence on TOC, the UVI depends on the sun angle, clouds, and surface albedo (Weatherhead et al. 2005). In the Arctic, the UVI scale ranges from 0 to about 7, with the smallest annual peak radiation levels (UVI values < 4) observed at sites closest to the North Pole. UVI values ≤ 5 indicate low-to-moderate risk of erythema (WHO 2002).

UVI anomalies are assessed using both OMI and ground-based measurements, with the former providing better spatial coverage and the latter providing greater regional accuracy (Bernhard et al. 2015). Figures 5.30c,d quantify the spatial differences in monthly average noontime UVIs from historical (2005–18) averages based on measurements by OMI and by ground-based instruments at nine research stations located in the Arctic and Scandinavia. Areas with high UVIs roughly match areas with low TOCs and vice versa, but UVI anomalies have larger spatial variability because of their added dependence on clouds. In the following discussion, we emphasize

March 2019 and 15–30 April 2019. During the latter period, unusually large UVI anomalies over the Nordic countries occurred, while ozone and UVI anomalies for other months were generally within the typical range of variability.

In March 2019, monthly average noontime UVIs calculated from OMI observations over northwestern Canada were up to 55% above the 2005–18 mean (Fig. 5.30c). This region of unusually high UVIs coincided with the area of low TOCs in Fig. 5.30a. Large UVI anomalies of up to 50% were also observed west of Alaska. UVI anomalies for the remainder of the Arctic computed from OMI and ground-based measurements were below 15%. Because of the low solar zenith angle in March, absolute anomalies did not exceed 1.9 UVI units for latitudes higher than 60°N.

During the period of 15–30 April, a persistent high-pressure system was centered over the Nordic countries, and the ensuing periods of clear skies contributed to large UVI anomalies of up to 65% (Fig. 5.30d). Anomalies calculated from OMI and ground-based data agreed to within ±8% at almost all locations. Exceptions included Andøya and Finse due to local weather (cloudiness) and ground conditions (low albedo due to unusually wet snow cover), respectively. The influence of local conditions creates inconsistencies between satellite and ground-based measurements and illustrates the limitations of estimating UV radiation from space. These inconsistencies are largest at locations that are either affected by variable conditions within the satellite instrument's field of view (cloudiness, albedo, topography) or differences between the actual surface albedo and the albedo climatology used by OMI (Tanskanen et al. 2004).

Acknowledgments

The editors thank Dr. Martin Jeffries, USACE Cold Regions Research and Engineering Laboratory, and Florence Fetterer, National Snow and Ice Data Center, for providing an initial review of the full chapter. Their careful read and thoughtful input improved each of the sections and, importantly, led to better coherency between the sections.

a. Overview

- Jackie Richter-Menge appreciates support from NOAA's Arctic Research Office.
- Matthew Druckenmiller was supported by the Study of Environmental Arctic Change (SEARCH, NSF grant PLR-1331100).

b. Surface air temperature

- Jim Overland has support from the NOAA Arctic Research Program.
- Tom Ballinger acknowledges support from the Experimental Arctic Prediction Initiative at the University of Alaska Fairbanks.

d. Sea ice

Walt Meier's contribution was supported by the NASA Snow and Ice Distributed Active Archive Center (DAAC) at NSIDC, part of the NASA Earth Science Data and Information System (ESDIS) Project.

e. Greenland ice sheet

Macro Tedesco acknowledges financial support by the National Science Foundation (PLR-1603331, PLR-1713072), NASA (NNX17AH04G, 80NSSC17K0351) and the Heising-Simons Foundation. Financial support for measurements along the K-transect has been received from the Dutch Polar Program of NWO. Data from the Programme for Monitoring of the Greenland Ice Sheet (PROMICE) and the Greenland Analogue Project (GAP) were provided by the Geological Survey of Denmark and Greenland (GEUS) at http://www.promice.dk. Computational resources for running the MAR model have been provided by the Consortium des Équipements de Calcul Intensif (CÉCI), funded by the Fonds de la Recherche Scientifique de Belgique (F.R.S.FNRS) under grant no. 2.5020.11 and the Tier-1 supercomputer (Zenobe) of the Fédération Wallonie Bruxelles infrastructure funded by the Wallonia region under grant agreement no. 1117545.

j. Ozone and UV Radiation

Germar Bernhard and coauthors acknowledge the support of Biospherical Instruments, San Diego; the Research Council of Norway through its Centers of Excellence funding scheme, project number 223268/F50; the Academy of Finland for supporting UV measurements through the FARPOCC and SAARA projects; the European Space Agency for supporting the DACES project; and the European Union for supporting e-shape. We also thank the Microwave Limb Sounder team at NASA's Jet Propulsion Laboratory for data processing and analysis support; Tove Svendby from the Norwegian Institute for Air Research and Arne Dahlback from the University of Oslo for overseeing UV measurements at Oslo, Andøya, and Ny-Ålesund; and Juha M. Karhu, Tomi Karppinen, and Markku Ahponen from the Finnish Meteorological Institute for operating the Brewer UV spectroradiometer at Sodankylä.

Sidebar 5.1. Shifting fish distributions in the Bering Sea

We'd like to thank the scientists and crews who took part in these long-term groundfish surveys in the eastern and northern Bering Sea. We also thank R. Haehn for pulling the 2019 survey data.

Sidebar 5.2 Permafrost carbon

Support provided by:

- NSF Research, Synthesis, and Knowledge Transfer in a Changing Arctic: Science Support for the Study of Environmental Arctic Change (SEARCH) Grant # 1331083. (2014-2020)
- NSF PLR Arctic System Science Research Networking Activities (RNA) Permafrost Carbon Network: Synthesizing Flux Observations for Benchmarking Model Projections of Permafrost Carbon Exchange (2019-2023).

APPENDIX: Acronym List

ALT	active layer thickness
AMJ	April, May, June
CFCs	chlorofluorocarbons
CALM	Circumpolar Active Layer Monitoring
DMI	Danish Meteorological Institute
DJF	December–February
DU	Dobson units
GrIS	Greenland ice sheet
JFM	January, February, March
JAS	July, August, September
JJA	June–August
MAM	March–May
MLS	Microwave Limb Sounder
MAR	Modèle Atmosphérique Régionale
MODIS	Moderate Resolution Imaging Spectroradiometer
NSIDC	National Snow and Ice Data Center
NDVI	Normalized Difference Vegetation Index
NAO	North Atlantic Oscillation
NH	Northern Hemisphere
OND	October, November, December
OMI	Ozone Monitoring Instrument
Pg	petagrams
PSCs	polar stratospheric clouds
PROMICE	Program for Monitoring of the Greenland Ice Sheet
SSTs	sea surface temperatures
SCD	snow cover duration
SCE	snow cover extent
SWE	snow water equivalent
SSW	sudden stratospheric warming
SWI	Summer Warmth Index
SAT	surface air temperature
TOC	total ozone column
UV	ultraviolet
UVI	UV index
WGMS	World Glacier Monitoring Service

References

Acosta Navarro, J. C., and Coauthors, 2016: Amplification of Arctic warming by past air pollution reductions in Europe. *Nat. Geosci.*, **9**, 277–281, https://doi.org/10.1038/ngeo2673.

Alabia, I. D., J. G. Molinos, S.-I. Saitoh, T. Hirawake, T. Hirata, and F. J. Mueter, 2018: Distribution shifts of marine taxa in the Pacific Arctic under contemporary climate changes. *Divers. Distrib.*, **24**, 1583–1597, https://doi.org/10.1111/ddi.12788.

Andersen, J. K., and Coauthors, 2019: Update of annual calving front lines for 47 marine terminating outlet glaciers in Greenland (1999–2018). *Geol. Surv. Den. Greenl. Bull.*, **43**, e2019430202, https://doi.org/10.34194/GEUSB-201943-02-02.

Andruko, R., R. Danby, and P. Grogan, 2020: Recent growth and expansion of birch shrubs across a low Arctic landscape in continental Canada: Are these responses more a consequence of the severely declining caribou herd than of climate warming? *Ecosystems*, https://doi.org/10.1007/s10021-019-00474-7, in press.

Anthony, K. M. W., and Coauthors, 2014: A shift of thermokarst lakes from carbon sources to sinks during the Holocene epoch. *Nature*, **511**, 452–456, https://doi.org/10.1038/nature13560.

Barton, B. I., Y. Lenn, and C. Lique, 2018: Observed Atlantification of the Barents Sea causes the Polar Front to limit the expansion of winter sea ice. *J. Phys. Oceanogr.*, **48**, 1849–1866, https://doi.org/10.1175/JPO-D-18-0003.1.

Bernhard, G., and Coauthors, 2015: Comparison of OMI UV observations with ground-based measurements at high northern latitudes. *Atmos. Chem. Phys.*, **15**, 7391–7412, https://doi.org/10.5194/acp-15-7391-2015.

Bhartia, P. K., and C. W. Wellemeyer, 2002: TOMS-V8 total O3 algorithm. OMI Algorithm Theoretical Basis Document, Vol. II, NASA Goddard Space Flight Center Tech. Doc. ATBD-OMI-02, 15–31, http://eospso.nasa.gov/sites/default/files/atbd/ATBD-OMI-02.pdf.

Bhatt, U. S., and Coauthors, 2013: Recent declines in warming and vegetation greening trends over Pan-Arctic tundra. *Remote Sens.*, **5**, 4229–4254, https://doi.org/10.3390/rs5094229.

——, and Coauthors, 2017: Changing seasonality of panarctic tundra vegetation in relationship to climatic variables. *Environ. Res. Lett.*, **12**, 055003, https://doi.org/10.1088/1748-9326/aa6b0b.

Bieniek, P. A., and J. E. Walsh, 2017: Atmospheric circulation patterns associated with monthly and daily temperature and precipitation extremes in Alaska. *Int. J. Climatol.*, **37**, 208–217, https://doi.org/10.1002/joc.4994.

Bjella, K., 2019: Warming and thawing permafrost and impacts on infrastructure [in "State of the Climate in 2018"]. *Bull. Amer. Meteor. Soc.*, **100** (9), S157–S159., https://doi.org/10.1175/2019BAMSStateoftheClimate.1.

Blume-Werry, G., A. Milbau, L. M. Teuber, M. Johansson, and E. Dorrepaal, 2019: Dwelling in the deep – Strongly increased root growth and rooting depth enhance plant interactions with thawing permafrost soil. *New Phytol.*, **223**, 1328–1339, https://doi.org/10.1111/nph.15903.

Boike, J., and Coauthors, 2018: A 20-year record (1998–2017) of permafrost, active layer, and meteorological conditions at a High Arctic permafrost research site (Bayelva, Spitsbergen). *Earth Syst. Sci. Data*, **10**, 355–390, https://doi.org/10.5194/essd-10-355-2018.

Box, J. E., D. van As, and K. Steffen, 2017: Greenland, Canadian and Icelandic land ice albedo grids (2000–2016). *Geol. Surv. Den. Greenl. Bull.*, **38**, 53–56, https://doi.org/10.34194/geusb.v38.4414.

——, and Coauthors, 2019: Key indicators of Arctic climate change: 1971–2017. *Environ. Res. Lett.*, **14**, 045010, https://doi.org/10.1088/1748-9326/aafc1b.

Brasnett, B., 1999: A global analysis of snow depth for numerical weather prediction. *J. Appl. Meteor.*, **38**, 726–740, https://doi.org/10.1175/1520-0450(1999)038<0726:AGAOSD>2.0.CO;2.

Brinkman, T. J., W. D. Hansen, F. S. Chapin, G. Kofinas, S. BurnSilver, and T. S. Rupp, 2016: Arctic communities perceive climate impacts on access as a critical challenge to availability of subsistence resources. *Climatic Change*, **139**, 413–427, https://doi.org/10.1007/s10584-016-1819-6.

Brown, J., O. J. Ferrians Jr., J. A. Heginbottom, and E. S. Melnikov, 1997: Circum-Arctic map of permafrost and ground-ice conditions. U.S. Geological Survey Circum-Pacific Map CP-45, 1:10,000,000, https://doi.org/10.3133/cp45.

Brown, R., B. Brasnett, and D. Robinson, 2003: Gridded North American monthly snow depth and snow water equivalent for GCM evaluation. *Atmos.–Ocean*, **41**, 1–14, https://doi.org/10.3137/ao.410101.

——, D. Vikhamar Schuler, O. Bulygina, C. Derksen, K. Luojus, L. Mudryk, L. Wang, and D. Yang, 2017: Arctic terrestrial snow cover. Snow, Water, Ice and Permafrost in the Arctic (SWIPA) 2017, Arctic Monitoring and Assessment Programme, 25–64, www.amap.no/documents/doc/snow-water-ice-and-permafrost-in-the-arctic-swipa-2017/1610.

Brun, E., V. Vionnet, A. Boone, B. Decharme, Y. Peings, R. Valette, F. Karbou, and S. Morin, 2013: Simulation of Northern Eurasian local snow depth, mass, and density using a detailed snowpack model and meteorological reanalyses. *J. Hydrometeor.*, **14**, 203–219, https://doi.org/10.1175/JHM-D-12-012.1.

Butchart, N., and E. E. Remsberg, 1986: The area of the stratospheric polar vortex as a diagnostic for tracer transport on an isentropic surface. *J. Atmos. Sci.*, **43**, 1319–1339, https://doi.org/10.1175/1520-0469(1986)043<1319:TAOTSP>2.0.CO;2.

Callaghan, T., and Coauthors, 2011: The changing face of Arctic snow cover: A synthesis of observed and projected changes. *AMBIO*, **40**, 17–3131, https://doi.org/10.1007/s13280-011-0212-y.

Cape, M. R., F. Straneo, N. Beaird, R. M. Bundy, and M. A. Charette, 2019: Nutrient release to oceans from buoyancy-driven upwelling at Greenland tidewater glaciers. *Nat. Geosci.*, **12**, 34–39, https://doi.org/10.1038/S41561-018-0268-4.

Cappelen, J., Ed., 2020: Greenland - DMI historical climate data collection 1784-2019. DMI Rep. 20-04, Danish Meteorological Institute, 119 pp., www.dmi.dk/fileadmin/Rapporter/2020/DMIRep20-04.pdf.

Cavalieri, D. J., C. L. Parkinson, P. Gloersen, and H. J. Zwally, 1996: Sea ice concentrations from Nimbus-7 SMMR and DMSP SSM/I-SSMIS passive microwave data, version 1 (updated yearly). NASA NSIDC DAAC, accessed 1 November 2019, https://doi.org/10.5067/8GQ8LZQVL0VL.

Christiansen, H. H., and Coauthors, 2010: The thermal state of permafrost in the Nordic area during the International Polar Year 2007–2009. *Permafrost Periglacial Processes*, **21**, 156–181, https://doi.org/10.1002/ppp.687.

Commane, R., and Coauthors, 2017: Carbon dioxide sources from Alaska driven by increasing early winter respiration from Arctic tundra. *Proc. Natl. Acad. Sci. USA*, **114**, 5361–5366, https://doi.org/10.1073/pnas.1618567114.

Cray, H. A., and W. H. Pollard, 2018: Use of stabilized thaw slumps by Arctic birds and mammals: Evidence from Herschel Island, Yukon. *Can. Field Nat.*, **132**, 279–284, https://doi.org/10.22621/cfn.v132i3.1988.

Dee, D. P., and Coauthors, 2011: The ERA-Interim reanalysis: Configuration and performance of the data assimilation system. *Quart. J. Roy. Meteor. Soc.*, **137**, 553–597, https://doi.org/10.1002/qj.828.

Duchesne, C., S. L. Smith, M. Ednie, and P. P. Bonnaventure, 2015: Active layer variability and change in the Mackenzie Valley, Northwest Territories. 68th Canadian Geotechnical Conf./7th Canadian Conf. on Permafrost, Quebec, Canada, GEOQuébec, Paper 117.

Dufour, A., O. Zolina, and S. K. Gulev, 2016: Atmospheric moisture transport to the Arctic. *J. Climate*, **29**, 5061–5081, https://doi.org/10.1175/JCLI-D-15-0559.1.

Duncan, B. N., and Coauthors, 2019: Space-based observations for understanding changes in the Arctic-Boreal zone. *Rev. Geophys.*, **58**, e2019RG000652, https://doi.org/10.1029/2019RG000652.

Ednie, M., and S. L. Smith, 2015: Permafrost temperature data 2008-2014 from community based monitoring sites in Nunavut. Geological Survey of Canada Open File 7784, 18 pp., https://doi.org/10.4095/296705.

EEAP, 2019: Environmental effects and interactions of stratospheric ozone depletion, UV radiation, and climate change. 2018 Assessment Rep. Nairobi: Environmental Effects Assessment Panel, United Nations Environment Programme (UNEP), 390 pp., https://ozone.unep.org/sites/default/files/2019-04/EEAP_assessment-report-2018%20%282%29.pdf.

Estilow, T. W., A. H. Young, and D. A. Robinson, 2015: A long-term Northern Hemisphere snow cover extent data record for climate studies and monitoring. *Earth Syst. Sci. Data*, **7**, 137–142, https://doi.org/10.5194/essd-7-137-2015.

Farquharson, L. M., V. E. Romanovsky, W. L. Cable, D. A. Walker, S. V. Kokelj, and D. Nicolsky, 2019: Climate change drives widespread and rapid thermokarst development in very cold permafrost in the Canadian High Arctic. *Geophys. Res. Lett.*, **46**, 6681–6689, https://doi.org/10.1029/2019GL082187.

Fausto, R. S. and D. van As, 2019: Programme for monitoring of the Greenland ice sheet (PROMICE): Automatic weather station data, v03. Geological Survey of Denmark and Greenland, accessed 10 January 2020, https://doi.org/10.22008/promice/data/aws.

Fetterer, F., K. Knowles, W. N. Meier, M. Savoie, and A. K. Windnagel, 2017: Sea ice index, version 3: Regional daily data (updated daily). NSIDC, accessed 1 February 2020, https://doi.org/10.7265/N5K072F8.

Fettweis, X., 2007: Reconstruction of the 1979–2006 Greenland ice sheet surface mass balance using the regional climate model MAR. *Cryosphere*, **1**, 21–40, https://doi.org/10.5194/tc-1-21-2007.

Fissel, B., and Coauthors, 2019: Stock assessment and fishery evaluation report for the groundfish fisheries of the Gulf of Alaska and Bering Sea/Aleutian Island Area. Economic Status of the Groundfish Fisheries off Alaska, NOAA, 297 pp., www.fisheries.noaa.gov/resource/data/2018-economic-status-groundfish-fisheries-alaska.

Fossheim, M., R. Primicerio, E. Johannesen, R. B. Ingvaldsen, M. M. Aschan, and A. V. Dolgov, 2015: Recent warming leads to a rapid borealization of fish communities in the Arctic. *Nat. Climate Change*, **5**, 673–677, https://doi.org/10.1038/nclimate2647.

Gardner, A. S., and Coauthors, 2011: Sharply increased mass loss from glaciers and ice caps in the Canadian Arctic Archipelago. *Nature*, **473**, 357–360, https://doi.org/10.1038/nature10089.

——, and Coauthors, 2013: A reconciled estimate of glacier contributions to sea level rise: 2003–2009. *Science*, **340**, 852–857, https://doi.org/10.1126/science.1234532.

Helfrich, S., D. McNamara, B. Ramsay, T. Baldwin, and T. Kasheta, 2007: Enhancements to, and forthcoming developments in the Interactive Multisensor Snow and Ice Mapping System (IMS). *Hydrol. Processes*, **21**, 1576–1586, https://doi.org/10.1002/hyp.6720.

Herman-Mercer, N. M., M. Laituri, M. Massey, E. Matkin, R. Toohey, K. Elder, P. F. Schuster, and E. Mutter, 2019: Vulnerability of subsistence systems due to social and environmental change: A case study in the Yukon-Kuskokwim Delta, Alaska. *Arctic*, **72**, 258–272, https://doi.org/10.14430/arctic68867.

Hewitt, R. E., D. L. Taylor, H. Genet, A. D. McGuire, and M. C. Mack, 2019: Below-ground plant traits influence tundra plant acquisition of newly thawed permafrost nitrogen. *J. Ecol.*, **107**, 950–962, https://doi.org/10.1111/1365-2745.13062.

Hollowed, A. B., and Coauthors, 2013: Projected impacts of climate change on marine fish and fisheries. *ICES J. Mar. Sci.*, **70**, 1023–1037, https://doi.org/10.1093/icesjms/fst081.

Hopwood, M. J., D. Carroll, T. J. Browning, L. Meire, J. Mortensen, S. Krisch, and E. P. Achterberg, 2018: Non-linear response of summertime marine productivity to increased meltwater discharge around Greenland. *Nat. Commun.*, **9**, 3256, https://doi.org/10.1038/S41467-018-05488-8.

Hugelius, G., and Coauthors, 2014: Improved estimates show large circumpolar stocks of permafrost carbon while quantifying substantial uncertainty ranges and identifying remaining data gaps. *Biogeosciences*, **11**, 6573–6593, https://doi.org/10.5194/bg-11-6573-2014.

Ims, R. A., J.-A. Henden, M. A. Strømeng, A. V. Thingnes, M. J. Garmo, and J. U. Jepsen, 2019: Arctic greening and bird nest predation risk across tundra ecotones. *Nat. Climate Change*, **9**, 607–610, https://doi.org/10.1038/s41558-019-0514-9.

Jacob, T., J. Wahr, W. T. Pfeffer, and S. Swenson, 2012: Recent contributions of glaciers and ice caps to sea level rise. *Nature*, **482**, 514–518, https://doi.org/10.1038/nature10847.

Jobbágy, E. G., and R. B. Jackson, 2000: The vertical distribution of soil organic carbon and its relation to climate and vegetation. *Ecol. Appl.*, **10**, 423–436, https://doi.org/10.1890/1051-0761(2000)010[0423:TVDOSO]2.0.CO;2.

Kalnay, E., and Coauthors, 1996: The NCEP/NCAR 40-Year Reanalysis Project. *Bull. Amer. Meteor. Soc.*, **77**, 437–471, https://doi.org/https://doi.org/10.1175/1520-0477(1996)077<0437:TNYRP>2.0.CO;2.

Kim, B.-M., and Coauthors, 2017: Major cause of unprecedented Arctic warming in January 2016: Critical role of an Atlantic windstorm. *Sci. Rep.*, **7**, 40051, https://doi.org/10.1038/srep40051.

Kjøllmoen, B., L. M. Andreassen, H. Elvehøy, and M. Jackson, 2019: Glaciological investigations in Norway 2018. NVE Rep. 46.2019, 84 pp., http://publikasjoner.nve.no/rapport/2019/rapport2019_46.pdf.

Le Quéré, C., and Coauthors, 2018: Global Carbon Budget 2018. *Earth Syst. Sci. Data*, **10** (4), 2141–2194, https://doi.org/10.5194/essd-10-2141-2018.

Langenbrunner, B., 2020: Ocean-driven Arctic warming. *Nat. Climate Change*, **10**, 184, https://doi.org/10.1038/s41558-020-0730-3.

Lee, S. H., and A. H. Butler, 2020: The 2018–2019 Arctic stratospheric polar vortex. *Weather*, **75**, 52–57, https://doi.org/10.1002/wea.3643.

Luo, H., R. M. Castelao, A. K. Rennermalm, M. Tedesco, A. Bracco, P. L. Yager, and T. L. Mote, 2016: Oceanic transport of surface meltwater from the southern Greenland ice sheet. *Nat. Geosci.*, **9**, 528–532, https://doi.org/10.1038/ngeo2708.

Mahlstein, I., and R. Knutti, 2012: September Arctic sea ice predicted to disappear near 2°C global warming above present. *J. Geophys. Res.*, **117**, D06104, https://doi.org/10.1029/2011JD016709.

Manney, G. L., and Coauthors, 2011: Unprecedented Arctic ozone loss in 2011. *Nature*, **478**, 469–475, https://doi.org/10.1038/nature10556.

Manney, G. L., Z. D. Lawrence, M. L. Santee, N. J. Livesey, A. Lambert, and M. C. Pitts, 2015: Polar processing in a split vortex: Arctic ozone loss in early winter 2012/2013. *Atmos. Chem. Phys.*, **15**, 5381–5403, https://doi.org/10.5194/acp-15-5381-2015.

Marsh, J. M., and F. J. Mueter, 2020: Influences of temperature, predators, and competitors on polar cod (Boreogadus saida) at the southern margin of their distribution. *Polar Biol.*, https://doi.org/10.1007/s00300-019-02575-4, in press.

Maslanik, J., and J. Stroeve, 1999: Near-real-time DMSP SSMIS daily polar gridded sea ice concentrations, version 1. NASA NSIDC DAAC, accessed 1 February 2020, https://doi.org/10.5067/U8C09DWVX9LM.

——, ——, C. Fowler, and W. Emery, 2011: Distribution and trends in Arctic sea ice age through spring 2011. *Geophys. Res. Lett.*, **38**, L13502, https://doi.org/10.1029/2011GL047735.

Meier, W. N., and J. S. Stewart, 2019: Assessing uncertainties in sea ice extent climate indicators. *Environ. Res. Lett.*, **14**, 035005, https://doi.org/10.1088/1748-9326/aaf52c.

——, ——, and F. Fetterer, 2007: Whither Arctic sea ice? A clear signal of decline regionally, seasonally and extending beyond the satellite record. *Ann. Glaciol.*, **46**, 428–434, https://doi.org/10.3189/172756407782871170.

——, and Coauthors, 2014: Arctic sea ice in transformation: A review of recent observed changes and impacts on biology and human activity. *Rev. Geophys.*, **52**, 185–217, https://doi.org/10.1002/2013RG000431.

——, F. Fetterer, M. Savoie, S. Mallory, R. Duerr, and J. Stroeve, 2017: NOAA/NSIDC climate data record of passive microwave sea ice concentration, version 3. NSIDC, accessed 1 November 2019, https://doi.org/10.7265/N59P2ZTG.

Millan, R., J. Mouginot, and E. Rignot, 2017: Mass budget of the glaciers and ice caps of the Queen Elizabeth Islands, Canada, from 1991 to 2015. *Environ. Res. Lett.*, **12**, 024016, https://doi.org/10.1088/1748-9326/aa5b04.

Morlighem, M., and Coauthors, 2017: BedMachine v3: Complete bed topography and ocean bathymetry mapping of Greenland from multibeam echo sounding combined with mass conservation. *Geophys. Res. Lett.*, **44**, 11 051–11 061, https://doi.org/10.1002/2017GL074954.

Mörsdorf, M. A., N. S. Baggesen, N. G. Yoccoz, A. Michelsen, B. Elberling, P. L. Ambus, and E. J. Cooper, 2019: Deepened winter snow significantly influences the availability and forms of nitrogen taken up by plants in High Arctic tundra. *Soil Biol. Biochem.*, **135**, 222–234, https://doi.org/10.1016/j.soilbio.2019.05.009.

Mote, T., 2007: Greenland surface melt trends 1973–2007: Evidence of a large increase in 2007. *Geophys. Res. Lett.*, **34**, L22507, https://doi.org/10.1029/2007GL031976.

Mouginot, J., and Coauthors, 2019: Forty-six years of Greenland Ice Sheet mass balance from 1972 to 2018. *Proc. Natl. Acad. Sci. USA*, **116**, 9239–9244, https://doi.org/10.1073/pnas.1904242116.

Mudryk, L., M. Santolaria-Otín, G. Krinner, M. Ménégoz, C. Derksen, C. Brutel-Vuilmet, M. Brady, and R. Essery, 2020: Historical Northern Hemisphere snow cover trends and projected changes in the CMIP-6 multi-model ensemble. *Cryosphere Discuss.*, https://doi.org/10.5194/tc-2019-320.

Müller, R., J.-U. Grooß, C. Lemmen, D. Heinze, M. Dameris, and G. Bodeker, 2008: Simple measures of ozone depletion in the polar stratosphere. *Atmos. Chem. Phys.*, **8**, 251–264, https://doi.org/10.5194/acp-8-251-2008.

Myers-Smith, I. H., and Coauthors, 2020: Complexity revealed in the greening of the Arctic. *Nat. Climate Change*, **10**, 106–117, https://doi.org/10.1038/s41558-019-0688-1.

Natali, S., and Coauthors, 2019: Large loss of CO2 in winter observed across the northern permafrost region. *Nat. Climate Change*, 9, 852–857, https://doi.org/10.1038/s41558-019-0592-8.

National Academies of Sciences, Engineering, and Medicine, 2019: Understanding Northern Latitude Vegetation Greening and Browning: Proceedings of a Workshop. National Academies Press, 62 pp., https://doi.org/10.17226/25423.

Notz, D., and J. Stroeve, 2016: Observed Arctic sea-ice loss directly follows anthropogenic CO2 emission. *Science*, **354**, 747–750, https://doi.org/10.1126/science.aag2345.

NPFMC, 2018: Fishery management plan for groundfish of the Bering Sea and Aleutian Islands Management Area. North Pacific Fishery Management Council, 152 pp., www.npfmc.org/wp-content/PDFdocuments/fmp/BSAI/BSAIfmp.pdf.

O'Neel, S., and Coauthors, 2019: Reanalysis of the US Geological Survey Benchmark Glaciers: Long-term insight into climate forcing of glacier mass balance. *J. Glaciol.*, **65**, 850–866, https://doi.org/10.1017/jog.2019.66.

Overeem, I., B. D. Hudson, J. P. M. Syvitski, A. B. Mikkelsen, B. Hasholt, M. R. Van Den Broeke, B. P. Y. Noël, and M. Morlighem, 2017: Substantial export of suspended sediment to the global oceans from glacial erosion in Greenland. *Nat. Geosci.*, **10**, 859–863, https://doi.org/10.1038/ngeo3046.

Overland, J. E., 2009: The case for global warming in the Arctic. Influence of Climate Change on the Changing Arctic and Sub-Arctic Conditions, J. C. J. Nihoul and A. G. Kostianoy, Eds., Springer, 13–23.

——, E. Hanna, I. Hanssen-Bauer, S.-J. Kim, J. E. Walsh, M. Wang, and U. S. Bhatt, 2019: Surface air temperature [in "State of the Climate in 2018"]. *Bull. Amer. Meteor. Soc.*, **100** (9), S142–S143., https://doi.org/10.1175/2019BAMSStateoftheClimate.1.

Peng, G., W. N. Meier, D. J. Scott, and M. H. Savoie, 2013: A long-term and reproducible passive microwave sea ice concentration data record for climate studies and monitoring. *Earth Syst. Sci. Data*, **5**, 311–318, https://doi.org/10.5194/essd-5-311-2013.

Piao, S., and Coauthors, 2019: Characteristics, drivers and feedbacks of global greening. *Nat. Rev. Earth Environ.*, **1**, 14–27, https://doi.org/10.1038/s43017-019-0001-x.

Pinsky, M. L., B. Worm, M. J. Fogarty, J. L. Sarmiento, and S. A. Levin, 2013: Marine taxa track local climate velocities. *Science*, **341**, 1239–1242, https://doi.org/10.1126/science.1239352.

Pinzon, J., and C. Tucker, 2014: A non-stationary 1981–2012 AVHRR NDVI3g time series. *Remote Sens.*, **6**, 6929–6960, https://doi.org/10.3390/rs6086929.

Pithan, F., and T. Mauritsen, 2014: Arctic amplification dominated by temperature feedbacks in contemporary climate models. *Nat. Geosci.*, **7**, 181–184, https://doi.org/10.1038/ngeo2071.

Post, E., and Coauthors, 2019: The polar regions in a 2°C warmer world. *Sci. Adv.*, **5**, eaaw9883, https://doi.org/10.1126/sciadv.aaw9883.

Raynolds, M. K., D. A. Walker, H. E. Epstein, J. E. Pinzon, and C. J. Tucker, 2012: A new estimate of tundra-biome phytomass from trans-Arctic field data and AVHRR NDVI. *Remote Sens. Lett.*, **3**, 403–411, https://doi.org/10.1080/01431161.2011.609188.

Reichle, R., C. Draper, Q. Liu, M. Girotto, S. Mahanama, R. Koster, and G. De Lannoy, 2017: Assessment of MERRA-2 land surface hydrology estimates. *J. Climate*, **30**, 2937–2960, https://doi.org/10.1175/JCLI-D-16-0720.1.

Reynolds, R. W., N. A. Rayner, T. M. Smith, D. C. Stokes, and W. Wang, 2002: An improved in situ and satellite SST analysis for climate. *J. Climate*, **15**, 1609–1625, https://doi.org/10.1175/1520-0442(2002)015<1609:AIISAS>2.0.CO;2.

——, T. M. Smith, C. Liu, D. B. Chelton, K. S. Casey, and M. G. Schlax, 2007: Daily high-resolution-blended analyses for sea surface temperature. *J. Climate*, **20**, 5473–5496, https://doi.org/10.1175/2007JCLI1824.1.

Richter-Menge, J., M. L. Druckenmiller, and M. Jeffries, Eds., 2019: Arctic Report Card 2019. NOAA, www.arctic.noaa.gov/Report-Card.

Romanovsky, V. E., and Coauthors, 2017: Changing permafrost and its impacts. Snow, Water, Ice and Permafrost in the Arctic (SWIPA) 2017, Arctic, Monitoring and Assessment Programme, 65–102, www.amap.no/documents/doc/snow-water-ice-and-permafrost-in-the-arctic-swipa-2017/1610.

Salmon, V. G., A. L. Breen, J. Kumar, M. J. Lara, P. E. Thornton, S. D. Wullschleger, and C. M. Iversen, 2019: Alder distribution and expansion across a tundra hillslope: Implications for local N cycling. *Front. Plant Sci.*, **10**, 1099, https://doi.org/10.3389/fpls.2019.01099.

Schmidt, N. M., J. Reneerkens, J. H. Christensen, M. Olesen, and T. Roslin, 2019: An ecosystem-wide reproductive failure with more snow in the Arctic. *PLoS Biol.*, **17**, e3000392, https://doi.org/10.1371/journal.pbio.3000392.

Schuur, E. A. G., 2019: Permafrost and the global carbon cycle. Arctic Report Card 2019, J. Richter-Menge, M. L. Druckenmiller, and M. Jeffries, Eds., NOAA, www.arctic.noaa.gov/Report-Card.

——, and Coauthors, 2008: Vulnerability of permafrost carbon to climate change: Implications for the global carbon cycle. *BioScience*, **58**, 701–714, https://doi.org/10.1641/B580807.

——, and Coauthors, 2015: Climate change and the permafrost carbon feedback. *Nature*, **520**, 171–179, https://doi.org/10.1038/nature14338.

——, and Coauthors, 2018: Chapter 11: Arctic and boreal carbon. Second State of the Carbon Cycle Report (SOCCR2): A Sustained Assessment Report, N. Cavallaro et al., Eds., U.S. Global Change Research Program, 428–468.

Sharp, M., and Coauthors, 2018: Glaciers and ice caps outside Greenland [in "State of the Climate in 2017"]. *Bull. Amer. Meteor. Soc.*, **99** (8), S156–S161, https://doi.org/10.1175/2018BAMSStateoftheClimate.1.

Shiklomanov, N. I., D. A. Streletskiy, and F. E. Nelson, 2012: Northern Hemisphere component of the global Circumpolar Active Layer Monitoring (CALM) program. Proc. 10th Int. Conf. on Permafrost, Vol. 1, Salekhard, Russia, Tyumen Oil and Gas University, 377–382.

Smith, S. L., J. Chartrand, and C. Duchesne, 2018: Report on 2017 field activities and collection of ground-thermal and active-layer data in the Mackenzie corridor, Northwest Territories. Geological Survey of Canada Open File 8492, 109 pp., https://doi.org/10.4095/313036.

——, C. Duchesne, and A. G. Lewkowicz, 2019: Tracking changes in permafrost thermal state in Northern Canada. Cold Regions Engineering 2019, J.-P. Bilodeau et al. Eds., American Society of Civil Engineers, 670–677, https://doi.org/10.1061/9780784482599.

Stabeno, P. J., and S. W. Bell, 2019: Extreme conditions in the Bering Sea (2017–2018): Record breaking low sea-ice extent. *Geophys. Res. Lett.*, **46**, 8952–8959, https://doi.org/10.1029/2019GL083816.

——, and Coauthors, 2012: A comparison of the physics of the northern and southern shelves of the eastern Bering Sea and some implications for the ecosystem. *Deep-Sea Res. II*, **65**, 14–30, https://doi.org/10.1016/j.dsr2.2012.02.019.

——, R. L. Thoman, and K. Wood, 2019: Recent warming in the Bering Sea and its impact on the ecosystem. Arctic Report Card 2019, J. Richter-Menge, M. L. Druckenmiller, and M. Jeffries, Eds., NOAA, www.arctic.noaa.gov/Report-Card.

Stevenson, D. E., and R. R. Lauth, 2019: Bottom trawl surveys in the northern Bering Sea indicate recent shifts in the distribution of marine species. *Polar Biol.*, **42**, 407–421, https://doi.org/10.1007/s00300-018-2431-1.

Strauss, J., L. Schirrmeister, G. Grosse, S. Wetterich, M. Ulrich, U. Herzschuh, and H.-W. Hubberten, 2013: The deep permafrost carbon pool of the Yedoma region in Siberia and Alaska. *Geophys. Res. Lett.*, **40**, 6165–6170, https://doi.org/10.1002/2013GL058088.

——, and Coauthors, 2017: Deep Yedoma permafrost: A synthesis of depositional characteristics and carbon vulnerability. *Earth-Sci. Rev.*, **172**, 75–86, https://doi.org/10.1016/j.earscirev.2017.07.007.

Stroh, J. N., G. Panteleev, S. Kirillov, M. Makhotin, and N. Shakhova, 2015: Sea-surface temperature and salinity product comparison against external in situ data in the Arctic Ocean. *J. Geophys. Res. Oceans*, **120**, 7223–7236, https://doi.org/10.1002/2015JC011005.

Stuecker, M. F., and Coauthors, 2018: Polar amplification dominated by local forcing and feedbacks. *Nat. Climate Change*, **8**, 1076–1081, https://doi.org/10.1038/s41558-018-0339-y.

Takala, M., K. Luojus, J. Pulliainen, C. Derksen, J. Lemmetyinen, J.-P. Kärnä, and J. Koskinen, 2011: Estimating northern hemisphere snow water equivalent for climate research through assimilation of space-borne radiometer data and ground-based measurements. *Remote Sens. Environ.*, **115**, 3517–3529, https://doi.org/10.1016/j.rse.2011.08.014.

Tanskanen, A., 2004: Lambertian surface albedo climatology at 360 nm from TOMS data using moving time-window technique. Proceedings of the XX Quadrennial Ozone Symposium, C. S. Zerefos, Ed., Vol. II, International Ozone Commission, 1159–1160.

Tape, K. D., B. M. Jones, C. D. Arp, I. Nitze, and G. Grosse, 2018: Tundra be dammed: Beaver colonization of the Arctic. *Global Change Biol.*, **24**, 4478–4488, https://doi.org/10.1111/gcb.14332.

Taylor, A. R., R. B. Lanctot, and R. T. Holmes, 2018: An evaluation of 60 years of shorebird response to environmental change at Utqiaġvik (Barrow). Alaska. Trends and Traditions: Avifaunal Change in Western North America, W. D. Shuford, R. E. Gill, and C. M. Handel, Eds., Western Field Ornithologists, 312–330.

Tedesco, M., and X. Fettweis, 2020: Unprecedented atmospheric conditions (1948–2019) drive the 2019 exceptional melting season over the Greenland ice sheet. *Cryosphere*, 14, 1209–1223, https://doi.org/10.5194/tc-14-1209-2020.

——, ——, T. Mote, J. Wahr, P. Alexander, J. Box, and B. Wouters, 2013: Evidence and analysis of 2012 Greenland records from spaceborne observations, a regional climate model and reanalysis data. *Cryosphere*, **7**, 615–630, https://doi.org/10.5194/tc-7-615-2013.

Thoman, R. L., and Coauthors, 2020: The record low Bering Sea ice extent in 2018: Context, impacts, and an assessment of the role of anthropogenic climate change [in "Explaining Extreme Events of 2018 from a Climate Perspective"]. *Bull. Amer. Meteor. Soc.*, **101** (1), S53–S58, https://doi.org/10.1175/BAMS-D-19-0175.1.

Thorson, J. T., 2019: Guidance for decisions using the Vector Autoregressive Spatio-Temporal (VAST) package in stock, ecosystem, habitat and climate assessments. *Fish. Res.*, **210**, 143–161, https://doi.org/10.1016/j.fishres.2018.10.013.

——, and Coauthors, 2019: Comparison of near-bottom fish densities show rapid community and population shifts in Bering and Barents Seas. Arctic Report Card 2019, J. Richter-Menge, M. L. Druckenmiller, and M. Jeffries, Eds., NOAA, www.arctic.noaa.gov/Report-Card.

Timmermans, M.-L., and A. Proshutinsky, 2015: The Arctic: Sea surface temperature [in "State of the Climate in 2014"]. *Bull. Amer. Meteor. Soc.*, **96** (7), S147–S148, https://doi.org/10.1175/2015BAMSStateoftheClimate.1.

Treharne, R., J. W. Bjerke, H. Tømmervik, L. Stendardi, and G. K. Phoenix, 2019: Arctic browning: Impacts of extreme climatic events on heathland ecosystem CO2 fluxes. *Global Change Biol.*, **25**, 489–503, https://doi.org/10.1111/gcb.14500.

Tschudi, M. A., J. C. Stroeve, and J. S. Stewart, 2016: Relating the age of Arctic sea ice to its thickness, as measured during NASA's ICESat and IceBridge Campaigns. *Remote Sens.*, **8**, 457, https://doi.org/10.3390/rs8060457.

——, W. N. Meier, J. S. Stewart, C. Fowler, and J. Maslanik, 2019a: EASE-Grid sea ice age, version 4. NASA NSIDC DAAC, accessed 1 November 2019, https://doi.org/10.5067/UTAV7490FEPB.

——, ——, and ——, 2019b: Quicklook Arctic weekly EASE-Grid sea ice age, version 1. NASA NSIDC DAAC, accessed 1 November 2019, https://doi.org/10.5067/2XXGZY3DUGNQ.

U.S. National Ice Center, 2008: IMS daily Northern Hemisphere snow and ice analysis at 1 km, 4 km, and 24 km resolutions, version 1 [24km] (updated daily). NSIDC, accessed 1 November 2019, https://doi.org/10.7265/N52R3PMC.

van As, D., R. S. Fausto, J. Cappelen, R. S. W. van de Wal, R. J. Braithwaite, and H. Machguth, 2016: Placing Greenland ice sheet ablation measurements in a multi-decadal context. *Geol. Surv. Den. Greenl. Bull.*, **35**, 71–74, https://doi.org/10.34194/geusb.v35.4942.

van Pelt, W., and Coauthors, 2019: A long-term dataset of climatic mass balance, snow conditions, and runoff in Svalbard (1957–2018). *Cryosphere*, **13**, 2259–2280, https://doi.org/10.5194/tc-13-2259-2019.

Veldhuis, D., P. Tejsner, F. Riede, T. T. Høye, and R. Willerslev, 2018: Arctic disequilibrium: Shifting human-environmental systems. *Cross-Cultural Res.*, **53**, 243–251, https://doi.org/10.1177/1069397118815132.

Wahr, J., M. Molenaar, and F. Bryan, 1998: Time variability of the Earth's gravity field: Hydrological and oceanic effects and their possible detection using GRACE. *J. Geophys. Res.*, **103**, 30205–30229, https://doi.org/10.1029/98JB02844.

Walsh, J. E., W. L. Chapman, F. Fetterer, and J. S. Stewart, 2019: Gridded monthly sea ice extent and concentration, 1850 onward, version 2. NSIDC, accessed 1 November 2019, https://doi.org/10.7265/jj4s-tq79.

Walker, D. A., and Coauthors, 2005: The circumpolar Arctic vegetation map. *J. Veg. Sci.*, **16**, 267–282, https://doi.org/10.1111/j.1654-1103.2005.tb02365.x.

Weatherhead, B., A. Tanskanen, and A. Stevermer, 2005: Ozone and ultraviolet radiation. Arctic Climate Impact Assessment, Cambridge University Press, 152–182. www.amap.no/documents/download/1086/inline.

WGMS, 2017: Global Glacier Change Bulletin. M. Zemp et al., Eds., Bulletin 2 (2014–2015),ICSU(WDS)/IUGG(IACS)/UNEP/UNESCO/WMO, 244 pp., https://doi.org/10.5904/wgms-fog-2017-1.

WHO, 2002: Global solar UV index: A practical guide. WHO/SDE/OEH/02.2, WHO/WMO,UNEP/ICNIRP, 28 pp., www.who.int/uv/publications/en/GlobalUVI.pdf.

Wilcox, E. J., D. Keim, T. de Jong, B. Walker, O. Sonnentag, A. E. Sniderhan, P. Mann, and P. Marsh, 2019: Tundra shrub expansion may amplify permafrost thaw by advancing snowmelt timing. *Arct. Sci.*, **5**, 202–217, https://doi.org/10.1139/as-2018-0028.

WMO, 2018: Scientific assessment of ozone depletion: 2018. Global Ozone Research and Monitoring Project Rep. 58, World Meteorological Organization, 588 pp., www.esrl.noaa.gov/csl/assessments/ozone/2018/downloads/2018OzoneAssessment.pdf.

Wouters, B., A. S. Gardner, and G. Moholdt, 2019: Global glacier mass loss during the GRACE satellite mission (2002–2016). *Front. Earth Sci.*, **7**, 96, https://doi.org/10.3389/feart.2019.00096.

Wyllie-Echeverria, T., and W. S. Wooster, 1998: Year-to-year variations in Bering Sea ice cover and some consequences for fish distributions. *Fish. Oceanogr.*, **7**, 159–170, https://doi.org/10.1046/j.1365-2419.1998.00058.x.

Zemp, M., and Coauthors, 2019: Global glacier mass changes and their contributions to sea-level rise from 1961 to 2016. *Nature*, **568**, 382–386, https://doi.org/10.1038/s41586-019-1071-0.